



DOCTORAL THESIS

Simulation of the packaging process of embedded components in printed circuit boards

Katerina MACUROVA

*A thesis submitted in fulfilment of the requirements
for the degree of Dr.mont.
in the*

**Montanuniversitaet Leoben
Institute of Mechanics**



Leoben, April 2015

Affidavit

I declare in lieu of oath that I wrote this thesis and performed the associated research myself, using only literature cited in this volume.

Signed:

Date:

"Design is not what it looks and feels like. Design is how it works"

Steve Jobs

Dedicated to my family. . .

Abstract

The aim of the thesis is to investigate the critical steps during the embedding process, which is used in the manufacturing of highly integrated printed circuit boards (PCBs). The embedding technology enables reduction of space (and cost) and an increase of board performance by introducing functional components (*e.g.* silicon dies) inside the PCB. The critical process steps during die embedding are (i) the die attachment, (ii) the die assembly, and (iii) the lamination process. A second objective is to evaluate the package reliability during temperature cycling and provide design rules to increase the lifetime of PCB systems.

Concerning the die attachment the focus is set on the description of the adhesive bond line thickness development underneath a silicon die as a function of the attachment force and holding time. The solution is obtained with an analytical squeeze flow approach as well as a numerical simulation using computational fluid dynamics.

The die assembly and the lamination process are analyzed in terms of stresses and package warpage, which occur due to the mismatch of coefficients of thermal expansions during adhesive and epoxy resin curing at elevated temperatures. Special attention is given to the derivation of a volumetric shrinkage of the polymers during their phase transformation, which results in a major loading mechanism of the structure.

The stress-strain state of the assembled structure is investigated both analytically using (i) classical laminate theory and (ii) the interfacial model, and numerically by a finite element analysis, respectively.

The complex laminated package containing prepregs (a glass woven structure pre-impregnated with the epoxy resin) is numerically analyzed using finite element analysis (FEA). A special focus is set on orthotropic properties of the prepregs, which are analytically homogenized based on the lamination theory of plain woven composites.

The warpage results of the assembled and the laminated packages are validated experimentally by an X-ray diffraction method (Rocking-Curve-Technique) showing a good agreement between the calculated and measured curvature radius values.

Finally, reliability of a functional PCB board containing copper vias and traces is numerically analyzed under thermal cycling loading. Based on these results, a model is

proposed to identify critical vias within the package. The lifetime of the package associated with the failure of the critical via is estimated using analytical approaches for low-cycle fatigue.

As a result of this investigation, a numerical and analytical toolset for simulation of the stress-strain situation during the packaging production process steps has been developed. The influence of material and geometrical parameters on the package reliability has been studied. Finally, design rules for the overall embedding process have been derived, which consequently provide the possibility to improve the reliability of future PCB systems.

Acknowledgements

I would like to deeply acknowledge Raul Bermejo and Martin Pletz from the Institute of Structural and Functional Ceramics, Montanuniversitaet Leoben, for their advice and fruitful discussions about the results.

I am grateful to Abdellah Kharicha from the Chair of Simulation and Modelling of Metallurgical Processes, Montanuniversitaet Leoben, for his help and invaluable advice with the fluid dynamics simulations.

Thanks to Ronald Schöngrundner from Materials Center Leoben Forschung GmbH who managed the project that framed my thesis.

My supervisor Thomas Antretter is gratefully acknowledged for his positive attitude and advice during the embedding process investigation.

Special thanks go to all technicians, who provided material tests and experimental measurements.

I would like to thank T. Krivec and M. Morianz from AT&S, Austria, for providing the samples. The helpful discussions and support of M. Brizoux, W. Maia and A. Lecalevier from THALES, France, are gratefully acknowledged.

Financial support by the Austrian Federal Government (in particular from Bundesministerium für Verkehr, Innovation und Technologie and Bundesministerium für Wissenschaft, Forschung und Wirtschaft) represented by Österreichische Forschungsförderungsgesellschaft mbH and the Styrian and the Tyrolean Provincial Government, represented by Steirische Wirtschaftsförderungsgesellschaft mbH and Standortagentur Tirol, within the framework of the COMET Funding Programme is gratefully acknowledged.

Table of contents

Affidavit.....	i
Abstract.....	iv
Acknowledgements.....	vi
Table of contents.....	vii
List of symbols.....	ix
1. Introduction.....	1
1.1. Motivation and objectives.....	2
2. The die attachment process.....	3
2.1. Analytical description of the adhesive flow.....	5
2.2. Numerical description of the adhesive flow	9
2.2.1. Volume of Fluid.....	11
2.2.1.1. Adhesive droplet shape	13
2.2.1.2. Surface tension.....	14
2.2.1.3. Contact angle	14
2.2.2. Dynamic mesh	15
2.2.3. The 6DOF technique.....	16
2.3. Adhesive rheological properties	17
2.4. Results and discussion	19
2.4.1. Experimental validation	19
2.4.2. Numerical simulation results	22
2.4.3. Using the analytical model in numerical simulations	24
2.4.3.1. Adhesive droplet shape development.....	25
2.5. Summary and conclusions	27
3. The die assembly process	28
3.1. Analytical models	29
3.1.1. Classical laminate theory	29
3.1.2. Interfacial model	32
3.2. Numerical model	34
3.3. Material properties.....	36
3.4. Results and discussion	42
3.4.1. Deflection and validation.....	42

3.4.2.	Stress state in the assembly	45
3.4.3.	Interfacial stresses in the assembly	48
3.5.	Influence of nonlinear material behavior on a stress state in the assembly	52
3.6.	Summary and conclusions	54
4.	The lamination process.....	56
4.1.	Homogenization of the thermo-mechanical properties of plain woven composites	58
4.1.1.	Concept of lamination theory of woven structures	59
4.2.	Numerical model	65
4.3.	Material properties.....	69
4.4.	Results and discussion	73
4.5.	Summary and conclusions	78
5.	Reliability study of a PCB board with vias.....	79
5.1.	Fatigue life assessment of copper vias.....	81
5.2.	Numerical model	84
5.3.	Material properties.....	85
5.4.	Results and discussion	89
5.4.1.	Stress-strain investigation in the copper via patterns	91
5.4.1.1.	Application of the representative cell model.....	96
5.4.2.	Lifetime assessment of copper vias.....	99
5.5.	Summary and conclusions	100
6.	Parametric study and design rules for the embedding process.....	101
6.1.	Definition of failure criteria.....	102
6.2.	Parametric study	103
6.3.	Results and discussion	106
6.3.1.	Design rules for the assembly process	106
6.3.2.	Design rules for the lamination process	114
6.3.3.	Design rules for a PCB board with vias	118
6.4.	Summary and conclusions	126
7.	Conclusions.....	128
	List of figures.....	131
	List of tables.....	137
	References.....	139

List of symbols

Nomenclature

2D	Two dimensional
3D	Three dimensional
6DOF	Six degree of freedom
3PB	3-point bending
1ViaRef	Single via reference model
2ViasRef	Two vias reference model
B3B	Ball-on three-balls testing
FR-4	Prepreg, a glass-reinforced epoxy laminate
P1 - P4	Critical location for stress-strain evaluation in via radius transition
S1 - S4	Sections defining the most common via interconnects by traces
μ -DMA RSAG2	Type of micro-dynamic mechanical analyzer
A	
A	First temperature step of assembly process, heating-up to 80 °C
A_z	Stress evaluation location in assembled structure
B	
B	Second temperature step of assembly process, isothermal curing at 80 °C
BLT	Bond line thickness
B_z	Stress evaluation location in assembled structure
C	
C	Third temperature step of assembly process, heating-up to 130 °C
CCA	Composite cylinder assemblage
CFD	Computational fluid dynamics
CLT	Classical laminate theory
CTE	Coefficient of thermal expansion
Cu	Copper
C_z	Stress evaluation location in assembled structure
D	
D	Forth temperature step of assembly process, isothermal curing at 130 °C
DMA	Dynamic mechanical analysis
DOE	Design of experiments
E	
E	Fifth temperature step of assembly process
EBSD	Electron backscattering diffraction
F	
F	Step of the lamination process, heating-up to 200 °C
FEA	Finite element analysis
FEM	Finite element method
FVM	Finite volume method
G	
G	Step of the lamination process, cooling-down to RT

H	Copper removal process
LE	Linear elastic material model
MPC	Multi-point-constraint method
PCB	Printed circuit board
PL	Elasto-plastic material model
RC	Resin content
<i>Ref. FEA</i>	Numerical model of a laminate with a finite length $2L$ without the adhesive meniscus
RT	Room temperature
Si	Silicon
SF	Silicon footprint
TMA	Thermo-mechanical analysis
THK	Thickness
UD	Unidirectional
UDF	User defined function
VOF	Volume of fluid
X	Idealized via pattern containing all vias interconnected by traces
XRD	X-ray diffraction, Rocking-Curve-measurement

Latin symbols

\vec{A}	Face vector
A_{Cu}	area of a copper foil below and surrounding a single silicon die
A_{ij}	Extensional stiffness sub-matrix
$A_i^{(j)}$	Constants calculated from CTEs of the corresponding materials and geometry; $i, j = 1, 2$
A_{Si}	Area of a single silicon die
ABD	Matrix represents the elastic properties of the entire laminate
B_{ij}	Bending-extension coupling stiffness sub-matrix
B_L	Critical bow percentage
C	Courant number
D	The smallest drilled hole diameter of via
D_i	Flexural stiffness of the i -th layer
D_{ij}	Bending stiffness sub-matrix
E	Young's modulus
E_L	Longitudinal elastic modulus of UD lamina
E_T	Transversal elastic modulus of UD lamina
E_x	Elastic modulus in the x -direction
E_y	Elastic modulus in the y -direction
E_z	Elastic modulus in the z -direction
F	Attachment force

F_i	Shearing forces on the i-th layer
G_{LT}	Longitudinal-transversal shear modulus of UD lamina
G_{xy}	Shear modulus in the XY-plane
G_{xz}	Shear modulus in the XZ-plane
G_{yz}	Shear modulus in the YZ-plane
H	Via height
H_L	Total prepreg thickness
H/D	Via aspect ratio
L	Silicon die half-length defined by the interfacial model
L_{Cu}	Copper foil length half-distance between the modelled die and the adjacent one
L_d	Diagonal length of the silicon die
L_m	Side length of a triangular shaped adhesive meniscus
L_x	Silicon die half-length in x-direction
\underline{M}	Vector of bending moments
\underline{M}_{th}	Vector of equivalent virtual thermal bending moments
\underline{N}	Vector of normal force
N_i^T	Thermal stress resultants
N_f	Total number of cycles to failure
N_{fe}	Number of cycles to failure due to accumulated elastic strain
N_{fp}	Number of cycles to failure due to accumulated plastic strain
\underline{N}_{th}	Vector of equivalent virtual thermal forces
P	Maximum load at failure
Q_{ij}	Reduced stiffness matrix
$\overline{Q}_{ij,k}$	Transformed strand stiffness constants
R	Radius
R_d	Die radius
R_e	Radius defining area of P1 – P4 for stress-strain evaluation
$R_{p0.1}$	0.1 % offset yield strength
S_0	Outer span
$[\overline{S}_{ij}]_k$	Effective averaged compliance constants
$S_{ij}(\theta_k)$	Local reduced compliance constants
$T_{ref,as}$	Reference temperature of the assembly process
$T_{ref,lam}$	Reference temperature of the lamination process simulation
\vec{T}	Surface tension force vector
ΔT	Temperature change
ΔT_{ic}	Temperature increment of 1°C within isothermal curing simulation
V	Volume of element
V_0	Initial constant droplet volume
V^0	Total volume of the computational one-quarter prepreg structure

\dot{V}_f	Volume flux through an element face
V_f^0	Prepreg overall fiber volume fraction
V_f^s	Strand volume fraction inside the fill and the warp tows
V^{pm}	Volume fraction of the pure resin matrix
ΔV_{chem}	Chemical shrinkage
ΔV_{final}	Final curing volumetric shrinkage after package cool-down
ΔV_{therm}	Thermal shrinkage
ΔV_{tot}	Total volumetric shrinkage
∂V	Boundary of the element control volume V
∇	Nabla operator
a_f	Fill strand width
a_i	Arbitrary constant of the i -th layer
a_{yt}	Gap parameters of strands in the YZ-plane
a_w	Warp strand
b	Width of a specimen
b_i	Arbitrary constant of the i -th layer
c	Fatigue ductility exponent
d	Diagonal coordinate
d/L_d	Dimensionless ratio for evaluation of interfacial stress distribution to the silicon die corner
f	Numerically obtained dimensionless factor for definition of silicon strength
\vec{f}	Body forces vector
\vec{f}_{ext}	External forces vector
g_f	Gap between the fill strands
g_w	Gap between the warp strands
h	Adhesive height, bond line thickness
h_0	Initial adhesive droplet height
h_f	Height of the fill strand
h_i	Height of the i -th laminate layer
h_m	Height of a triangular shaped adhesive meniscus
h_v	Maximum vertical displacement of the silicon die
\bar{h}_f	Mean thickness of the fill strand
\bar{h}_m	Mean thickness of the resin matrix in the cross-ply laminate
\bar{h}_w	Mean thickness of the warp strand
k	Layer number
k	Consistency index
l	Specimen length
m	Mass

m_w	Weibull modulus
n	Power law index
n	Index of the preceding time step
$n+1$	Index of the current time step
\vec{n}	Normal to the phases interface
n_h	Hardening exponent
\vec{n}_w	Unit vectors normal to the wall
p	Pressure
P	Phase index of vacuum
q	Phase index of adhesive
r	Radial coordinate
t_s	Specimen thickness
\vec{t}	Tangent to the phases interface
\vec{t}_w	Unit vectors tangential to the wall
Δt	Time increment
\vec{v}	Velocity vector
\vec{v}_G	Velocity of the moving mesh
\vec{v}_g	Translation acceleration of the center of gravity
v_r	Radial velocity
\vec{v}_q	Velocity vector of phase q
x	x-axis (radial) coordinate
x/L	Dimensionless coordinate for evaluation of interfacial stress distribution along the silicon die edge
Δx_{elem}	Element mesh dimension
y	y-axis coordinate
z	z-axis (axial) coordinate
z_k	Distance from the midplane to the upper face of the k-th layer
$zx_1(x, y), zx_2(x, y)$	Strand shape parameters along the fill direction
zy_t	Gap parameters of strands in the YZ-plane
$zy_1(y), zy_2(y)$	Strand shape parameter along the warp direction

Greek symbols

Θ_k^{max}	Maximum undulation angle
$\Theta_w(y)$	Local off-axis undulation angle
Θ_w	Contact angle at the wall
α	Volume fraction
$\alpha_{C,r}$	Reactive curing coefficient of thermal expansion

$\alpha_i (\theta_k)$	The local reduced thermal expansion coefficients
$[\bar{\alpha}_i]_k$	Effective averaged thermal coefficients
α_L	Longitudinal coefficient of thermal expansion of UD lamina
α_T	Transversal coefficient of thermal expansion of UD lamina
α_w	Via wall angle between via bottom land and via
α_x	Coefficient of thermal expansion in the x-direction
α_y	Coefficient of thermal expansion in the y-direction
α_z	Coefficient of thermal expansion in the z-direction
β_w	Secondary wall angle, defined between via and via top land
$\dot{\gamma}$	Shear rate
$\underline{\varepsilon}^0$	Strain vector of the laminate midplane
$\varepsilon_0^p (T)$	Temperature dependent initial plastic strain
ε_f	Ductility
ε_{len}	Isotropic reactive length change
ε_p^{eq}	Accumulated equivalent plastic strain
ε_{true}	True strain
ε_{vol}	Reactive volumetric change
ε_y	Strain component in y-direction
$\Delta\varepsilon$	Strain range, strain increment
$\Delta\varepsilon_e$	Elastic strain range, elastic strain increment
$\Delta\varepsilon_p$	Plastic strain range, plastic strain increment, equivalent plastic strain increment
η	Viscosity
θ	Bragg angle
κ	Surface curvature
$\underline{\kappa}^0$	Vector of curvature of the laminate midplane
κ_i	Eigenvalue
ν	Poisson's ratio
ν_{TL}	Longitudinal-transversal Poisson's ration of UD lamina
ν_{xy}	Poisson's ratio in the XY-plane
ν_{xz}	Poisson's ratio in the XZ-plane
ν_{yz}	Poisson's ratio in the YZ-plane
π	Mathematical constant
ρ	Density
σ	Surface tension
σ_0	Characteristic strength
σ_1	Maximum principal stress
σ_f	Strength
σ_i	Peeling stress in the i-th interface
σ_{max}	Material the equivalent maximum stress corresponding to the fracture load P

σ_{true}	True stress
σ_x	In-plane stress in x-direction
σ_y	In-plane stress in y-direction
$\sigma_{y0}(T)$	Temperature dependent initial yield stress
σ_{yield}	Yield stress
σ_z	Stress component in z-direction, normal stress, peeling stress
τ_i	Shearing stresses on the laminate's i-th interface
$\overline{\overline{\tau}}$	Viscous stress tensor
$\overline{\overline{\tau}}_p$	Tangential stress at the interface of the vacuum p
$\overline{\overline{\tau}}_q$	Tangential stress at the interface of the adhesive q
ϕ	General scalar
ω	Coordinate of ω -axis
$\Delta\omega$	Step in ω -direction

1. Introduction

Early printed circuit boards (PCBs) were made of polymer panels onto which the electronic components (*e.g.* silicon dies) were assembled using surface-mounted technology [1]. Initially, the conductive traces were printed onto the surface, which limited the complexity of the design, since intersections of the traces were not possible. This led to the development of multi-layer printed circuit boards which distribute traces over multiple layers. Such a configuration reduces design limitations considerably, leading to more complex and powerful boards.

To continue the miniaturization of electronic devices, while at the same time increasing their functionality, Embedded Component Packaging (ECP[®]) technology was developed to integrate functional components in the inner layers of a multi-layer PCB [2, 3, 4]. ECP[®] has become state-of-the-art and industrially manufactured products are available. The next logical step for embedding modules is to increase the complexity by embedding of dies with hundreds of interconnections. Therefore the size of the dies requested to embed is constantly growing. For example the size has doubled in the last years. Additionally the ratio between a silicon area and a laminate area is increasing in a similar way, which results in an increasing warpage of the die and the board itself [2].

Since the functional die, which was before mounted on a PCB surface, is transferred into the inner layer of the laminate, the die is exposed to an additional loading as a consequence of the embedding process. As a result of a mismatch in the mechanical behaviors of the different kinds of materials involved [5], critical stresses within the dies or delamination of the dies can occur. Due to the brittleness of the silicon die the force required to fracture them can be of the order of a few Newton. In previous works the failure of typical $2 \times 2 \times 0.12 \text{ mm}^3$ silicon chips was analyzed and the mechanical resistance (strength) determined under biaxial bending [6, 7, 8]. The fracture loads for such geometry ranges from 5 N to 20 N for a loading configuration, *i.e.* biaxial bending that has some similarities with the loading during die embedding.

1.1. Motivation and objectives

With the trend towards increasing complexity of PCBs, there is a considerable interest of investigating the embedding process. The embedding process chain is illustrated in Figure 1.

The objective of the thesis is to understand the physics of the embedding process in order to determine the loading on the silicon die during manufacturing of PCBs. The minimum requirement for the die embedding is a survival of the functional component followed by high demands on the process improvement to increase the package reliability. Therefore a modelling tool box for the embedding process steps is developed. This includes integration of all relevant process steps for the embedding. The steps are: (a) the die attachment, (b) the assembly process, (c) the lamination process followed by the copper removal. Furthermore, (d) the mechanical influence of the copper vias and the polymer properties (the adhesive, the resin) are considered.

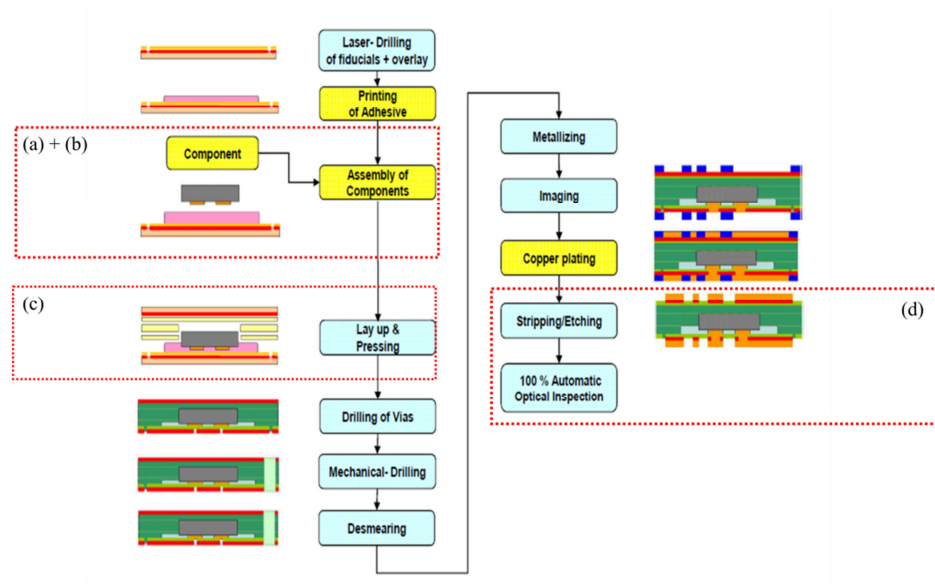


Figure 1: The embedding process chain defined by AT&S: (a) the die attachment, (b) the assembly process, (c) the PCB core lamination, (d) testing of the PCB board containing vias.

Each of the mentioned process steps is thoroughly investigated in the following chapters. Based on the obtained process knowledge design rules are proposed showing the process limitations.

2. The die attachment process

The focus of this chapter is set on the die attachment onto the copper foil by using an adhesive (Figure 2), *i.e.* the first manufacturing step within the die embedding. The die attachment is highly relevant for the embedding process, since the adhesive bond line thickness (so-called BLT) as well as the adhesive properties significantly influence the stiffness and warpage of the PCB and thus the overall reliability, linked with the aspect ratio (the ratio of the circuit board thickness to the smallest via hole diameter) when drilling vias through the adhesive. In this chapter only the flow behavior of the adhesive is considered.

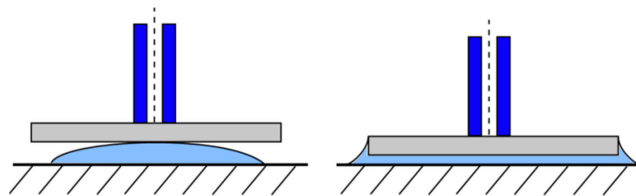


Figure 2: Schematic picture of the die attachment process.

The underlying process is described as follows: During attachment the silicon die is taken and placed with a nozzle by force on an adhesive droplet to adhere the die to the copper foil [2, 9]. The curing and shrinkage process is part of subsequent analysis of the assembly process, see chapter 3. The attachment force is in the order of a few Newton, *i.e.* from 1 to 15 N. The embedded component is a semiconductor silicon die with dimensions of 7.2 x 6.75 x 0.12 mm, see Figure 3. The die is attached face down which means that the copper-patterned side is downwards.



Figure 3: The semiconductor silicon die with copper-patterned side [9].

The adhesive droplet has a special shape, *i.e.* a pattern, which guarantees the best adhesive distribution underneath the die during and after the placement [3]. The droplet is produced by a screen printing technology, which uses a screen made of woven mesh to support an adhesive-blocking stencil layer. The attached stencil forms open areas of mesh that transfer adhesive, which can be pressed through the mesh as a sharp-edged image onto a copper foil. A squeegee is moved across the screen, forcing or pumping adhesive into the mesh openings for transfer by capillary action during the blade stroke [10].

The real adhesive droplet shape, see Figure 4, is measured with the Nano Focus method which provides a 3D surface of the droplet. The initial height of the standard droplet is 150 μm .

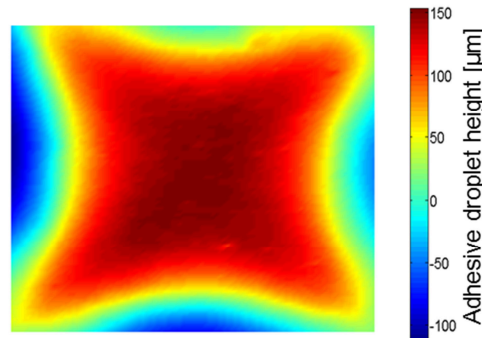


Figure 4: The real adhesive droplet shape obtained by a Nano Focus measurement [9].

Before the die is placed, the adhesive droplet is treated in a vacuum process to avoid any incidence of bubbles in the droplet due to the screen printing process. The incidence of the bubbles is undesirable, because it decreases reliability and functionality of PCBs [2, 3]. Therefore, the placement of the die is done in a cleanroom environment.

Several additional aspects of the attachment process play a significant role, *i.e.* the attachment force, the holding time and the adhesive droplet shape. The adhesive BLT and the adhesive distribution under the silicon die after the placement with respect to the attachment force, further termed *force/displacement dependency*, are investigated analytically and numerically. A part of the results has been published in [9].

2.1. Analytical description of the adhesive flow

The real adhesive flow underneath the die during the placement with all aspects mentioned above is very complex. A simplified approach to describe the *force/displacement dependency* of the die attachment is chosen here.

For simplified geometrical conditions the adhesive flow during the die attachment can be calculated analytically. In this regard the theory of a squeezing flow between parallel disks [11, 12, 13] is employed.

An axisymmetric model represents the silicon die and the adhesive droplet. Two simplified cases are investigated, a fully filled area (a constant contact area) and a partially filled area (a constant mass), which describe the adhesive droplet underneath the die, see Figure 5.

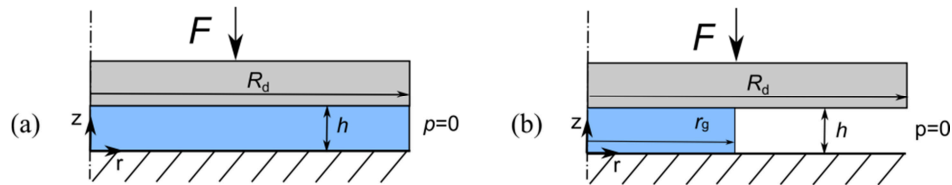


Figure 5: The analytical model for the adhesive flow during the attachment process, (a) for fully filled area under the silicon die and (b) with the simplified adhesive droplet [9].

Only the viscous shear flow of the adhesive in the radial direction is accounted for in the analytical model and all the inertia forces are neglected. The radial velocity profile is identical in each position of $0 \leq r(t) \leq R_d$. The axisymmetric model represents dies with a circular shape. Evaluation of the *force/displacement dependency* results in small errors for almost rectangular-shaped dies. The fluid is assumed to stick to the wall, *i.e.* no relative slip occurs at the wall. In Figure 5 the geometry of the analytical model is shown. On the rigid ground a viscous adhesive film is situated with an initial thickness of h_0 . The silicon die is assumed as a rigid body with a radius R_d , sitting on top of the adhesive. At the sides of the die, the pressure p is 0 Pa. On top of the component a vertical attachment force F , is applied. The actual adhesive BLT is expressed as the adhesive height $h(t)$.

Based on the real droplet shape, an equivalent disk shape droplet with radius $r_g = 2.42$ mm, *i.e.* $r(t = 0)$, and the initial droplet height $h_0 = 150$ μm is defined. The die radius is defined as $R_d = 3.375$ mm, see Figure 6.

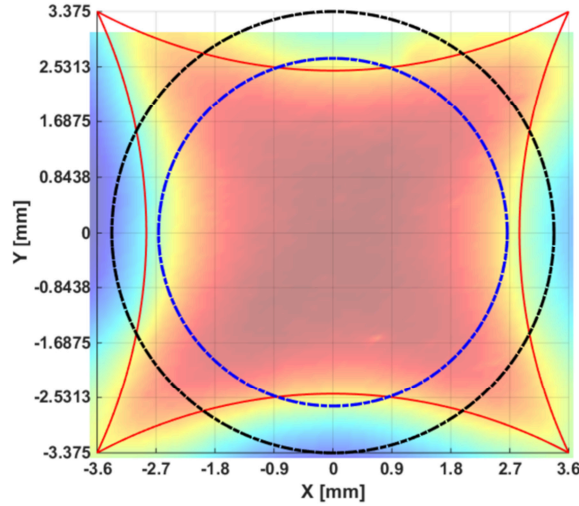


Figure 6: The adhesive droplet contour (red line) with the cylindrical droplet with a radius r_g (blue line) and the cylindrical die with a radius R_d (black line). The scale of the X- and Y-axis corresponds to the die size [9].

A brief summary of equations solving the *force/displacement dependency* based on the squeezing flow theory is given below. In general the fluid behavior is classified based on a relation between the fluid viscosity η , and the shear rate $\dot{\gamma}$, *i.e.* the rate of change of fluid deformation over time. At first, an ideal *Newtonian flow* behavior of the adhesive is assumed, which means that the viscosity is kept constant.

The adhesive flow is analytically solved by calculation of mass Eq. (1) and momentum conservation equations (the so-called *Navier-Stokes equations*) Eq. (2) [14, 15], here expressed in a general form:

$$\text{div } \vec{v} = 0, \quad (1)$$

$$\frac{\partial(\rho \vec{v})}{\partial t} + \text{div}(\rho \vec{v} \otimes \vec{v} - \vec{\tau}) + \nabla p = \rho \vec{f} + \vec{T}. \quad (2)$$

Where \vec{v} is the velocity vector, ρ stands for the density, $\vec{\tau}$ is the viscous stress tensor, p is the pressure, \vec{f} represents the body forces (*e.g.* gravity) and \vec{T} is the surface tension

force. In case (a) the adhesive completely fills the space underneath the die. Applying the assumption concerning the droplet shape [13], the *Navier-Stokes equations* simplify to:

$$\frac{\partial p}{\partial r} = \frac{\partial}{\partial z} \left(\eta \frac{\partial v_r}{\partial z} \right), \quad (3)$$

with v_r being the flow velocity in radial direction and p is the pressure in the adhesive. The symbol η stands for the shear viscosity of the adhesive. The pressure p is assumed to be constant over the adhesive thickness (the z -direction).

This equation can be solved with the boundary conditions that the pressure gradient is zero in the center of the adhesive ($r = 0$) and that the pressure p is zero at the sides of the die ($r = R_d$) [13]:

$$\frac{\partial p}{\partial r} = 0 \text{ for } r = 0, \quad (4)$$

$$(5)$$

$$p = 0 \text{ for } r = R_d.$$

With the condition of volume preservation the pressure distribution can be calculated using Eq. (6). It contains both the adhesive height $h(t)$ and the time derivate of the pressure gradient which corresponds to the vertical velocity of the die ($\partial h / \partial t$) [13]:

$$p(r,t) = -\frac{3\eta}{h(t)^3} (R_d^2 - r^2) \frac{\partial h}{\partial t}. \quad (6)$$

The integral of the pressure over the whole area of the die results in the whole vertical force F [13] on the die:

$$F = \int p(r,t) dS = -\frac{3\pi\eta R_d^4}{2h(t)^3} \frac{\partial h}{\partial t}. \quad (7)$$

The variables h and t can be separated to solve the differential equation:

$$(8)$$

$$-\int \frac{dh}{h^3} = \int \frac{2F}{3\pi\eta R_d^4} dt.$$

The *force/displacement dependency* is afterwards defined by *Stefan's equation* Eq. (9), see [13], for a *Newtonian fluid* of a constant viscosity η as:

$$h(t) = \sqrt{\frac{1}{\frac{1}{h_0^2} + \frac{4Ft}{3\pi\eta R_d^4}}}, \quad (9)$$

where h_0 is the initial adhesive droplet height, F is the attachment force, t is the loading time, and R_d is the radius simplifying the die shape.

In case (b), the space underneath the die is partly filled. The adhesive droplet is represented by a cylinder, see Figure 5, and changes its radius $r(t)$ during the loading. The viscous adhesive is assumed as incompressible so that the volume, V_0 , is constant. The adhesive height $h(t)$ development is then defined by Eq. (10) which was derived by Dienes [16] as:

$$h(t) = \sqrt[4]{\frac{1}{\frac{1}{h_0^4} + \frac{8F\pi}{3\eta V_0^2}}} = \sqrt[4]{\frac{1}{\frac{1}{h_0^4} + \frac{8Ft}{3\pi\eta r_g^4 h_0^2}}}, \quad (10)$$

where r_g is the initial droplet radius.

While Eq. (9) is restricted to *Newtonian fluids*, J. R. Scott (see also Oka) [17] extended this relationship to a *non-Newtonian fluid*, which viscosity η is related to a shear rate $\dot{\gamma}$ by a *power law* function as:

$$\eta = k\dot{\gamma}^{(n-1)}, \quad (11)$$

$$h(t) = \sqrt[{\frac{1}{n}+1}]{\frac{1}{h_0^{\frac{1}{n}+1} + \left(\frac{1}{n}+1\right) \left(\frac{F(n+3)}{2\pi k R_d^{n+3}}\right)^{\frac{1}{n}} \left(\frac{n}{2n+1}\right) t}}. \quad (12)$$

Where the symbol η stands for the shear viscosity of the adhesive, k is the consistency index, and n is the *power law* index.

If the *power law* behavior is included in Eq. (10), the relation is extended into the form:

$$h(t) = \sqrt[\frac{3n+5}{2n}]{\frac{1}{h_0^{\frac{3n+5}{2n}} + \left(\frac{3n+5}{2n}\right) \left(\frac{F(n+1)}{4\pi k r_g^{n+3} h_0^{\frac{n+3}{2}} \left(\frac{1+2n}{n}\right)^n \left(\frac{1}{2} - \frac{1}{n+3}\right)}\right)^{\frac{1}{n}}}} t \quad (13)$$

The analytical approach mentioned above is used as a basis for the squeezing flow investigation, which has been established on simplifications proposed above.

2.2. Numerical description of the adhesive flow

An enhanced investigation of the adhesive flow underneath the die is provided numerically by transient computational fluid dynamics (CFD) using the Ansys Fluent[®] software [15]. The software is based on the finite volume method (FVM) [14], which discretizes a fluid domain with linear elements without mid-side nodes. The elements themselves do not have any physical properties. They only represent a computational area. The integration points are located in the center of elements, where numerical variables (velocity, pressure etc.) are defined. Such a numerical configuration is called a *co-located scheme*.

In order to decrease the calculation time, the geometry of the die, the adhesive and the copper foil is simplified to a 2D axisymmetric model. The numerical model represents only a space underneath the silicon die, where the fluid flow takes place. Here, the adhesive droplet is placed on the copper foil (defined in the model as bottom rigid wall) and compressed by the silicon die (defined in the model as top rigid wall). At the sides of the die a pressure outlet is specified with a gauge pressure p set to 0 Pa. This interprets a static pressure of an environment where the adhesive flow exhausts. On top of the silicon die, *i.e.* the top rigid wall, the attachment force F is applied. The height of the computational area is equal to the initial height of the adhesive droplet h_0 of 150 μm (Figure 7) and it is discretized by 10 elements over the adhesive droplet height. During convergence studies it has been shown that 10 elements give an accurate

result of the flow profile of the adhesive. The top rigid wall is modelled with simplified copper conduct pads.

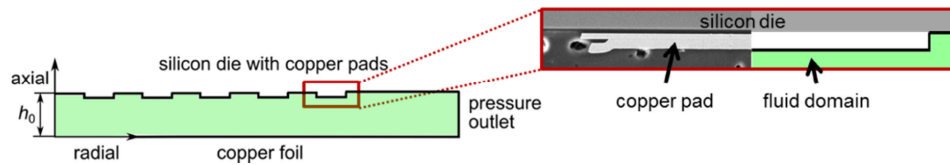


Figure 7: Schematic of a numerical 2D axisymmetric model with simplified copper pads on the silicon die.

For the adhesive flow simulation a quadrilateral Eulerian mesh is employed *i.e.* a material flows through a background mesh. The adhesive droplet is therefore not locked in the same elements over time. A quadrilateral element shape is found to be the most appropriate for the subsequent numerical techniques:

- **Volume of Fluid (VOF)**

The flow of the adhesive droplet in vacuum represents a multiphase flow with clearly defined droplet shape. The VOF method is a suitable technique for multiphase flow simulation which allows tracking a position of the interface between immiscible fluids [14, 15], *i.e.* adhesive/vacuum.

- **Dynamic mesh**

The Eulerian mesh is deformed during a die placement. If the die displacement is large compared to the local element size, the element quality can deteriorate or elements can start to degenerate. This might result in negative element volume, and consequently lead to convergence problems. In such a case, a dynamic mesh is an appropriate tool in order to change an element size and/or reduce the number of elements over time [14, 15].

- **Six Degree of Freedom (6DOF)**

This technique is a simplified fluid-structure interaction approach using in general 2D or a 3D model, where the force is applied in Fluent[®] on a rigid body. The rigid body displacement and the fluid flow are coupled and solved together [14, 15].

2.2.1. Volume of Fluid

The adhesive flow in vacuum is numerically solved by calculation of mass Eq. (1) and momentum conservation equations Eq. (2). If VOF is employed, Fluent[®] solves one set of momentum equations for all phases (adhesive, vacuum). Both phases are assumed as incompressible in terms of constant density [15].

In order to model a free surface flow of the adhesive droplet, a volume tracking method is used. Here, the tracking of the interface between the phases is realized by solution of the continuity equation Eq. (14) for the volume fraction of one of the phases. For the q^{th} phase Eq. (14) has the following form [15]:

$$\frac{\partial}{\partial t}(\alpha_q \rho_q) + \nabla \cdot (\alpha_q \rho_q \vec{v}_q) = 0, \quad (14)$$

where index q represents the adhesive, α is its volume fraction and \vec{v}_q is the velocity of the adhesive (the phase q). Further, the vacuum is indexed as the phase p .

The VOF equation is in the attachment case solved explicitly. The explicit approach applies standard finite-difference interpolation schemes to the volume fraction values that are computed in the preceding time step [15] by:

$$\frac{\alpha_q^{n+1} \rho_q^{n+1} - \alpha_q^n \rho_q^n}{\Delta t} V + \sum_f (\rho_q \dot{V}_f^n \alpha_{q,f}^n) = 0, \quad (15)$$

where V is the volume of element, \dot{V}_f is the volume flux through an element face, based on normal velocity, n is the index of the preceding time step, $n+1$ is the index of the current time step and Δt is the time increment.

The explicit approach recalculates a volume fraction in sub increments, as shown in Eq. (16). The number of sub increments is defined by a value of the *Courant number* C [15]:

$$\frac{|\vec{v}| \Delta t}{\Delta x_{\text{elem}}} < C. \quad (16)$$

Where $|\vec{v}|$ is the fluid speed, Δt is the minimum transient time increment for any element near the interface and Δx_{elem} is the element size. The advection of the interface between phases is updated once per time step. In the numerical simulation a variable time step is used to reach the defined *Courant number* C of 0.1.

The velocity fields of phase p and q are continuous across their interface. The continuity of the normal component represents a kinematic consequence with the assumption of no mass transfer across the interface [15], Eq. (17). The continuity of the tangential component is analogous to a *no-slip* boundary condition at a rigid wall [15] Eq. (18). Since the velocity vectors \vec{v}_p and \vec{v}_q are unknown, it is required to define a boundary condition connecting the state of stress in each fluid at the interface [15] by Eq. (19):

$$\vec{v}_p \vec{n} = \vec{v}_q \vec{n} = \vec{v} \vec{n}, \quad (17)$$

$$\vec{v}_p \vec{t} = \vec{v}_q \vec{t}, \quad (18)$$

$$(p_p - p_q) \vec{n} + (\eta_p \bar{\bar{\tau}}_p - \eta_q \bar{\bar{\tau}}_q) \vec{n} = \sigma \kappa \vec{n}. \quad (19)$$

Where \vec{n} is the normal to the phase interface, \vec{t} is the tangent to the phase interface, σ is the surface tension and κ is the surface curvature. p_q, p_p is the pressure and $\bar{\bar{\tau}}_p$ and $\bar{\bar{\tau}}_q$ represent tangential stress at the interface of the adhesive q and the vacuum p. η_p, η_q is the dynamic shear viscosity of the adhesive q and the vacuum p. For interface tracking the *geo-reconstruction* discretization scheme is chosen. This approach renders a clear, crisp interface without numerical diffusion.

The VOF model allows including the effects of surface tension along the interface between each pair of phases. Since the surface tension and the contact angle have significant influence on the wall adhesion as it is demonstrated in [18], the model is augmented by the additional specification of the contact angles.

2.2.1.1. Adhesive droplet shape

In case of the die attachment, the vacuum stands for the primary phase p and the adhesive for the secondary phase q . The volume fraction of the secondary phase is defined in each element. Since the adhesive droplet shape is very specific, the shape cannot be defined by standard primitives over the software interface. Therefore, the shape is implemented by a user defined function (UDF) called *DEFINE_INIT*. This function is executed once per initialization, called immediately after the default initialization and performed by the solver.

The 2D shape of the adhesive droplet cross section is obtained from the Nano Focus measurement. Here only the profile of the cross section, located in the middle of the measured 3D adhesive droplet, is used. This profile is fitted by a polynomial function and implemented into *UDF DEFINE_INIT*, see section 2.3.

After the initialization, the adhesive droplet is represented by elements with integration points lying under the fit function [15]:

$$y \leq f(x) \rightarrow \text{VOF}(\text{cell, phase } q) = 1.0. \quad (20)$$

Where x and y represent the integration point coordinates. Since the phase fraction takes the value 0.0 or 1.0, the phase interface is sharp, see Figure 8a. During the flow simulation the phase fraction is recalculated and the phase interface becomes smooth, see Figure 8b. The total volume fraction of both phases adds up to 1.0 [15].

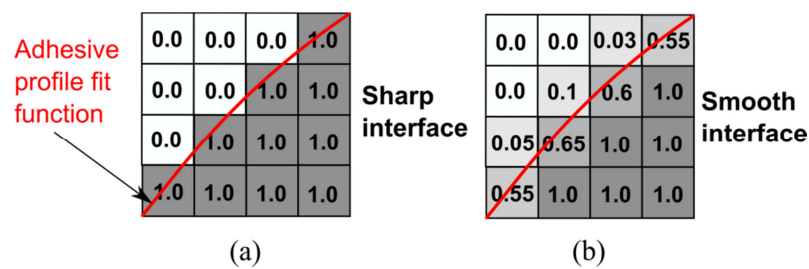


Figure 8: The adhesive droplet definition in the *Eulerian mesh*: (a) the sharp phase interface after initialization, (b) the smooth phase interface with VOF recalculation [15].

2.2.1.2. Surface tension

The surface tension is a measure of liquid resistance to the attachment force and plays an important role at adhesion. Wall adhesion is defined as a surface tension property. This so-called dynamic boundary condition results in the adjustment of the curvature of the surface near the wall.

The surface tension is numerically implemented using the Continuum Surface Force (CSF) model [15]. The surface tension force \vec{T} of CSF defined by Eq. (21) and the wall adhesion in form of surface curvature defined by Eq. (22) are introduced as additional source terms into the momentum equation Eq. (2).

$$\vec{T} = \frac{\sigma\rho\kappa_q\nabla\alpha_q}{\frac{1}{2}(\rho_p + \rho_q)}, \quad (21)$$

$$\kappa_q = \nabla \left(\frac{\nabla\alpha_q}{\|\nabla\alpha_q\|} \right). \quad (22)$$

Where ρ is the volume-averaged density of phases in an element and κ_q is the surface curvature computed from local gradients in the surface normal at the interface. The surface normal is defined as the gradient of the α_q volume fraction.

2.2.1.3. Contact angle

The wall adhesion to the silicon die and the copper foil is realized by definition of contact angles. The contact angle is a material property and is a measure of solid surface wettability, see Figure 9.

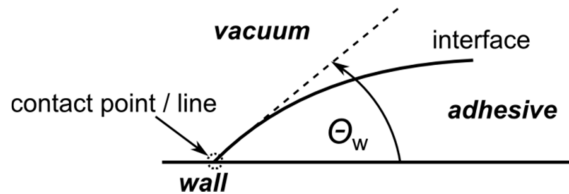


Figure 9: The contact angle Θ_w definition [15].

If Θ_w is the contact angle at the wall, then the surface normal at the element next to the wall is:

$$\vec{n} = \frac{\nabla \alpha_q}{\|\nabla \alpha_q\|} = \vec{n}_w \cos \Theta_w + \vec{t}_w \sin \Theta_w, \quad (23)$$

where \vec{n}_w and \vec{t}_w are the unit vectors normal and tangential to the wall. The vectors are calculated from the local curvature of the phase interface. The contact angles are assumed as static, *i.e.* time independent.

2.2.2. Dynamic mesh

The integral form of the conservation equation Eq. (24) expressed for a general scalar ϕ on an arbitrary control volume V can be written with respect to a dynamic mesh as [15]:

$$\frac{d}{dt} \int_V \rho \phi dV + \int_{\partial V} \rho \phi (\vec{v} - \vec{v}_G) d\vec{A} = 0. \quad (24)$$

Here \vec{v} is the flow velocity vector, \vec{v}_G is the velocity of the moving mesh, \vec{A} is the face vector, ∂V represents the boundary of the control volume V .

In the attachment case, an initial mesh modifies its size over time based on a *diffusion smoothing* method by a *boundary distance technique* with a *diffusion factor* 0. This setup changes the height of all elements in an adjacent zone uniformly. The number of elements over the whole analysis stays constant.

In general the motion of the die can be conducted by force or displacement, *i.e.* velocity controlled. In this regard geometrical boundaries of a dynamic mesh have to be defined as dynamic mesh zones with appropriate properties, *e.g.* as *stationary*, *deforming*, *user defined*, *rigid body*.

A dynamic mesh zone can be specified as follows:

- A boundary surrounding an adjacent dynamic mesh zone, which is not subjected to any deformation, is defined as *stationary*.

- A boundary, which is in contact with the moving body and changes its length during movement, has to be defined as *deforming*.
- *User defined* boundary represents the moving body, which is controlled by the displacement, *i.e.* velocity. The boundary movement is defined by a user defined function (UDF) as *DEFINE_GRID_MOTION*.
- A *rigid body* zone represents a moving body driven by force. The force is defined by UDF as *DEFINE_SDOF_PROPERTIES*. Using a force boundary condition in fluid dynamics stands for a simplified 2 way fluid-structure interaction with a rigid body called six degrees of freedom (6DOF), which is described in detail in the next section.

Slip boundary conditions at a wall are used to bound fluid and solid regions. The following options are available to model the influence of the wall boundary on the fluid mass and momentum: *no-slip*, *free slip* and *slip*, see Figure 10.

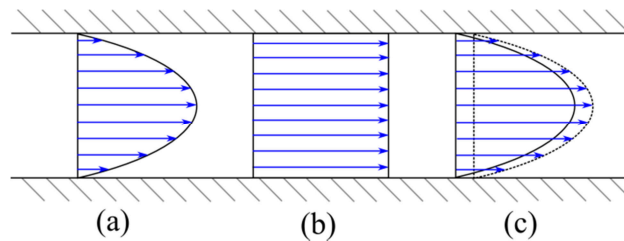


Figure 10: Velocity profile at no-slip (a), free slip (b) and slip (c) wall conditions [14].

No-slip is a default wall condition in viscous flows. It indicates that the fluid sticks to the wall, see Figure 10a. The fluid has zero velocity relative to the boundary. Such a condition is used in the analytical solution. To allow the fluid to move along a contact with the wall, a *free slip* condition is available. In this case, the velocity component parallel to the wall has a finite value, which is computed by Eq. (1) and (2), see Figure 10b. The *slip* wall condition allows the fluid to partially move along a used defined contact length with the wall, see Figure 10c.

2.2.3. The 6DOF technique

This fluid-structure interaction technique works with a rigid body, whose forces and moments are used in order to compute its translational and angular motion [14, 15]. The

subsequent motion is determined based on the solution at the current time. The linear and angular velocities are derived from the force balance on the rigid body by the six degree of freedom (6DOF) solver. The translational and angular motion is calculated for the center of gravity of the object and implemented into the dynamic mesh conservation equation, Eq. (24).

In the attachment case, the rigid body is the top wall of the 2D axisymmetric model of the fluid domain in Fluent[®]. The moving top wall manages the adhesive flow. The adhesive flow in turn influences the die displacement, *i.e.* the die displacement and the adhesive flow are coupled and solved together. During attachment only translation of the die is allowed [15], see Eq. (25),

$$\dot{\vec{v}}_g = \frac{1}{m} \sum \vec{f}_{\text{ext}}, \quad (25)$$

where $\dot{\vec{v}}_g$ is the translation acceleration of the center of gravity, m is the mass and \vec{f}_{ext} stands for the force vector of all external forces (*e.g.* the attachment force).

The 6DOF technique is established in Fluent[®] via a dynamic mesh and defined by UDF `DEFINE_SDOF_PROPERTIES`. In the attachment case `DEFINE_SDOF_PROPERTIES` contains 3 main parts:

- definition of mass and moments of inertia for the moving object,
- specification of the force loading,
- restriction of movement and rotation in/around the axis perpendicular to the loading direction.

2.3. Adhesive rheological properties

Since the adhesive flow and the BLT development are clearly dependent on the adhesive material behavior, a detailed description of the adhesive properties is summarized in the current section.

The used adhesive exhibits a *non-Newtonian* fluid behavior. A shear rate dependent viscosity is measured with a rotational rheometer, type MCR501, Anton Paar GmbH at

three different temperatures (24°C, 40°C and 60°C). The measurements are done according to ISO 6721-10, with the angular frequency range from 0.1 rad.s⁻¹ to 500 rad.s⁻¹ and in the shear rate range from 0.001 s⁻¹ to 10 s⁻¹ using a plate/plate measuring system by the Chair of Polymer Processing at the Montanuniversitaet Leoben [19]. The viscosity of the adhesive is measured in two different aging states, the new adhesive and aged one (aging under low temperature for few days). The adhesive material behavior is characterized by a *power law* model according to Eq. (11) as shown in Figure 11. Since the viscosity decreases with increasing shear rate, the adhesive represents a *shear-thinning fluid* [20]. The adhesive material coefficients are summarized in Table 1. Figure 11 shows that the adhesive aging leads to an increase of the viscosity at high shear rates.

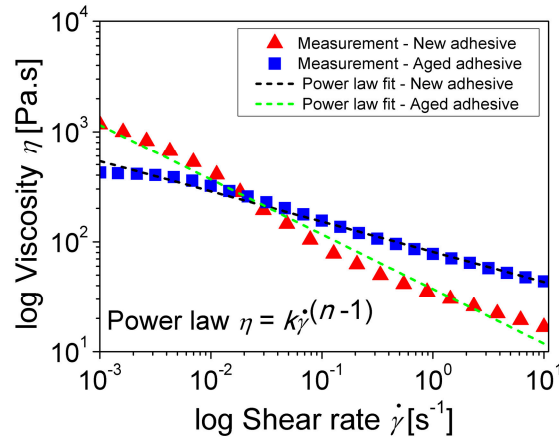


Figure 11: Shear-rate dependent viscosity of the new and aged adhesive at room temperature. The line represents a power law fit function of the experimental data [21].

Table 1: The adhesive material coefficients

Adhesive state	Consistency index k [Pa.s ⁿ]	Power law index n [-]	Density ρ [kg/m ³] [22]	Surface tension σ [N/m] [23]
New	37.19	0.503	1175	43e-3
Aged	81.09	0.726		

Since the copper foil and the silicon die have a different surface energy, the contact angles of the droplet to these surfaces differ as well. The contact angles are defined as static. From Nano Focus measurements of the adhesive droplet shape [24] the static contact angle to the copper foil is calculated as 11° [21]. The static contact angle to the

silicon die is taken from literature [25] as 50° . Since contact angles are smaller than 90° , a good adhesion is reached [26].

In the present case the adhesive droplet shape is described by a polynomial function of the 4th order by fitting of profile data of the droplet cross section obtained the Nano Focus measurement [21], Eq. (26). The cross-section is located in the middle of the 3D adhesive droplet, see Figure 12. The polynomial function of the droplet profile is implemented into UDF *DEFINE_INIT*.

$$y = -3 \times 10^6 x^4 - 7.1373x^3 - 9.1723x^2 - 9 \times 10^{-5} x + 1 \times 10^{-4}, \quad (26)$$

where x is the coordinate position in radial direction of a 2D axisymmetric model and y is the particular adhesive droplet height.

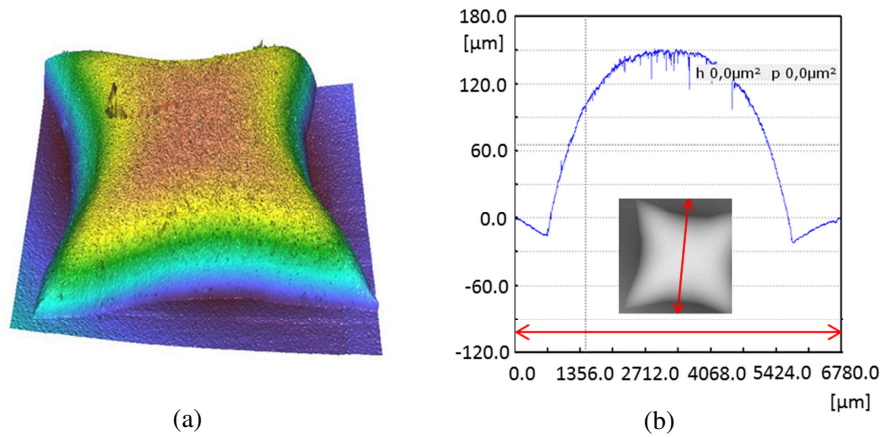


Figure 12: (a) The adhesive droplet 3D reconstruction, (b) Adhesive profile data used for a polynomial function fitting [24].

2.4. Results and discussion

2.4.1. Experimental validation

In order to validate the analytical and numerical results a design of experiments (DOE) has been carried out by AT&S [27]. Here, the silicon dies are placed with a different attachment force of 1 N, 5 N, 10 N, 15 N and a different holding time of 0 s, 2 s, 5 s and 10 s on the adhesive droplet. A final adhesive bond line thickness (BLT) is measured after the die placement and the adhesive curing using a destructive method in terms of a confocal microscopy from cross sections of assembled dies by AT&S. The

measurement is provided in 4 locations of 2 cross sections of any combination of attachment force and holding time t ; see Figure 13. The experimental results are evaluated statistically.

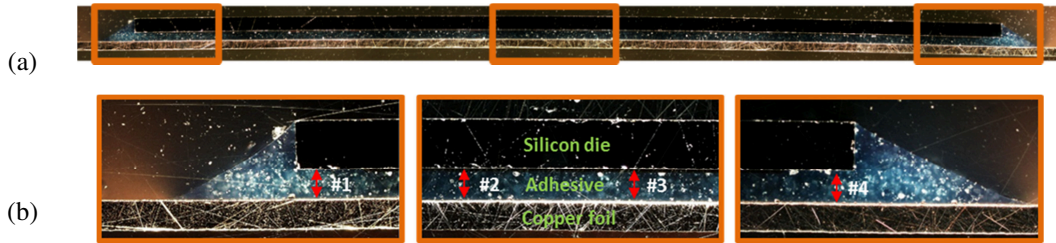


Figure 13: (a) Cross section of the die attached to the copper foil by an adhesive droplet (b) Locations of the adhesive bond line thickness measurement #1, #2, #3, #4.

Averaged experimental data obtained by a cross-section measurement are shown in Figure 14. It should be noted that due to the impossibility of in-situ measurement of BLT during the die attachment and the destructive way of the cross-sectioning, the adhesive BLT development is not determined on identical specimens.

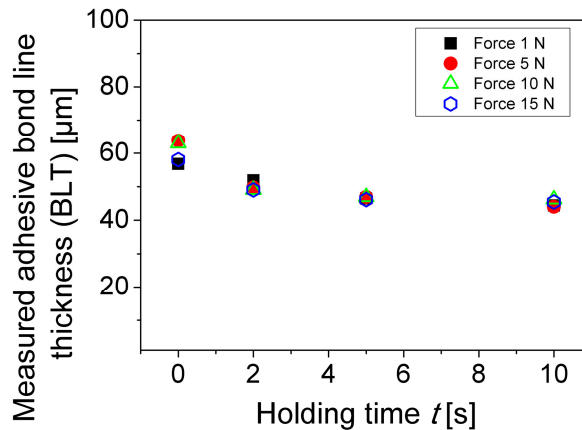


Figure 14: The averaged adhesive bond line thickness after the die placement as a function of the attachment force and the holding time.

Figure 14 shows that there is no significant difference between BLT values for the attachment forces from 1 N to 15 N. In any case, the final adhesive BLT is approx. 45 μm after a holding time $t = 10$ s.

In order to describe the adhesive BLT development analytically Eq. (13) is employed. It assumes an incompressible adhesive behavior under the premise of a

constant droplet volume. The experimental BLT data for the attachment force F of 1 N to 15 N over time are compared to the analytically derived values for both cases of the new and aged adhesive; see Figure 15-16a, b.

These figures show a clear dependence of the adhesive BLT development as a function of the holding time in both the experiment and the analytical solution. In all cases it is demonstrated that: (i) Experimental BLT reaches approx. 60 μm at very short holding time (at less than 0.1 s), *i.e.* the attachment process is highly dynamic (with high attachment speed). In this moment, the adhesive already fully fills the area under the die. (ii) A convergence of BLT is observed for a holding time of 2 s and longer.

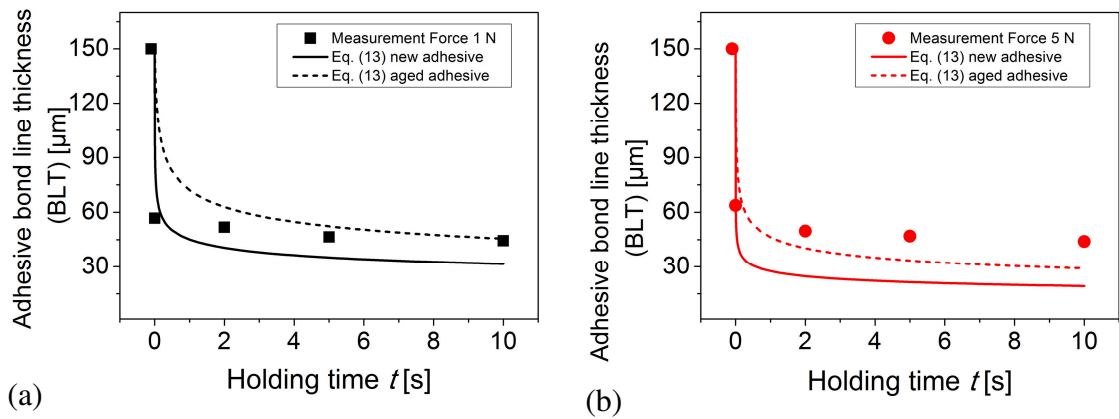


Figure 15: Comparison of experimental data and the adhesive bond line thickness development for the new and aged adhesive using analytical Eq. (13) for (a) the attachment force $F = 1$ N, (b) the attachment force $F = 5$ N.

Due to aging the adhesive is more viscous which leads to a higher BLT in comparison to the one obtained for the new adhesive. If the attachment force of 1 N is used, the analytical solution exhibits a good agreement with experimental data. The measured data lie between the analytical values of the new and aged adhesive, see Figure 15a. A higher deviation of the analytical results from the measured data is observed for the attachment forces F of 5 N and higher (Figure 15b and 16a, b). Here, the analytical approach overestimates the force impact on the adhesive flow. The experimental measurement shows that the adhesive BLT is only dependent on the holding time. The attachment force does not play a significant role.

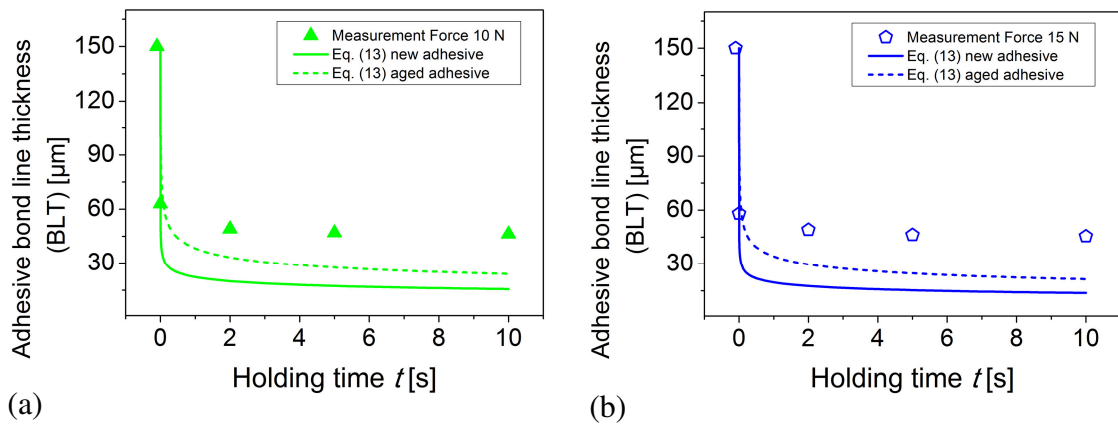


Figure 16: Comparison of experimental data and the adhesive bond line thickness development for the new and aged adhesive using analytical Eq. (13) for (a) the attachment force $F = 10$ N, (b) the attachment force $F = 15$ N.

The difference in the experimental and analytical values is explained by the following facts: At first, the axisymmetric analytical model does not take into account the “star shape” of the adhesive droplet which influences the flow conditions underneath the silicon die as it is described in [28]. Second, an initial acceleration of the attachment force during die placement is neglected. The attachment force value is not verified by measurement. A possible force overshoot during the die placement may align the measured BLT values.

2.4.2. Numerical simulation results

The numerical analysis allows including physical phenomena (surface tension, contact angle etc.), which are neglected in the analytical solution. It solves the BLT development over time as a result of a droplet adhesion and spreading under the loaded die. Nevertheless, during the numerical solution, convergence issues arise as a consequence of numerical difficulties of the attachment process. The challenges for a numerical model are twofold: (i) Two phases flow along a moving solid boundary. (ii) A force constrained solid boundary motion in a fluid domain, if the solid does not have any fixed position (two way fluid-structure interaction).

As to challenge (i): The die attachment represents a flow of an isolated adhesive drop over a dry solid surface. Here, a phase contact point appears at the front of the droplet, where the adhesive, the vacuum and the solid surface (*i.e.* the silicon die, the copper

foil) meet, see Figure 9. The shift of the phase interface is restricted to a distance between two elements. This leads to reduction of the time increment in order to reach convergence. A moving phase interface (vacuum/adhesive) at a wall boundary which is augmented by the dynamic mesh has a crucial influence on the fluid reaction force acting on the die and requires a precise specification of *slip wall conditions* for both phases.

If a *no-slip* boundary condition (the fluid sticks to the wall) is enforced at the phase contact point and there is a relative motion between the liquid and the solid (the solid boundary moves), a non-integrable singularity occurs at the phase contact point signifying an unphysical infinite force [26, 29, 30, 31], see Figure 17. This is the so-called *moving contact line problem*.

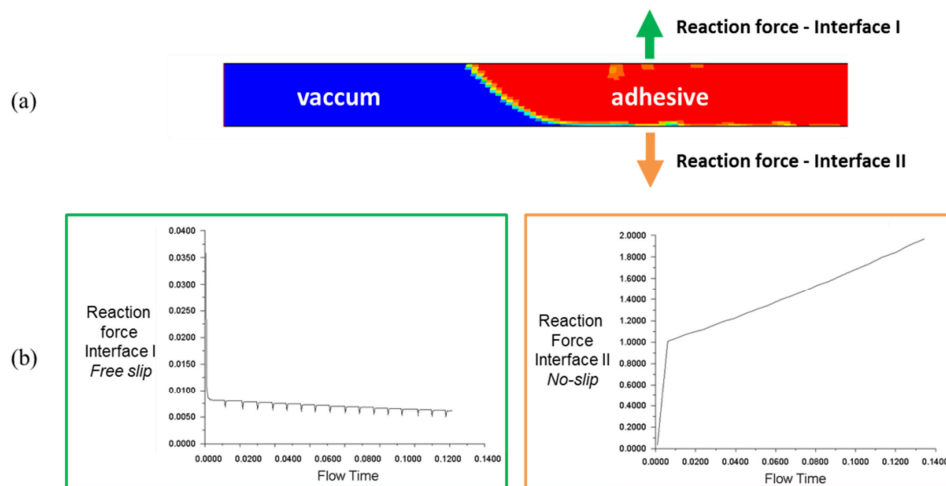


Figure 17: Moving contact line problem in a numerical simulation (a) Vacuum and adhesive distribution in a computational domain, (b) Reaction forces arising at interface I (*free slip*) and at interface II (*no-slip*).

In [32] and [33] it has been shown that the stress tensor singularity can be avoided when the fluid is allowed to slip variably near the phase contact point. This is reached by a recalculation of *free slip* and *no-slip* conditions for phases using UDF `DEFINE_PROFILE`. The *free slip* condition is defined for the vacuum/solid interface and *no slip* condition for the adhesive/solid interface, see Figure 18.

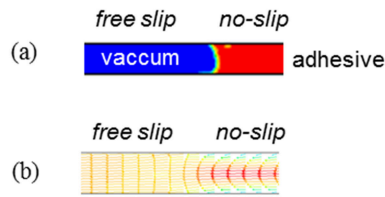


Figure 18: (a) The vacuum and the adhesive distribution underneath a silicon die, (b) Radial velocity profile of vacuum with *free slip* and the adhesive with *no-slip* condition at the wall.

As to challenge (ii): A force boundary condition considered for the die placement exhibits numerical instabilities arising in the fluid domain. These lead to an extensive calculation time which does not allow a practical use of the complex numerical simulation of the attachment process. It is observed that the numerical solution is more unstable with a higher fluid viscosity.

2.4.3. Using the analytical model in numerical simulations

As a consequence of numerical difficulties a new approach for the application of force boundary conditions has been developed. Some analogies are observed between the results of the analytically derived BLT development over time for a fully filled domain (Figure 5a) and the corresponding numerical simulation using a 2D axisymmetric model and the constant attachment force.

For the purpose of a direct comparison, the attachment case is numerically simulated using a constant adhesive viscosity. The input parameters for the 6DOF simulation are the constant adhesive viscosity of 0.1 Pa.s and the attachment force F of $1e-3$ N. The same values are used for the analytical model defined by Eq. (9). The decrease of the adhesive viscosity allows the increase of the time increment, *i.e.* $1e-5$ - $1e-6$ s. The validation of the analytical model by comparison of the BLT development with the CFD solution for a short calculation time is illustrated in Figure 19.

It is shown that the numerical results of the adhesive BLT development during the placement for the fully filled area are similar to the results of the analytical model. The difference is only about 0.35 %. One can assume that the same trend will be obtained for higher viscosities.

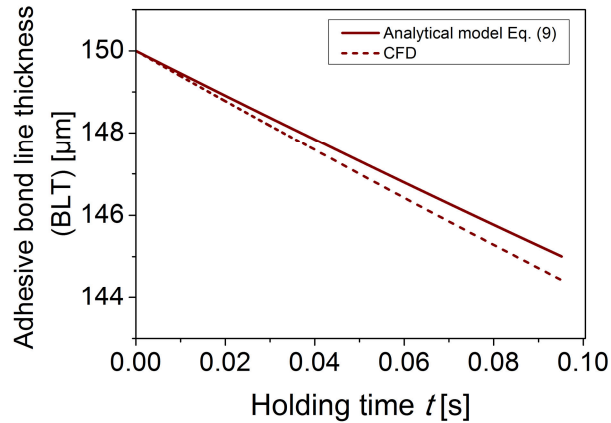


Figure 19: Adhesive bond line thickness (BLT) development for fully filled area underneath the silicon die with a radius R_d of 3.375 mm, viscosity η of 0.1 Pa.s and force F of 1e-3 N. Comparison of the analytical model Eq. (9) and the numerical (CFD) solution [9].

In order to bypass the force boundary condition, the analytically solved displacement is used as a boundary condition (the *Dirichlet-Neumann partitioning* [34]) to solve the flow of the adhesive. Thus the displacement of the die is calculated with the analytic equation for a given force and consequently applied as a boundary condition to the numerical model. This leads to a significant reduction of calculation time of the numerical simulations, since a displacement boundary condition in a fluid flow analysis entails a better convergence behavior than a force boundary condition.

2.4.3.1. Adhesive droplet shape development

In the current section the flow of the adhesive is fully governed by the die displacement based on the analytical model, Eq. (13). The adhesive has a corresponding *non-Newtonian* behavior (as defined in section 2.3). The attachment force of 1 N is applied in the analytical model. It should be pointed out that such an approach does not solve the die displacement numerically, but it is used for a precise study of the adhesive droplet shape development during the die attachment. The numerical model is 2D axisymmetric; therefore the influence of the droplet star shape is not studied. Only the adhesive profile curvature is taken into account.

The profile of the adhesive after the initial die attachment is unknown. The adhesion of the droplet to the die is not reached after VOF initialization, as shown in Figure 20a. Using a free droplet profile as an initial state for the placement causes voids between the adhesive and the component during the placement even with the *free slip* condition, see Figure 21.

To reach the defined contact angle between the silicon die/ the copper foil and the adhesive droplet, a pre-calculation with capillary effect is carried out. In such a case the adhesive flow is driven only by the surface tension and the contact angles. The obtained attached profile of the droplet is used as an initial condition for the calculation of the die placement in Figure 20b.

The development of the adhesive distribution during the die placement is illustrated in Figure 20a-c, if the *free slip* wall condition is used.

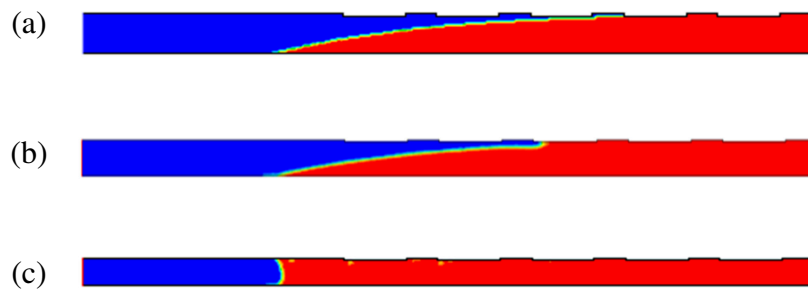


Figure 20: 2D flow model of the real adhesive droplet (red – adhesive, blue – vacuum) [9].

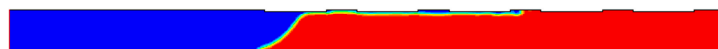


Figure 21: Free droplet profile: Numerically caused voids between the adhesive droplet and the silicon die (top wall) due to a missing initial contact between the adhesive and the silicon die [9].

During the die placement the reconstruction of the phase interfaces is provided in each time step. The shift of the phase interface is restricted to a distance between two elements. It requires the reduction of a time increment to reach convergence. Including all aspects mentioned above the numerical simulation is rather time-consuming.

2.5. Summary and conclusions

The die attachment by an adhesive on a copper foil is investigated in terms of the adhesive bond line thickness (BLT) development as a function of the attachment force F and the holding time t . The *non-Newtonian* material behavior of the adhesive and the adhesive aging are taken into account.

The analytical solution based on the squeeze flow approach is presented. The analytical results are compared with the experimental measurements of the adhesive BLT by confocal microscopy. The data show a similar trend over time. A good agreement of the results is reached for the small attachment force F of 1 N. However for high attachment forces, *i.e.* for $F = 5$ to 15 N, the absolute values of the data derived from experiments are lower than the calculated ones due to the simplifications in the analytical model. The difference in the experimental and analytical values is explained by the influence of the real adhesive droplet shape (“star shape”).

A numerical model is developed for the complex adhesive flow simulation. The model shows a way to calculate the flow under the silicon die with all physical phenomena included, such as surface tension, contact angle and real adhesive profile. It is found that application of the force boundary condition, which best corresponds to the placement process of the die, results in high numerical instabilities and thus unreasonable calculation times.

In order to bypass numerical instabilities due to the force boundary condition, the analytically solved displacement is used as a boundary condition in the numerical model. Such a procedure allows a subsequent numerical investigation of the adhesive flow with a real droplet profile and all underlying physical phenomena. A comparison of the analytical results with the six degrees of freedom (6DOF) numerical simulation shows a good agreement.

It is concluded that the analytical model allows describing the adhesive BLT development with the limitation of a small constant attachment force, when the impact of the adhesive droplet star shape is not dominant. The numerical simulation in the presented state is rather time-consuming and it is thus not suitable for industrial use.

3. The die assembly process

The assembly process deals with sticking the silicon die onto a copper foil by an adhesive [2]. This process is initiated by (i) the flow of adhesive underneath the silicon die during its placement and finished by (ii) the curing of the adhesive bond line at elevated temperature followed by cooling the assembly down to room temperature (RT). The first step has been investigated in chapter 2. In the following, the adhesive curing and cooling is described and analyzed.

Figure 22a shows a cross-section of an assembly unit, which is extracted from a board with uniformly distributed silicon dies (see Figure 22b). The investigated assembled structure represents a tri-layered laminate, which consists of a silicon die, a die attach adhesive and a copper foil.

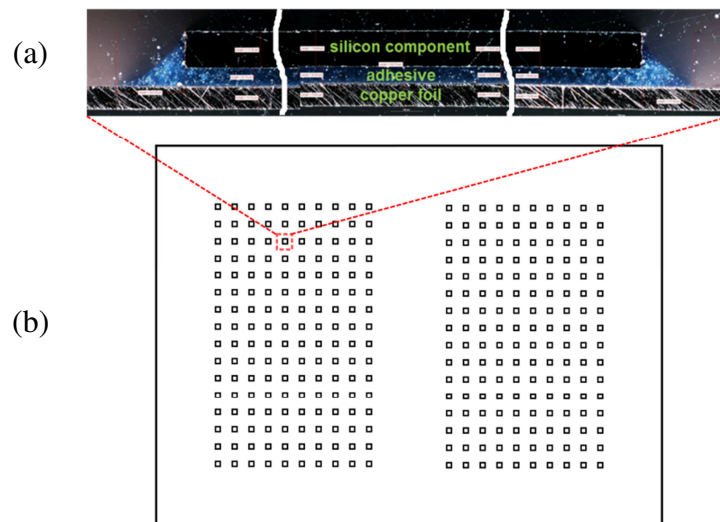


Figure 22: (a) The assembled structure in a cross-section, (b) The 24'' x 18'' copper panel with uniformly distributed dies [35, 36].

The temperature intervals for the different steps of the assembly process are illustrated in Figure 23. After the placement of the die onto the adhesive at room temperature (RT), the temperature is increased (step **A** - **D**), thus activating and speeding up the adhesive curing, *i.e.* the cross-linking in the polymer. During this process the volume of the adhesive decreases. This is referred to as cure shrinkage. As a consequence, the adhesive polymer undergoes transition from the liquid to the solid

state. Mechanically relevant cure shrinkage starts when the gel point of the cross-linking system is achieved. Thereby, the hardening of the adhesive develops continuously, leading to increasing force feedback effects on the silicon die and the copper foil. The curing is finished after certain time. Then, the package is subsequently cooled down to RT (step **E**).

In the following study the die assembly process is profoundly analyzed in terms of stresses and the package warpage, which occur due to mismatch of the coefficients of thermal expansion (CTEs) during the adhesive polymerization at elevated temperatures. The stress-strain state of the assembled structure is investigated both analytically and numerically. A part of the results has already been published in [37, 36] and described in [35].

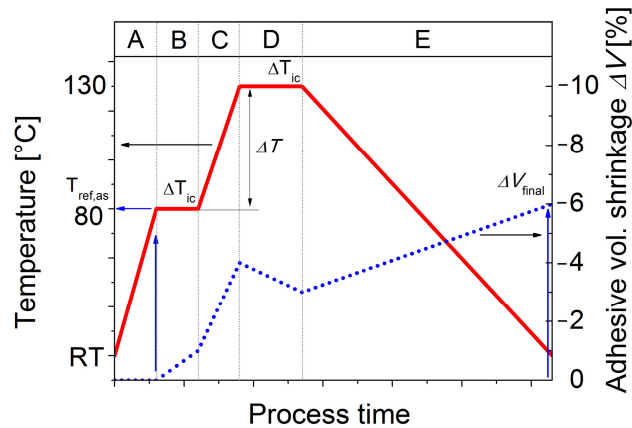


Figure 23: The temperature profile (red solid line) of the assembly process with corresponding adhesive volumetric shrinkage ΔV (blue dotted line). The temperature increase of $\Delta T_{ic} = 1^\circ\text{C}$ is used within the curing time of steps **B** and **D** in the numerical simulation [36, 37].

3.1. Analytical models

3.1.1. Classical laminate theory

The stresses in multilayer microelectronic packaging assemblies subjected to thermal loading can be predicted with analytical models. Classical laminate theory (CLT) developed by Kirchhoff [38] and enhanced by Pister and Dong [39], Reissner and Stavsky [40], and Berthelot [41] has become the background of the mechanical analysis

of laminates. This analytical solution is used to calculate the distribution of in-plane stresses and the package deformation.

In order to analyze the stresses and deflection during the assembly process CLT is applied considering the assembled structure as a laminate composite. CLT considers the plane stress state ($\sigma_z = 0$) in the laminate. A simplified geometry of the die assembly is used, in which only the area occupied by the die is considered, see Figure 24.

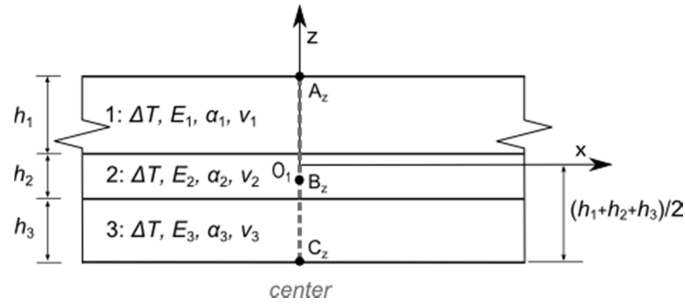


Figure 24: Schematic of the assembled structure based on the classical laminate theory (CLT). The structure consists of three layers with different material properties (E_i , α_i , ν_i) and heights (h_i), 1: silicon die, 2: adhesive, 3: copper foil [36].

CLT adopts several assumptions: (i) the interface between layers is perfectly bonded, (ii) the laminate exhibits pure bending with constant radius, (iii) the materials behave linear-elastically, (iv) transverse and normal strains in z -direction are negligible, (v) the temperature change ΔT is uniform in all layers, and (vi) the laminate is infinite in x and y -direction, *i.e.* the analytical results are evaluated far enough from free edges and corners. The total thickness of the investigated laminate is $235 \mu\text{m}$, which is considerably smaller than the length of the silicon die (7.2 mm), so that effects of the edges on the stresses and deflections in the center of the die can be neglected.

CLT consists of a comprehensive set of deformation hypotheses leading to the force-strain-curvature and moment-strain-curvature relations of the entire laminate. Furthermore, CLT allows the global laminate stiffness to be defined based on the properties of each single layer. Recalculation of the desired quantities (strain, stress) of each single layer is possible by solving for kinematic variables defining the global laminate behavior. The laminate curvature κ is determined around the geometric midplane (represented by the X -axis) with R being the curvature radius [41]:

$$\kappa = 1/R. \quad (27)$$

The elastic behavior of the whole laminate is described by a Hookean type law, which couples forces and moments, laminate stiffness and midplane deformations [41]:

$$\begin{bmatrix} \underline{N} \\ \underline{M} \end{bmatrix} = \begin{bmatrix} [A] & [B] \\ [B] & [D] \end{bmatrix} \begin{bmatrix} \underline{\epsilon}^0 \\ \underline{\kappa}^0 \end{bmatrix} - \begin{bmatrix} \underline{N}_{th} \\ \underline{M}_{th} \end{bmatrix}, \quad (28)$$

where \underline{N} and \underline{M} are vectors of external forces and moments. The ABD matrix represents the elastic properties of the entire laminate and $\underline{\epsilon}^0$ and $\underline{\kappa}^0$ are vectors of strain and curvature of the laminate midplane. \underline{N}_{th} and \underline{M}_{th} are vectors of equivalent virtual thermal forces and moments, which would have an equal strain effect due to a given temperature change ΔT .

The ABD matrix is derived based on a transformed reduced stiffness matrix Q_{ij} of each material used in the laminate. The sub-matrix A_{ij} represents extensional stiffness, the sub-matrix B_{ij} represents bending-extension coupling stiffness (which is zero for isotropic layers), and the sub-matrix D_{ij} represents bending stiffness [41]:

$$A_{ij} = \sum_{k=1}^n [Q_{ij}]_k (z_k - z_{k-1}), \quad (29)$$

$$B_{ij} = \sum_{k=1}^n [Q_{ij}]_k (z_k^2 - z_{k-1}^2), \quad (30)$$

$$D_{ij} = \sum_{k=1}^n [Q_{ij}]_k (z_k^3 - z_{k-1}^3), \quad (31)$$

where the index k stands for the layer number, and z_k is the distance from the midplane to the upper face of the k -th layer. Finally, deformation and curvature of the midplane are determined by inverting Eq. (28). The in-plane stress distribution and the curvature definition in the tri-material assembly are shown in Figure 25.

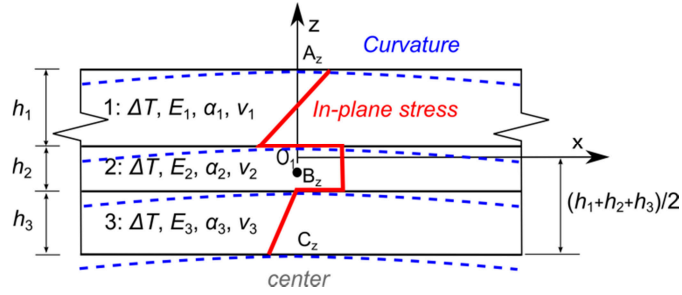


Figure 25: Schematic of the in-plane stress distribution and the curvature of the tri-material assembly using the classical laminate theory (CLT).

3.1.2. Interfacial model

The interfacial model based on the work of Sujan et al. [42, 43] allows calculating the magnitude and longitudinal distribution of interfacial stresses and the package curvature along a die half-length, L_x . The interfacial model considers the plane strain state ($\epsilon_y = 0$) in the laminate. It adopts the same assumptions (i) to (v) as CLT, as mentioned in section 3.1.1. The package geometry is simplified to the 2D laminate with a finite length equal to the die half-length, L , in x- or y-direction. The adhesive meniscus is not incorporated, see Figure 26.

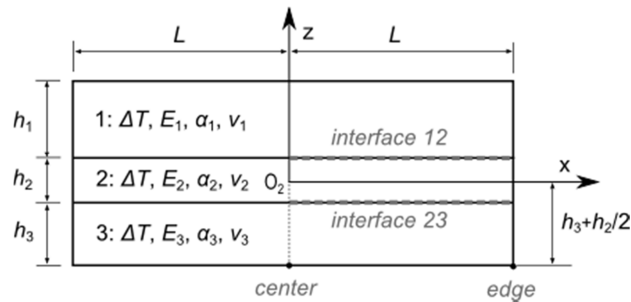


Figure 26: Schematic of the assembled structure based on the interfacial model. 1: silicon die, 2: adhesive, 3: copper foil. The coordinate system centralized in the middle of the adhesive bond line thickness (BLT) is used for derivation of stresses and strains [36].

Due to the CTE mismatch, interfacial stresses arise in the package. The interfacial stresses include shearing Eq. (32) and peeling (transverse normal) stresses Eq. (33), (34). They are responsible for adhesive and cohesive delamination of the attachment material [42, 43]. The shearing stresses, τ_i are given in a closed-form as:

$$\tau_i = A_i^{(1)} \sinh(\kappa_1 x) + A_i^{(2)} \sinh(\kappa_2 x), \quad (32)$$

where $A_i^{(1)}$ and $A_i^{(2)}$, for $i = 1, 2$, are constants which are calculated from the CTEs of the corresponding materials and geometry [42, 43]. The parameters κ_i , for $i=1, 2$, are solutions of an eigenvalues problem formulated in [42]. They depend on material and geometry parameters and the variable x defines the position along the die half-length, L .

The peeling stresses σ_i are related to the shearing stresses by:

$$\sigma_1 = - \left[a_1 \frac{d\tau_1}{dx} + a_2 \frac{d\tau_2}{dx} \right], \quad (33)$$

$$\sigma_2 = \left[b_1 \frac{d\tau_1}{dx} + b_2 \frac{d\tau_2}{dx} \right]. \quad (34)$$

Where a_i , b_i are arbitrary constants dependent on the thicknesses h_i and the flexural rigidity D_i of the i -th layer [43].

By integration of the shearing stresses, Eq. (32), the shearing forces F_i per unit assembly width are obtained:

$$F_i = \int_{-L}^x \tau_i dx = \frac{A_i^{(1)}}{\kappa_1} \{ \cosh(\kappa_1 x) - \cosh(\kappa_1 L) \} + \frac{A_i^{(2)}}{\kappa_2} \{ \cosh(\kappa_2 x) - \cosh(\kappa_2 L) \}. \quad (35)$$

The conditions of the displacement compatibility at a solid-solid interface lead to package warpage. The moment equilibrium about the positive Y-axis (perpendicular to the paper plane, see Figure 27) at x and $z = 0$ is given by:

$$M_1 + M_2 + M_3 - \frac{1}{2}(h_1 + h_2)F_1 - \frac{1}{2}(h_2 + h_3)F_2 = 0. \quad (36)$$

Where M_i is the bending moment acting over the i -th layer cross-section.

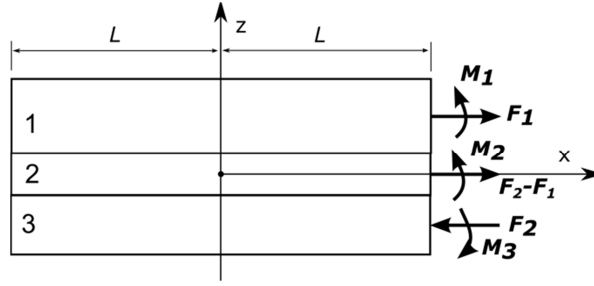


Figure 27: Shearing forces and bending moments in the tri-material assembly [43].

The conditions of the displacement compatibility in a solid-solid interface lead to the formula for the package curvature radius, R :

$$\frac{1}{R} = \left(\frac{h_1 + h_2}{2D} \right) F_1 + \left(\frac{h_2 + h_3}{2D} \right) F_2, \quad (37)$$

where $D = \Sigma D_i$, for $i = 1 - 3$, if D_i is the flexural stiffness of the i -th layer (per unit thickness of “1”), $D_i = E_i h_i^3 / 12(1 - \nu_i^2)$.

The interface shearing stress distribution and the curvature definition in the tri-material assembly are shown in Figure 28.

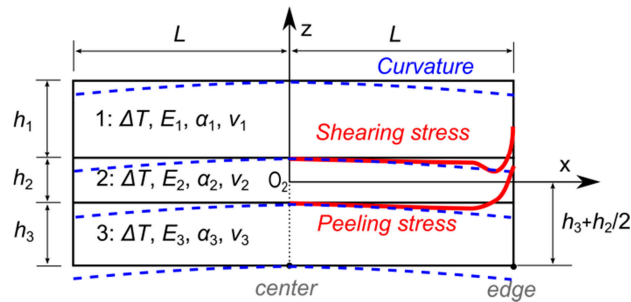


Figure 28: Schematic of the shearing and peeling stress and curvature of the tri-material assembly using the interfacial model.

3.2. Numerical model

In case of complex systems like microelectronic packaging structures, the use of the finite element method (FEM) enables the implementation of complex material models (*e.g.* elasto-plastic, phase transformations) as well as loading cases (*e.g.* adhesive curing process, cooling down etc.) to analyze critical processes during the fabrication of

printed circuit boards. The applicability of FEM to analyze the mechanical behavior of multilayer structures has been demonstrated in [44, 45, 46].

In order to investigate the stress state and the warpage caused by thermal loading during the assembly process, a FEM model is developed using the commercial finite element software ANSYS® [47]. FEA modelling of a laminated structure, whose length is significantly higher than its thickness, brings up the issue of the proper choice of the element type. After thorough convergence studies of the assembly and based on a literature review [44] an eight-node elements of type “solid185” with enhanced strain option have been chosen. To reduce the computational cost of the numerical analysis, only a quarter symmetry model is used. The silicon die is discretized by 10 elements, BLT by 4 elements and the copper foil by 6 elements over the thickness. The proposed numerical discretization is sufficient for the description of the stress-strain field in the structure. A mesh refinement close to sharp edges/corners is not applied, since edge effects, *i.e.* possible singularity, are not an objective of this study.

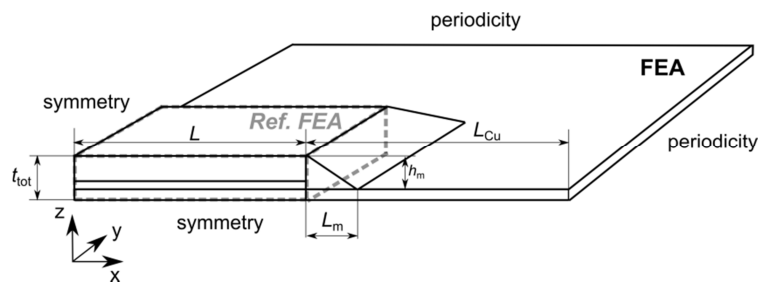


Figure 29: Numerical model of the assembled structure with boundary conditions. FEA represents a numerical model with the real assembly geometry. *Ref. FEA* is a numerical model having the same configuration as the interfacial model [36].

The numerical model incorporates the assembled structure, capturing the silicon die (flat on both sides), the adhesive with its meniscus and the copper foil. The dimensions of the modelled silicon die are $7.2 \times 6.75 \times 0.12 \text{ mm}^3$. The adhesive BLT is 0.045 mm. The copper foil has the dimensions $22 \times 22 \times 0.07 \text{ mm}^3$. The adhesive meniscus is formed during the die attachment process [9], as can be observed in Figure 22a. The meniscus is assumed as triangular shaped with a side length L_m of 0.37 mm and a height h_m of 0.165 mm. Using symmetry conditions only one quarter model of the package is modeled. When assuming an adjacent die attached to the copper foil, the copper foil length L_{Cu} is set to extend over one-half the distance between the modeled die and the

adjacent one, as shown in Figure 29. All geometry parameters, such as height, length, thickness etc., are taken from cross section measurements.

A coupling of free edges of the copper foil is chosen; this condition represents the periodic assembly. The adhesive is perfectly bonded to the silicon die and to the copper foil by means of nodes sharing the interface. This decreases the complexity of the solution and eliminates contact nonlinearities.

The adhesive curing is a transient process. However the curing kinetics is not investigated; instead a stepwise static approach is used in the numerical analysis. This methodology applies a uniform isothermal loading on the entire structure. For the case of isothermal curing steps, *i.e.* step **B** and **D** in Figure 23, the curing process is simulated by a thermal shrinkage upon a temperature increase of $\Delta T_{ic} = 1^\circ\text{C}$ within the curing time, to account for the volume change of the curing adhesive. The adhesive polymer system is assumed to have completely reacted. Consequently, all calculations refer to a stress free (initial) state, which is defined by the reference temperature ($T_{ref,as}$). $T_{ref,as}$ is set to 80°C where the mechanically relevant adhesive shrinkage starts. For the analysis, the heating-up to a curing temperature 80°C (step A in Figure 23) is not considered, because the stiffness of the uncured adhesive is negligible. The curing of the adhesive is assumed to occur progressively and homogeneously in each step.

3.3. Material properties

In order to analyze the thermo-mechanical response of the system during the attachment process, it is necessary to determine temperature dependent key properties of the involved materials. The material constants and the coefficient of thermal expansion of silicon die, adhesive and copper are determined and introduced into the analytical and numerical models. The mechanical strength of the silicon dies and the adhesive are measured. They will be compared with the stresses during the assembly process.

Special attention is given to the derivation of the volumetric shrinkage of the polymer adhesive during its phase transformation, because the cure shrinkage accounts for a significant part of the entire volume change.

Adhesive properties

The cure shrinkage measurement is particularly challenging. In this work, the adhesive volumetric shrinkage is characterized by measuring the mechanically relevant shrinkage, using a modified rheology measurement approach [48]. The adhesive volumetric shrinkage ΔV , measured by the Chair of Polymer Processing at the Montanuniversitaet Leoben [49], is represented in Figure 23 (blue solid line). The curing temperature profile (red solid line) is also shown for illustrative purposes. During heating-up of the assembly from RT to 80°C (step **A**), no volumetric shrinkage occurs. An increase of the volumetric shrinkage is observed during the isothermal curing at 80° (step **B**). At this temperature, the mechanically relevant adhesive shrinkage starts, reaching values of $\approx 1\%$. This temperature is set as the reference temperature, $T_{\text{ref,as}}$, for the stress calculations. At the following heating-up stage of the assembly to 130°C, the volumetric shrinkage increases to $\approx 4\%$ (step **C**). During isothermal curing at 130°C the volume shrinkage decreases to $\approx 3\%$, observed at the end of the curing process (step **D**). Then again an increase in ΔV is observed during the cooling down process (step **E**). The final volumetric shrinkage of the adhesive ΔV_{final} is around 6% at RT.

Since the adhesive volumetric shrinkage cannot be directly implemented into the numerical analysis, its amount is converted to an equivalent coefficient of thermal expansion, referred to as reactive CTE or $\alpha_{C,r}$. This approach is a modification of the work by Schmöller [50] and Böger [45].

The volumetric shrinkage measurement explained above provides the total shrinkage ΔV_{tot} at applied temperatures. It consists of (i) the thermal shrinkage ΔV_{therm} , caused by the adhesive CTE, and (ii) the chemical shrinkage ΔV_{chem} , related to the adhesive polymerization:

$$\Delta V_{\text{tot}} = \Delta V_{\text{therm}} + \Delta V_{\text{chem}} \quad (38)$$

Although the individual contribution of the thermal and chemical shrinkage cannot be separated during curing due to the used measurement technique, only the total shrinkage ΔV_{tot} is used for an estimation of the coefficient of thermal expansion of the

adhesive. The total volumetric shrinkage is equal to the reactive volumetric change ε_{vol} , which is converted to the isotropic reactive length change ε_{len} as:

$$\varepsilon_{\text{len}} = 1 - \sqrt[3]{1 - \varepsilon_{\text{vol}}} . \quad (39)$$

According to [50] Eq. (39) can be simplified to:

$$\varepsilon_{\text{len}} \approx \frac{\varepsilon_{\text{vol}}}{3} . \quad (40)$$

The reactive length change, ε_{len} corresponds to the thermal strain, $\varepsilon_{\text{therm}}$. Thus the reactive thermal expansion coefficient $\alpha_{\text{C,r}}$ is determined using a stepwise static approach [50] and expressed as follows:

$$\alpha_{\text{C,r}} = \varepsilon_{\text{therm}} / \Delta T , \quad (41)$$

where ΔT is the temperature change from the reference temperature $T_{\text{ref,as}}$ to the given temperature (see Figure 23).

With regard to the solution methodology $\alpha_{\text{C,r}}$ is derived for four temperature steps (from B to E). The steps **B** - **D** represent the adhesive curing, and step **E** the cooling-down to RT. In the isothermal curing steps, *i.e.* step **B** and **D**, the thermal loading is substituted by a slight temperature increase of $\Delta T = 1^\circ\text{C}$ to account for the volume change of the curing adhesive.

The adhesive elastic modulus is measured by Materials Center Leoben [51] on fully cured rectangular-shaped adhesive specimens by using a Micro-Dynamic Mechanical Analyzer (model μ -DMA RSAG2). The utilized elastic properties and the volumetric change ΔV of the adhesive at different temperatures are summarized in Table 2 and 3.

Table 2: Elastic properties of the adhesive and the adhesive volumetric shrinkage at temperature steps **B** - **E**

T [°C]	Young's modulus E [GPa]	Poisson's ratio ν [-]
20	3.43	0.30
50	3.00	0.30
115	0.08	0.39
135	0.05	0.45

Table 3: Adhesive volumetric shrinkage at temperature steps **B - E**

End of step	ΔV [%]
E	-6
B	-1
C	-4
D	-3

The flexural strength of the adhesive is measured by the Institute of Structural and Functional Ceramics at the Montanuniversitaet Leoben [51] according to the ASTM C1161 standard [30] by means of a 3-point bending (3PB) experiment (outer span $S_0=30\text{mm}$) with dimensions ($b \times t_s \times l$) 4.99 mm x 2.23 mm x 45 mm, with b , t_s and l being the width, thickness and length of the specimen, respectively. The specimen is chamfered on the tensile side to avoid failure from the edges. The experiments are done under displacement control, with a rate of 1 mm/min, in a μ Strain testing machine (Messphysik, Austria) with a load cell of 100 N. The corresponding load vs. displacement curve is plotted in Figure 30.

There is a clear linear behavior at the beginning, followed by non-linear behavior at higher loads. The flexural strength is calculated from the maximum load at failure, P , according to the following equation:

$$\sigma_{\max} = \frac{3 PS_0}{2 bt_s^2}. \quad (42)$$

The observed fracture load is 57 N, corresponding to a fracture stress of 105 MPa, according to Eq. (42).

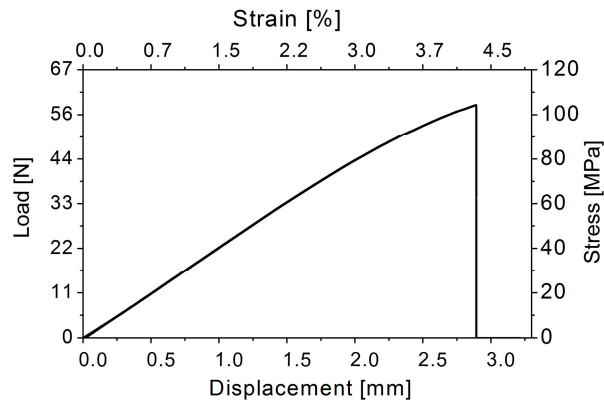


Figure 30: Load vs displacement curves of 3PB tests of an adhesive bar-shaped specimen. A linear behavior can be observed over a wide range, with a small amount of plastic deformation just before fracture [36, 52].

Silicon properties

The crystallographic orientation of a single silicon crystal die is determined by an electron backscattering diffraction (EBSD) measurement [53] by Materials Center Leoben [54]. A $\langle 100 \rangle$ -orientation is found. The orthotropic material properties according to the crystallographic orientation are taken from literature [55] and used in the numerical analysis. Only elastic properties at RT are considered in the model, since silicon remains almost invariable over the range of the processing temperatures (RT - 130°C) [56]. The elastic constants and CTE of silicon are shown in Table 4. For the analytical model calculation, isotropic material properties of the silicon of $E = 170$ GPa and $\nu = 0.3$ are applied.

Table 4: Elastic properties of standard silicon wafers in $\langle 100 \rangle$ -orientation [55, 56]

Young's modulus [GPa]	Poisson's ratio ν [-]	Shear modulus [GPa]	T [°C]	CTE [ppm/°C] Instantaneous coefficient
E_x 169	ν_{xy} 0.064	G_{xy} 50.9	20	2.6
E_y 169	ν_{yz} 0.36	G_{yz} 79.6	27	2.62
E_z 130	ν_{xz} 0.28	G_{xz} 79.6	127	3.25

Mechanical testing of commercially used silicon components with the dimensions $7.2 \times 6.75 \times 0.12$ mm³ is carried out using a miniaturized ball-on three-balls (B3B) testing jig [6] by the Institute of Structural and Functional Ceramics at the

Montanuniversitaet Leoben [57]. In the B3B method, a rectangular plate (or disc) is symmetrically supported by three balls on one side and loaded by a fourth ball in the center of the opposite side, which produces a well-defined biaxial stress field [40, 41]. The load is increased until fracture occurs, and the fracture load can be used to calculate the maximum biaxial tensile stress in the specimen at the moment of fracture. For a bulk plate of an elastically isotropic material the equivalent maximum stress, σ_{\max} , corresponding to the fracture load P is calculated as:

$$\sigma_{\max} = f \cdot P / t_s^2, \quad (43)$$

where t_s is the specimen thickness, and f is a numerically obtained dimensionless factor, which depends on the geometry of the specimen, the Poisson's ratio of the tested material, and on details of the load transfer from the jig into the specimen.

The silicon side is tested at a rate of 0.5 mm/min in ambient conditions (20°C and 50% relative humidity). A set of 15 specimens is tested to achieve statistical significance of the results. The failure stress values for each specimen (calculated according to Eq. (43)) are analyzed using Weibull statistics as commonly applied to brittle materials [58].

The characteristic strength σ_0 defined as the failure stress with a probability of 63%, and the Weibull modulus m_w are calculated using the maximum likelihood method (see Danzer et al. [59] for more details). In Table 5, the Weibull parameters along with the 90% confidence intervals are listed.

Table 5: Weibull parameters along with the 90% confidence intervals for silicon dies tested under biaxial bending using the ball-on-three-balls test.

Material	m_w	P [N]	σ_0 [MPa]
Silicon	1.6 [1.0 - 2.1]	13.7 [10.1 – 18.8]	2575 [1948 – 3638]

Copper properties

The copper foil's elastic modulus is measured using a micro-Dynamic Mechanical Analyzer (model μ -DMA RSAG2) by Materials Center Leoben [51]. Strip-shaped

specimens with the dimensions $40 \times 5 \times 0.018 \text{ mm}^3$ are loaded with a deformation amplitude of 0.02% with a frequency of 1Hz in a temperature range from 20 to 150°C. The Poisson's ratio is taken from literature [60], along with the temperature dependent CTE of bulk copper, which is taken from the materials database provided by The National Institute of Standards and Technology (NIST) [61]. All material properties are given in Table 6.

Table 6: Elastic properties of the copper foil and copper CTE [60, 61].

T [°C]	Young's modulus E [GPa]	Poisson's ratio ν [-]	T [°C]	CTE [ppm/°C] Instantaneous coefficient
20	91.80	0.34	20	16.50
50	89.77	0.34	65	17.00
100	85.77	0.34	100	17.40
150	80.83	0.34	135	17.80

The copper foil's plasticity is measured for different temperature using a micro-Dynamic Mechanical Analyzer (model μ -DMA RSAG2). The stress-strain curves are shown in Figure 31. The copper yield strength $R_{p0.1}$ is approx. 160 MPa at RT.

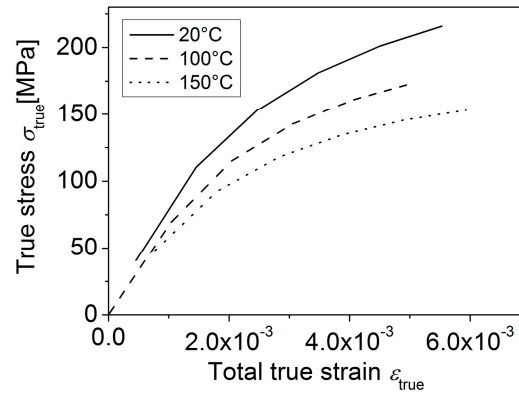


Figure 31: Copper foil plasticity data at various temperatures [36, 52].

3.4. Results and discussion

3.4.1. Deflection and validation

In the applied temperature/time range no viscoelastic/viscoplastic or creep effects are expected in the adhesive, therefore only linear elastic models are incorporated in the

analysis. During the progress of the assembly process, the stress distribution changes in the structure and the package warps. In order to determine a maximum loading of the silicon die, the warpage curvature developing in the temperature steps **B** - **E** is compared, see Figure 32b and Table 7. In addition, the maximum in-plane stress σ_x in the silicon die, in the adhesive close to the adhesive/silicon interface, and in the copper foil is estimated through the package center (the z-direction) for each temperature step. In all figures the deformations are exaggerated with a scaling factor of 10. The curvature radius, R , in the numerical model is derived by a least squares circle fit from coordinates of all points lying on the die top in the XZ-plane of symmetry, see Figure 32a.

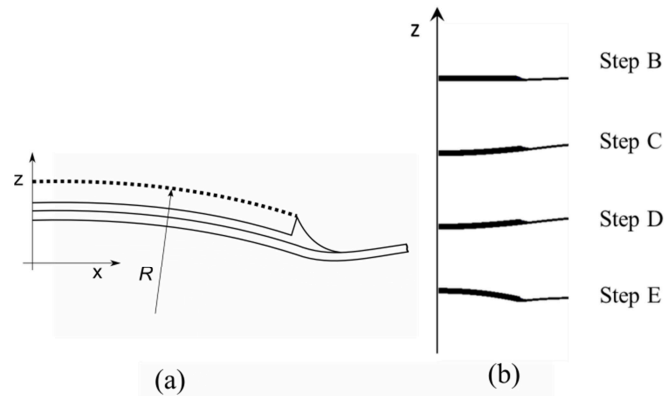


Figure 32: (a) Definition of the curvature radius, R , from points (black dots) on the die top, (b) The warpage evolution in the steps **B-E**, in the XZ-plane [35].

The analytical and numerical results are compared with experimental data obtained by X-ray diffraction method (Rocking-Curve-Technique). This analysis technique can map major warpage features non-destructively even in fully encapsulated packaged chips [62]. The rocking curve experiments of silicon dies are conducted on a D8 Discover diffractometer (Bruker AXS, Germany) in parallel beam geometry (40 kV, 35 mA, Cu $K\alpha$ radiation) by Materials Center Leoben [63]. The beam diameter is reduced by means of a circular primary baffle with 0.3 mm diameter. During the specimen scanning procedure, the detector is fixed at the Bragg angle 2θ of the crystal plane of interest and the specimen is rotated about the ω -axis (perpendicular to the diffraction plane spanned by incident and diffracted beam). For this purpose a step size $\Delta\omega$ of 0.01° and a counting time of 1 s/step are used. The scanned ω -angle is limited to the region \pm

2° near the maximum. The corresponding ω -angle refers to the direction of the lattice plane normal to the curved single crystal. The curvature κ along the x -direction at one specific point X is equal to the reciprocal radius of an osculating circle in this point: $\kappa = 1 / R$.

In order to validate the accuracy of the models, results from CLT and the numerically calculated warpage is compared with the corresponding experimentally measured data. Since the assembly process does not allow in-situ measurement of the warpage, the curvature radius, R , is measured only after cooling-down to RT, at the end of step **E**. The results obtained from CLT, FEA and XRD are summarized in Table 7.

Table 7: The curvature radius R and the maximum in-plane stress σ_x through the package center in the silicon die, in the adhesive close to the adhesive/silicon interface and in the copper foil for steps **B** – **E** obtained by FEA.

Solution step	Curvature radius R [mm]				Maximum in-plane stress σ_x [MPa]		
	CLT	FEA	XRD	Orientation	Si die	Adhesive	Copper
B	24309	46925	-	Concave	-1.5	8.1	-2.1
C	263	422	-	Concave	-37.0	51.1	-20.7
D	258	424	-	Concave	-37.2	51.3	-20.6
E	171	176	167 ± 2	Convex	51.0	94.7	-35.4

From the results it is obvious that the maximum curvature, *i.e.* the maximum loading of the silicon die, is obtained in step **E**, *i.e.* cooling-down to RT. It should be pointed out that CLT calculates the curvature radius in the center of an infinite laminate and assumes a constant curvature radius R . FEA and XRD derive the radius values from series of points on the silicon die top. Effects of the corners and simplifications in the CLT might explain the differences between CLT, FEM and XRD curvature results. A small difference in curvature/stress results between steps **C** and **D** is caused by a change of the adhesive volumetric shrinkage ΔV of 1%, see Figure 23.

To ensure that the results of all approaches are comparable and not distorted by different geometries, a reference FE analysis is conducted. The reference FE model (*Ref. FEA*) represents a laminate with a finite length $2L$ without the adhesive meniscus, *i.e.* $L_m = 0$ (Figure 29). The curvature results are shown in Table 8.

Table 8: The curvature radius, R , of the package after cooling down to RT

	CLT	Interfacial model	FEA	Ref. FEA	XRD
R [mm]	171	173 ¹ 170 ²	176	172	167 ± 2

Interfacial model: ¹ the average curvature radius R for positions $x/L = 0 - 0.95$; ² the curvature radius R in the package center $x/L = 0$.

One can conclude that both the analytical and numerical results are in a good agreement with the Rocking-Curve measurement with a difference of less than 6 %, in step **E**.

3.4.2. Stress state in the assembly

Since the dies and the copper sheet are quadratic, quarter symmetry is used. There are three important positions to evaluate the stress state: (i) the die center, (ii) the die edges and (iii) the die corners. From the symmetry in the geometry the following stress conditions are summarized. In the center there is a biaxial stress state ($\sigma_x = \sigma_y$), the stress along the edge is different from the stress perpendicular to the edge ($\sigma_x \neq \sigma_y$). Note that there is an adhesive meniscus at the edges and corners (no free surface on die sides) so that the perpendicular stresses do not become zero. Because of the quadratic shape of the dies, the stress components in the x- and y-directions are equal in the corners ($\sigma_x = \sigma_y$).

CLT and FEA are used to calculate the stress field in the assembly. FEA results of the in-plane stresses in the package center after step **E** are in good agreement with CLT results (see Figure 33). The small differences in the stress state in the die center are due to the influence of the adhesive meniscus and the outer copper foil.

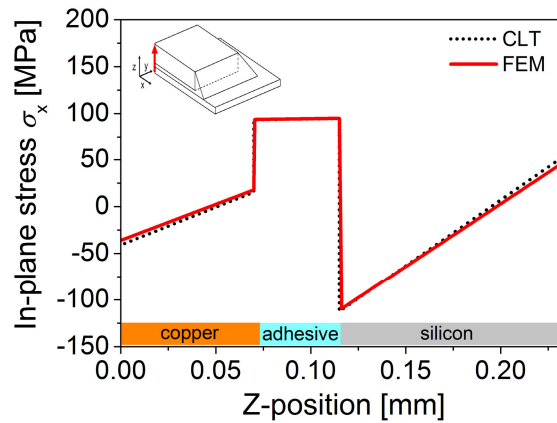


Figure 33: In-plane residual stress σ_x in the assembly center after the temperature step **E**, CLT result (black dotted line) vs. FEM result (red solid line) [35].

Figure 34 shows the maximum principal stress σ_1 on the top and the bottom of the assembly, where the highest stresses occur in the copper foil on the bottom of the assembly. Figure 35 shows the distribution of the in-plane stresses (σ_x , σ_y) calculated for the temperature step **E**. A detailed stress state evaluation is provided along the path going through the assembly center (red solid arrow), the path along the assembly edge (blue dashed arrow) and the path along the assembly corner (green dotted arrow). These paths are also illustrated in the diagrams of Figure 35.

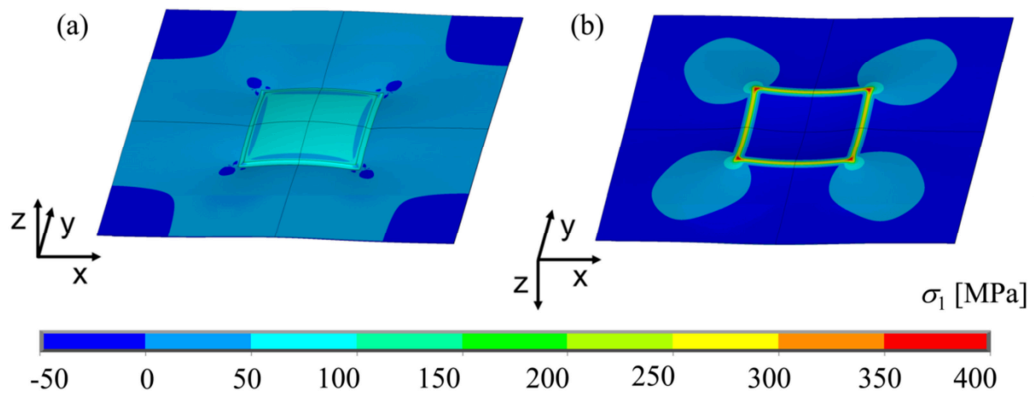


Figure 34: Maximum principal stress σ_1 [MPa] in the assembly after the temperature step **E**, (a) top view, (b) bottom view [35].

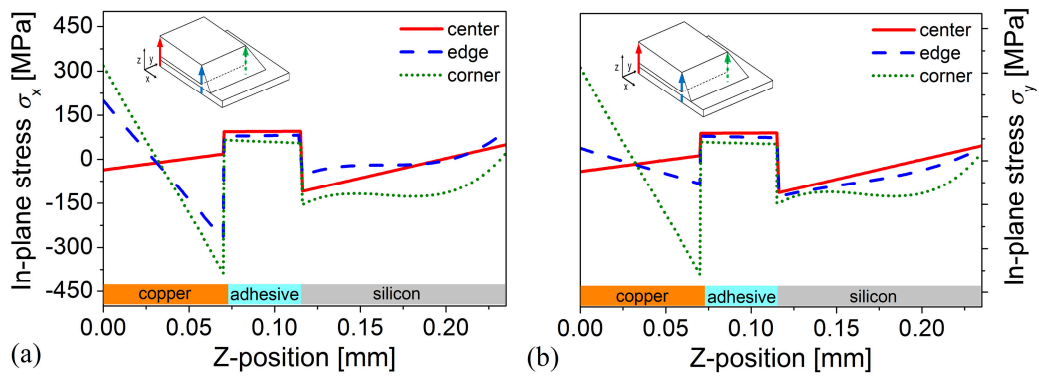


Figure 35: In-plane residual stress (a) in the x-direction (σ_x) and (b) in the y-direction (σ_y) after the temperature step **E** through the assembly center (red solid line), along the edge (blue dashed line) and along the corner (green dotted line) [35].

At the end of step **E** the assembly is warped in a convex manner with the top of the silicon die under biaxial tension $\sigma_x = \sigma_y$ of approximately 51 MPa, and the bottom of the die under compression. The meniscus of the adhesives covers the die edges and corners, resulting in non-zero biaxial stresses σ_x or/and σ_y perpendicular to the die edges/corners, see Figure 35. The maximum tensile stress, σ_x , in the die is approximately 100 MPa at the die edge.

The stresses increase in the vicinity of the sharp edges and corners of the die. In material junctions and sharp corners, singular stress fields can develop similar to stresses at crack tips [64]. In numerical models, the stresses in those regions can depend on the mesh size but stresses in other regions are calculated accurately. A singularity with stresses tending to infinity is not expected, putting aside a detailed numerical study of these material junctions.

The characteristic strength of the silicon dies is measured as 2575 MPa, as described in section 3.3. The maximum stress level induced into the silicon die after cooling-down to RT (approx. 100 MPa) is much lower than the biaxial strength and therefore not critical. Therefore, no damage occurs to the silicon die in the assembly process.

In general, the adhesive remains under tensile biaxial stresses ($\sigma_x = \sigma_y$). The maximum tensile stresses lie in the package center, where the stress magnitude is approximately 95 MPa, as shown Figure 35, with σ_x decreasing to approximately 50 MPa at the assembly corner. The measured adhesive strength of approximately 105

MPa (see section 3.3) is close to the maximum calculated stress value. However, a possible stress relaxation due to viscous mechanisms cannot be captured, since the adhesive is modelled as only linear-elastic rather than viscoelastic meaning the calculated stresses might be overestimated.

The maximum biaxial stresses ($\sigma_x = \sigma_y$) in the copper are located below the adhesive meniscus, *i.e.* close to the edges and the corners, as shown in Figure 35b. The maximum tensile stress is approx. 398 MPa and occurs on the bottom of the copper foil. Compressive stresses occur in the copper layer close to the copper/adhesive interface. The stresses emerging in the copper foil in the temperature step **E** become very high, because only a linear elastic model of copper is used in the analysis. It should be noted that after the assembly process, the copper foil is plastically deformed (irreversibly), therefore the stress magnitude should decrease, since the yield strength of the used thin copper foil is approx. 160MPa, see section 3.3.

3.4.3. Interfacial stresses in the assembly

Interfacial stresses arise at the contact area of perfectly bonded materials with dissimilar elastic constants and CTEs, especially in the case of thermal loading. The interfacial stresses have two components, the shearing stress and the peeling stress, as mentioned in section 3.1.2.

Determination of the shearing and peeling stresses in the interfaces is a very important topic in the microelectronics industry, since their extremes might overcome the interface strength and consequently lead to interface delamination [42, 65]. This is one of the most common failure modes of microelectronic packages. Nevertheless, delamination is not an objective of the thesis, therefore only the interfacial stress distribution at the assembly edge and corner is investigated and discussed. The shearing and peeling stresses are numerically and analytically evaluated along the interfaces 12 (silicon/adhesive) and 23 (adhesive/copper), as illustrated in Figure 26.

The shearing stress distribution along the assembly edge (in the XZ-plane) is plotted in Figure 36. The stress distribution in a diagonal direction to the assembly corner is shown in Figure 37. The plots start at $x/L = d/L_d = 0.8$ respectively, since the relevant

stresses arise close to sharp edges/corners. Here, d denotes the diagonal coordinate and L_d is the diagonal length of the silicon die.

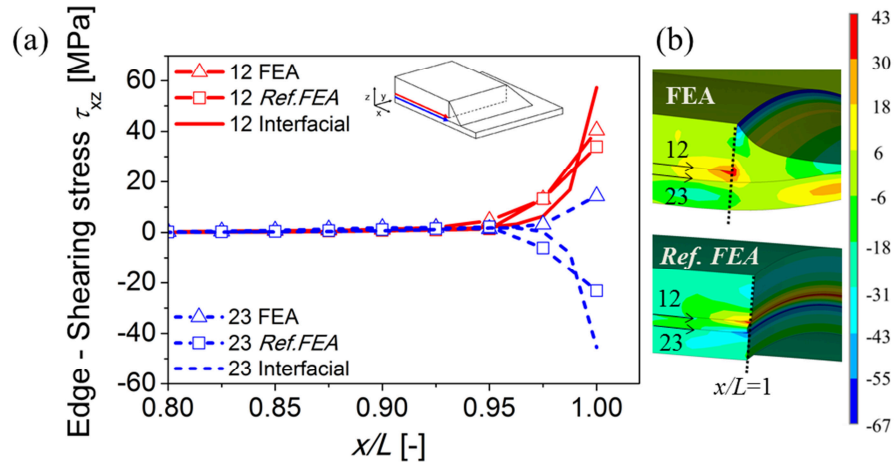


Figure 36: (a) Shearing stress distribution along the edge in the interfaces 12 and 23 evaluated by FEA, *Ref.FEA* and the interfacial model. (b) Shearing stress field in FEA and *Ref.FEA* model [36].

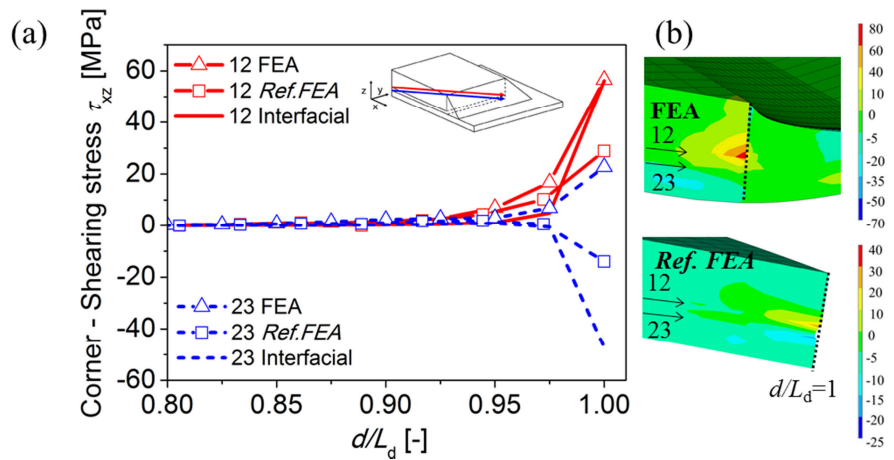


Figure 37: (a) Shearing stress distribution in a diagonal direction to the die corner in the interfaces 12 and 23 evaluated by FEA, *Ref.FEA* and the interfacial model. (b) Shearing stress field in FEA and *Ref.FEA* model.

Based on Figure 36 and Figure 37 it is shown that the resulting shearing stresses from the interfacial model are close to the numerically calculated values in all positions x/L , d/L_d respectively, except for the immediate vicinity of the sharp edges/corners at a position of approx. $x/L = d/L_d = 0.95$. It should be pointed out that in every situation of a

concave sharp edge/corner (as in the case of the adhesive meniscus) one has to expect some sort of singularity especially in the case when it is thermally loaded given different expansion coefficients for the silicon die and adhesive. A comprehensive study of a thermally loaded rectangular inclusion embedded in a surrounding matrix has been given in [66], see *e.g.* Eq. (3) therein.

In order to clarify the shearing interfacial stress distribution a field of the shearing stress τ_{xz} is plotted in the numerical models, see Figure 36b and Figure 37b. A clear stress peak is observed around the bottom edge/corner of the silicon die in the reference numerical model (*Ref. FEA*) as well as in the real assembly model (FEA). The shearing stress obtained by *Ref.FEA* model follows the same trend as the analytical results. Comparing FEA to the *Ref. FEA* it is shown that the adhesive meniscus and the copper foil surrounding the die cause an increase of the shearing stress on the interface 12 and change the shearing stress orientation in the interface 23. The shearing stresses obtained by FEA arising in the vicinity of a sharp corner (see Figure 37) are approx. 40 % higher than those at the sharp edge (see Figure 36).

The peeling stress distribution along the assembly edge (in the XZ-plane) is plotted in Figure 38. The stress distribution in a diagonal direction to the assembly corner is shown in Figure 39. The resulting peeling stresses obtained by the interfacial model significantly deviate from the numerical results. The peeling stress obtained by the *Ref.FEA* model does not even follow the same trend as the analytical results. Moreover, in previous studies [67] it has been demonstrated that the interfacial model does not describe the peeling stress distribution in the interface precisely.

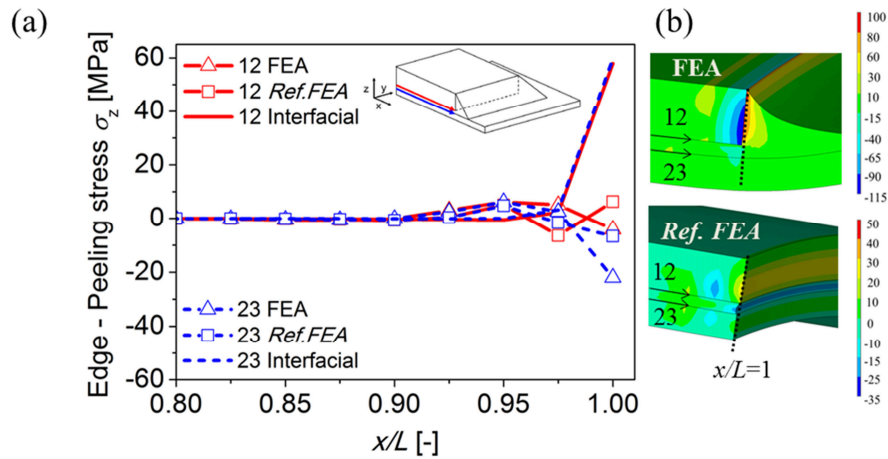


Figure 38: (a) Peeling stress distribution along the edge in the interfaces 12 and 23 evaluated by FEA, *Ref.FEA* and the interfacial model. (b) Peeling stress field in FEA and *Ref.FEA* model.

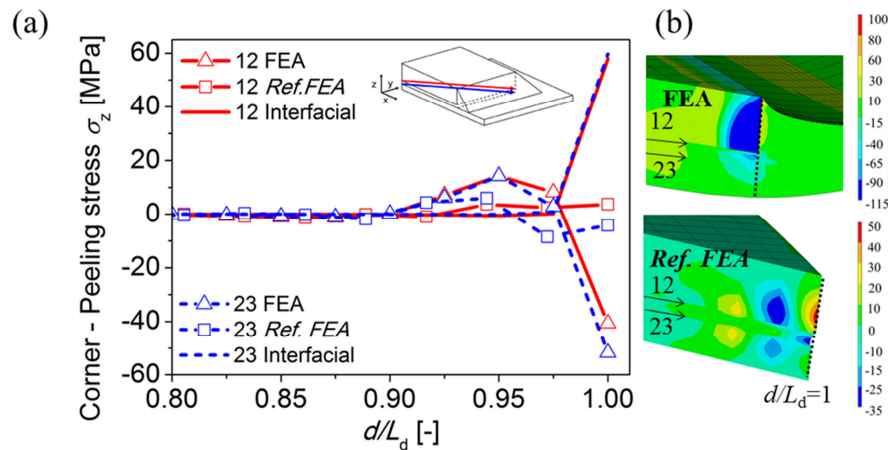


Figure 39: (a) Peeling stress distribution in a diagonal direction to the die corner in the interfaces 12 and 23 evaluated by FEA, *Ref.FEA* and the interfacial model. (b) Peeling stress field in FEA and *Ref.FEA* model.

Regarding the illustrated stresses in the interfaces it is shown that: (i) Both the shearing and peeling stresses are higher in the vicinity of the sharp corners than in the vicinity of the sharp edges. Such a behavior is commonly observed in square-/rectangular-shaped laminates and microelectronic packages due to the three-dimensional nature of delamination driving forces at corners during the thermo-mechanical loading [68]. (ii) The maximum loading arises in the interface 12, *i.e.* between the silicon die and the adhesive, where the highest difference of material CTEs takes place. This interface might be critical for the delamination.

3.5. Influence of nonlinear material behavior on a stress state in the assembly

Using a linear elastic material model (LE), the residual stresses in the copper foil and the adhesive are overestimated, because plastic deformation, which may release some of the stresses, is ignored; see Figure 34. The distribution of the maximum principal stress σ_1 in the assembly's XZ-plane is shown in Figure 40. Deformations are exaggerated with a scaling factor of 10. The stresses are: (i) above the yield stress σ_{yield} ($R_{p0.1}$) of approx. 160 MPa in the copper foil at RT and (ii) above the yield stress σ_{yield} of 80 MPa in the adhesive at RT.

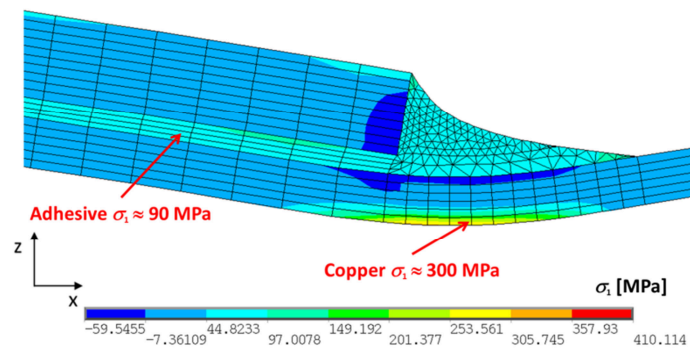


Figure 40: The principal stress σ_1 in the package after cooling to RT, in the assembly's XZ-plane for the LE model [36].

Consequently, elasto-plastic data with an isotropic hardening law are implemented in the FEA for: (i) the copper (Cu PL), (ii) the copper and the adhesive (Cu-Ad PL). The copper stress-strain curve is shown in Figure 31. Time dependency of the adhesive material behavior is neglected; for the sake of simplicity the material model is assumed as an elasto-plastic only. The plasticity of the adhesive is derived from a load-stroke curve obtained by a three-point bending (3PB), as described in section 3.3, see Figure 30. The adhesive model uses bilinear hardening with a plastic modulus of 1.9 GPa. The influence of plasticity on the curvature radius R and the residual stress in the assembly is shown in Table 9 and Table 10.

Table 9: Influence of plasticity on the curvature radius R of the package after cooling down to RT [36].

	FEA LE	FEA Cu PL	FEA Cu-Ad PL	XRD
R [mm]	176.2	175.8	178.6	167 ± 2

Based on Table 9 it is obvious that elasto-plastic behavior of copper and adhesive has negligible influence on the warpage of the assembly. The plasticity leads mainly to lower stresses in the copper and the adhesive, see Table 10.

Table 10: Influence of plasticity on the in-plane residual stress σ_x through the package center and the maximum σ_x in the entire model [36].

	σ_x [MPa]		
Position / Method	FEA LE	FEA Cu PL	FEA Cu-Ad PL
Si die top (A_z)	50.7	51.0	51.7
Adhesive (B_z)	94.2	94.2	85.7
Cu foil bottom (C_z)	-36.1	-35.0	-32.6
	Maximum σ_x [MPa]		
Adhesive (below die)	101.7	100.4	91.8
Cu (below meniscus)	381.7	227.1	223.8

If the viscoelastic nature of the adhesive were taken into account, it could lead to a relaxation of residual stresses by about 20% [69]. The LE approach is justified by the assumption of a fast assembly process, where the elastic effect is dominant as compared with the viscous effect [70].

3.6. Summary and conclusions

The attached die assembly is analyzed in terms of the package warpage and residual stresses during the assembly process. Both analytical and numerical methods are employed in the analysis. Since the analytical CLT and the interfacial model are not able to cover all geometrical aspects of the assembly, a 3D FE model is developed taking into account the real package geometry. A stepwise solution approach used in the analysis, employing only a linear elastic material model of all involved materials, is validated experimentally by the Rocking-Curve-measurement of the package warpage. Very good agreement with a relative error of less than 6 % is achieved between the analytical as well as the numerical models and the experimental measurement.

Since stresses arising in the silicon die may reach the strength limits and cause die damage, the maximum package loading during the assembly process is analyzed. Therefore, the maximum in-plane stress in the silicon die is identified after cooling the assembly down to RT.

- The maximum calculated stresses in the silicon die are clearly below the measured characteristic strength of the dies. Therefore, no die failure is predicted.
- The stresses calculated in the adhesive are in the order of the measured adhesive strength. Some plastic deformation or viscoelasticity would reduce those stresses but experiments show only a slight deviation from a linear-elastic behavior.
- Using a linear elastic material model leads to high stress in the copper layer, which are clearly above the measured value for copper yield stress of approx. 160 MPa.

By taking into account the elasto-plastic material behavior of the adhesive and the copper into the analysis, the stress peaks are reduced. Material plasticity leads to lower stresses in the adhesive and the copper. Nevertheless the influence of plasticity on the curvature radius is not significant because (i) the plastic deformations in the copper are confined to only small regions of the assembly; (ii) there are only small plastic deformations in the adhesive.

Both analytical models are limited to linear elastic material behavior. CLT is able to describe the in-plane stress distribution through the assembly center, *i.e.* far from free edges and corners. The interfacial model allows describing a stress distribution at the

material interfaces with the limitation of an idealized geometry assumption. In a case, when the silicon die edge is covered by the adhesive, the FEA results on the interface 23 (adhesive/copper foil) deviate from those obtained analytically. It is shown that:

- Both the shearing and peeling stresses are higher in the vicinity of the sharp corners than in the vicinity of the sharp edges.
- The maximum loading arises in the interface 12, *i.e.* between the silicon die and the adhesive, where the highest difference of material CTEs is found. This interface might be critical for possible delamination.

4. The lamination process

An embedded die package is produced through different steps during the embedding process [71, 37]. The focus of this work is set on the lamination during a die embedding. Here, the silicon die, which was stacked onto a copper foil by an adhesive in the assembly step, is embedded into layers of prepregs, and covered by a top copper foil using a vacuum-assisted hot press cycle. The prepregs (so-called FR-4) represent a non-conductive material made from E-glass fibers and epoxy resin. During the heat treatment of the package with different temperature and compression levels its polymer parts (adhesive, epoxy resin) introduce significant reaction forces on the silicon die due to their curing. After the lamination, conducting layers consisting of copper foils are removed / peeled off in specific areas at RT. Such a change of the package geometry significantly influences the residual stress state and warpage of the package. The copper removal is therefore included into the analysis, see Figure 41.

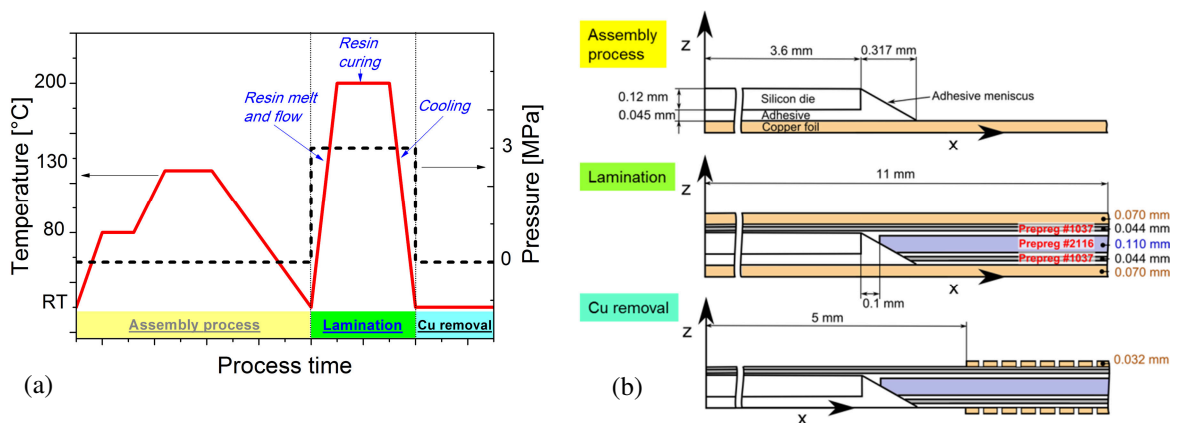


Figure 41: (a) Temperature (red solid line) and pressure (black dashed line) profile of the embedding process, (b) Investigated package after the assembly process, the lamination process and the copper (Cu) removal [52].

The press cycle of the lamination describes a relation between the applied temperature, pressure and time, see Figure 41a (lamination). The press cycle consists of three distinct parts: (i) Resin melt and flow, (ii) Resin cure, (iii) Cooling.

(i) *Resin melt and flow*: The built-up PCB is placed between preheated platens of the press. The press is closed and the PCB heats up. The resin flows at approx. 60 - 80°C

and full pressure of approx. 3 MPa is applied before the resin reaches this temperature. The heating rate as measured in the PCB is between 5°C to 8°C per minute. The press is loaded and closed as quickly as possible; in order to avoid uneven heating that will occur when only one side of a PCB is in contact with a heated platen. As the resin heats up, it becomes less viscous until it reaches its minimum melt viscosity. This is the time and temperature at which it flows and fills the cavities.

(ii) *Resin cure*: Once the resin has flowed and gelled, it needs continued heat and pressure to fully cure. The actual time and required temperature depend on the kind of resin [72].

(iii) *Cooling*: When the resin curing is finished, the package is cooled down to RT. The majority of the residual stresses are generated during cooling the package down from a hold temperature of 200°C [73].

The investigated package includes the silicon die with dimensions of 7.2 x 6.75 x 0.12 mm³. The adhesive bond line thickness (BLT) is 0.045 mm. Three layers of prepreg of a glass style #1037 and #2116 impregnated with the epoxy resin type R1551W are used for embedding. During the lamination the prepreg #1037 which contains 70% of the resin (further called RC 70%) is compressed to a post-press thickness of 0.044 mm and the prepreg #2116 RC 50% to a post-press thickness of 0.110 mm. The prepreg layers are placed symmetrically in terms of a #1037/#2116/#1037 configuration. Prepregs and copper foils have side lengths of approx. 22 x 22 mm². In order not to damage the die during their placement and compression, a cut-off distance of 0.1 mm is set between the die edge and the prepregs. The copper foil has an initial thickness of 0.07 mm. Later, the copper foil is removed above and below the silicon die in an area of approx. 10.4 x 10.0 mm². Over the rest of the package a copper pattern is created with a thickness of 0.032 mm, see Figure 41b. All nominal package dimensions are taken from cross-section measurements.

The important issue of the embedding process is the survival of the functional component, *i.e.* the silicon die, since the package is subsequently forwarded into via manufacturing and a solder mask printing process in order to create a functional PCB. In the following investigation the focus is set on a thermo-mechanical loading of a silicon die during embedding with a special focus on the lamination. The stress distribution and the package warpage are analyzed and compared with material

strengths and experimentally validated by the Rocking-Curve-Technique measurement. In this regard the influence of a resin melt and flow has been neglected. Only the lamination curing and cooling process and the copper foil removal are investigated. A part of the results has been published in [52].

4.1. Homogenization of the thermo-mechanical properties of plain woven composites

The prepreg layers are an integral part of the package and significantly influence the package stiffness, warpage and residual stresses after lamination.

The prepreg has a complex structure. It consists of a single layer of a woven E-glass cloth which is pre-impregnated with a blended epoxy resin and then partly polymerized to a ‘B-Stage’ [72]. The woven glass structure of a prepreg is made up of glass filaments that are bundled together and twisted at a set number of turns per inch to give a strand. The strands are then woven together to produce a glass cloth ready for impregnation to a ‘B-stage’. The partly cured prepreg in a ‘B-stage’ is used for the lamination, since it has several benefits: (i) the prepreg is easy to handle, (ii) the impregnated epoxy resin has still the ability to flow and to fill cavities in the package at elevated temperatures and pressure. Subsequently, during the lamination process the epoxy resin exhibits additional curing and changes to a fully cured state, a so-called ‘C-stage’. The properties of the prepreg described above allow the die embedding into the package and manufacturing of PCBs.

The utilized prepregs have dissimilar structure in x- (the so-called fill), y- (the so-called warp) and z-direction which leads to an orthotropic material behavior, see Figure 42.

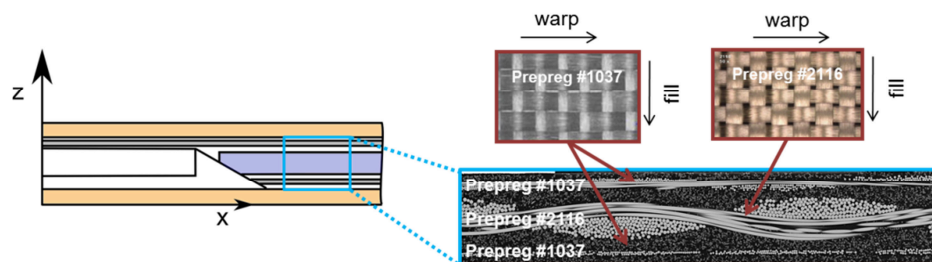


Figure 42: The structure of prepregs in the package [52].

The prepreg as a composite of the E-glass and the epoxy resin is commonly characterized by its homogenized thermo-elastic properties. In practice, the prepreg elastic properties are measured using a tensile testing or dynamic mechanical analysis (DMA). The prepreg CTE is usually determined by a thermo-mechanical analysis (TMA). The material testing is possible only in a 'B-stage' or after lamination in a 'C-stage'. Therefore in order to obtain homogenized prepreg properties containing the influence of the resin volumetric shrinkage during curing an analytical homogenization approach [74, 75, 76, 77] or a micromechanical numerical modelling of a prepreg structure [78, 79] is employed as an alternative. Necessary inputs of those approaches are the pure resin and the E-glass thermo-mechanical properties.

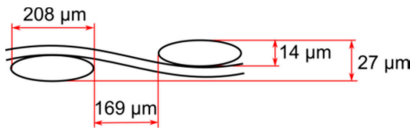
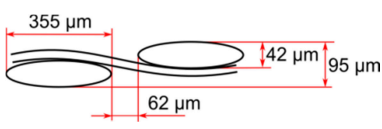
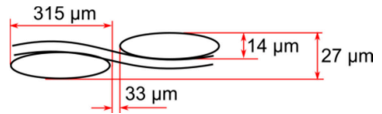
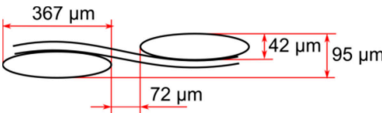
In the present work a modified analytical approach is chosen for the calculation of the homogenized prepreg properties. The approach is based on the work by Naik and Ganesh [74]. The benefit of the analytical model is shorter calculation time and less modelling effort than for a full numerical micromechanical modelling.

4.1.1. Concept of lamination theory of woven structures

The strategy of the analytical approach is simplified as follows. Based on a cross-section measurement of a glass woven structure in two perpendicular directions (the fill and the warp), a 3D geometrical model of a woven geometry is analytically reconstructed and homogenized in terms of the orthotropic thermo-elastic properties of the prepreg (*i.e.* elastic modulus, Poisson's ratio and coefficient of thermal expansion), which are analytically calculated by using concepts of lamination theory for woven composites.

The actual post-press geometry of the strands of prepreg #1037 and #2116 is summarized in Table 11. The strand cross-section has a quasi-elliptical shape and the strands are undulated in the longitudinal direction. The cross-section measurement has been provided by the Institute of Structural and Functional Ceramics at the Montanuniversitaet Leoben.

Table 11: Averaged prepreg strand dimensions based on cross-section measurements.

Direction	Prepreg #1037 strands	Prepreg #2116 strands
Warp		
Fill		

The lamination theory for woven composites adopts several assumptions. Due to the benefits of a symmetrical woven structure, the interlacing region (Figure 43a) is represented by only one-quarter and analyzed (a so-called unit cell), see Figure 43b. A real woven three materials structure is transformed to an idealized unidirectional (UD) cross-ply laminate consisting of the pure epoxy resin matrix and strands, Figure 43c. Each equivalent UD layer of the cross-ply laminate stands for one strand in the interlacing region. A detailed mathematical description of the approach is proposed below and in [74]. The analytical homogenization is performed using the MATLAB[®] software [80].

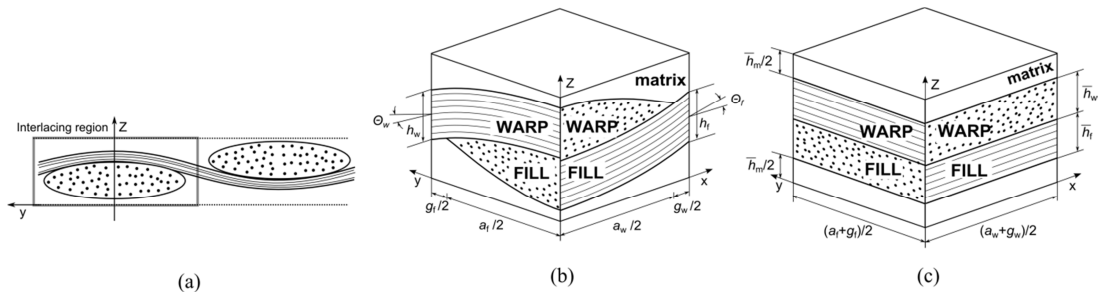


Figure 43: Concept of lamination theory of woven structures: (a) Interlacing region of a plain woven structure, (b) One-quarter model of a symmetry woven structure used for the analytical calculation (a unit cell), (c) An idealized unidirectional cross-ply laminate model representing the homogenized prepreg properties [74, 75].

In order to determine the thermo-elastic properties of the cross-ply laminate, the thermo-elastic properties of the both strands forming the cross-ply are required. Therefore the actual strand cross-section and the undulation have to be considered since they predominantly affect the strand thermo-elastic properties. For the purpose of computation, the strand cross-section and the strand undulation are defined by suitable shape functions.

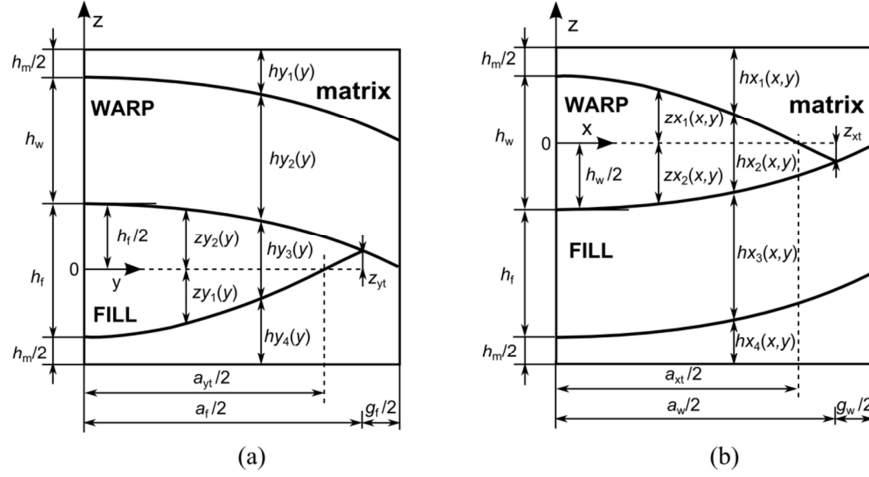


Figure 44: Parameters for the definition of strand shape functions (a) along the warp direction and (b) along the fill direction [74, 75].

The shape of a strand along the warp direction (the y-direction) is defined by sinusoidal functions [74, 75] as follows:

$$zy_1(y) = -(h_f/2)\cos(\pi y/a_f), \quad (44)$$

$$zy_2(y) = (h_f/2)\cos[\pi y/(a_f + g_f)], \quad (45)$$

Where the gap parameters a_{yt} and z_{yt} in the YZ-plane are defined as:

$$a_{yt} = \frac{\pi a_f}{2[\pi - \cos^{-1}(2z_{yt}/h_f)]}, \quad (46)$$

$$z_{yt} = (h_f/2)\cos[\pi a_f/2(a_f + g_f)]. \quad (47)$$

Here h_f is the height of the fill strand, a_f is the fill strand width, g_f is the gap between the fill strands and $zy_1(y)$, $zy_2(y)$ are the strand's shape parameters along the warp direction, as shown in Figure 44a. The shape functions along the fill direction are described in [74].

With regard to the assumed shape functions, Eq. (44) - (45) , the equation for the local off-axis undulation angle (see Figure 43b) of the warp strand is:

$$\Theta_w(y) = \tan^{-1} \left\{ \frac{d}{dy} [zy_2(y)] \right\}. \quad (48)$$

Using the prepreg overall fiber volume fraction V_f^0 as an input parameter, the strand volume fraction inside the fill and the warp tows V_f^s is calculated [74, 75] as follows:

$$V_f^s = \frac{V_f^0 V^0}{V^0 - V^{pm}}, \quad (49)$$

It should be noted that accurate computation of the strand volume fraction is the essential ingredient for the accuracy of any woven composite analysis. Here V^0 is the total volume of the computational one-quarter prepreg structure (see Figure 43b) and V^{pm} is the volume fraction of the pure resin matrix.

$$V^0 = (a_f + g_f)(a_w + g_w)H_L, \quad (50)$$

$$V^{pm} = (a_f + g_f)(a_w + g_w)\bar{h}_m, \quad (51)$$

where H_L is the total prepreg thickness and \bar{h}_m is the mean thickness of the resin matrix in the cross-ply laminate, as shown in Figure 43c.

$$\bar{h}_m = H_L - (\bar{h}_f + \bar{h}_w), \quad (52)$$

the mean thicknesses of the fill strand \bar{h}_f and the warp strand \bar{h}_w are defined [74] below:

$$\bar{h}_f = \frac{2}{a_f + g_f} \int_0^{a_f/2} [zy_2(y) - zy_1(y)] dy, \quad (53)$$

$$\bar{h}_w = \frac{2}{a_w + g_w} \int_0^{a_w/2} [zx_1(x, y) - zx_2(x, y)] dx, \quad (54)$$

where a_w is the warp strand width, g_w is the gap between the warp strands and $zx_1(x, y)$, $zx_2(x, y)$ are the strand shape parameters along the fill direction.

The homogenized orthotropic thermo-elastic properties are calculated in five steps as follows:

(i) *Transversally isotropic properties* of the warp and the fill strand are calculated for the actual strand volume fraction V_f^s . The strands are idealized as an equivalent straight UD lamina. In this regard the composite cylinder assemblage (CCA) is employed. Its detailed description is provided in [81].

(ii) The calculation of *local reduced compliance constants* $S_{ij}(\Theta_k)$ for $i, j = 1, 2, 6$ and index $k = w$ (the warp), f (the fill) is shown [74, 75] below:

$$S_{11}(\Theta_k) = \frac{1}{E_L(\Theta_k)}, \quad (55)$$

$$S_{22}(\Theta_k) = \frac{1}{E_T}, \quad (56)$$

$$S_{66}(\Theta_k) = \frac{1}{G_{LT}(\Theta_k)}, \quad (57)$$

$$S_{12}(\Theta_k) = \frac{\nu_{TL}(\Theta_k)}{E_T(\Theta_k)}, \quad (58)$$

where E_L , E_T , G_{LT} , ν_{TL} , α_L , α_T are thermo-elastic properties of a UD lamina obtained by CCA. The subscript index T represents the transversal direction and the index L is for the longitudinal direction.

The *local reduced thermal expansion coefficients* $\alpha_i(\Theta_k)$ for $i = 1, 2$ are defined as:

$$\alpha_1(\Theta_k) = \alpha_L \cos^2 \Theta_k + \alpha_T \sin^2 \Theta_k, \quad (59)$$

$$\alpha_2(\Theta_k) = \alpha_T. \quad (60)$$

(iii) *Effective averaged compliance constants* $[\bar{S}_{ij}]_k$ and *effective averaged thermal coefficients* $[\bar{\alpha}_i]_k$ in the warp and the fill strand are calculated by integrating along the strand length. It is assumed that the strand takes a circular path, so the expressions for

the effective constants and coefficients of the fill and warp strands in the one-quarter model are written [74, 75] as:

$$[\bar{S}_{ij}]_k = \frac{1}{\Theta_k^{\max}} \int_0^{\Theta_k} S_{ij}(\Theta_k) d\Theta, \quad (61)$$

$$[\bar{\alpha}_i]_k = \frac{1}{\Theta_k^{\max}} \int_0^{\Theta_k} \alpha_i(\Theta_k) d\Theta, \quad (62)$$

where the integral is divided by the maximum undulation angle Θ_k^{\max} .

(vi) Since in the case of a plain woven laminate bending deformations of the unit cell are constrained by the adjacent unit cell, the unit cell is subjected only to in-plane loading [74, 75]. Therefore only *extensional constants* appear in the *stiffness matrix* A_{ij} and in the *thermal stress resultants* N_i^T as:

$$A_{ij} = \frac{[(\bar{Q}_{ij})_f \bar{h}_f + (\bar{Q}_{ij})_w \bar{h}_w + (\bar{Q}_{ij})_m \bar{h}_m]}{H_L}, \quad (63)$$

$$N_i^T = \frac{\Delta T}{H_L} [(\bar{Q}_{ij})_f (\bar{\alpha}_i)_f \bar{h}_f + (\bar{Q}_{ij})_w (\bar{\alpha}_i)_w \bar{h}_w + (\bar{Q}_{ij})_m (\bar{\alpha}_i)_m \bar{h}_m]. \quad (64)$$

Where $\bar{Q}_{ij,k}$ are *transformed strand stiffness constants* calculated as:

$$\bar{Q}_{ij,k} = \text{inv} [\bar{S}_{ij}]_k. \quad (65)$$

Finally, the thermo-elastic properties of the woven laminate are determined in the fill direction (the x-direction) using the following equations:

$$E_x = A_{11} - \frac{A_{12}^2}{A_{22}}, \quad (66)$$

$$G_{xy} = A_{66}, \quad (67)$$

$$\nu_{xy} = \frac{A_{12}}{A_{11}}, \quad (68)$$

$$\alpha_x = \frac{(A_{22} N_1^T - A_{12} N_2^T)}{\Delta T (A_{11} A_{22} - A_{12}^2)}. \quad (69)$$

4.2. Numerical model

Due to the complexity of the package geometry, a finite element analysis is employed for the stress-strain investigation of the embedding process. The numerical analysis is conducted with the commercial finite element software ANSYS® [47]. Since the lamination follows the assembly process, the presence of residual stresses in the package due to its assembling clearly influences the laminate’s mechanical response. To include the influence of the assembly process, the process flow is simulated applying a corresponding temperature and pressure level on the package, see Figure 41.

The following strategy is applied for the embedded process simulation:

- All temperature steps of the embedding process are numerically modelled, see Figure 41. Elasto-plastic material behavior of the adhesive and the copper is used in the analysis in order to preserve plastic deformations arising in the package during the assembly process.
- The package is modelled as 2D axisymmetric to simulate the complexity of a 3D geometry with the additional benefit of a reduced calculation time. For the analysis quadratic elements of type “plane183” are employed [47]. The geometry is discretized by elements with a size of 0.01 mm, which has been determined as an optimum after thorough convergence studies. For illustrative purposes a comparison of different numerical models of the package with the corresponding calculation time is shown in Table 12 and Figure 45.

Table 12: Comparison of numerical models used for the embedding process simulation with a corresponding calculation time (FEA performed on a PC cluster with two 64-bit 6-core processors Xeon X5650 (2010)).

	2D “plane 183”	2D axisym. “plane 183”	3D quarter model “solid 185”
Number of elements	42.965	42.965	947.919
Calculation time	Seconds	Seconds	Hours

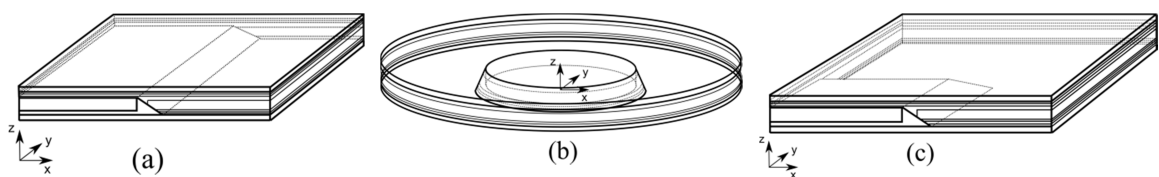


Figure 45: Geometrical representation of numerical models: (a) 2D model with symmetry condition, (b) 2D axisymmetric model, (c) 3D quarter symmetry model.

- The overall embedded package is modelled and subjected to the temperature history according to Figure 46. The laminated structure and particular parts of the package are deactivated / activated in the corresponding process steps; see Figure 47a. This is done using a numerical technique based upon “element death” and “element birth” [47]. In the assembly process (**B** - **E**), the prepregs, the epoxy resin and the top copper foil are initially deactivated. In the lamination (**F** - **G**) the prepregs, the epoxy resin and the top copper foil are activated in the structure. Finally, in step **H** the corresponding parts of the copper foil are deactivated to mimic the copper removal, see Figure 47a, b.
- The reference temperature of the assembled and the laminated structure is dissimilar corresponding to different curing profiles of the adhesive and the epoxy resin. The reference temperatures are defined in points where significant polymerization of the adhesive / the epoxy resin starts to occur. The assembled structure (step **B** - **E**) and the top copper foil have the reference temperature $T_{\text{ref,as}}$ set to 80°C according to the adhesive curing [37]. The laminated prepregs and the epoxy resin have the reference temperature $T_{\text{ref,lam}}$ set to 200°C according to the epoxy resin curing. A detailed description of the reference temperature estimation is shown in section 4.3.
- The curing kinetics of the adhesive and the epoxy resin is not investigated; instead a stepwise static approach is adopted [45]. A uniform isothermal loading is applied on the entire structure. The adhesive and the epoxy resin polymer systems are assumed to be completely reacted. Consequently, the calculations are referred to a stress free (initial) state, which is defined by the reference temperatures as mentioned above. The curing of the adhesive and the epoxy resin is assumed to occur progressively and homogeneously.

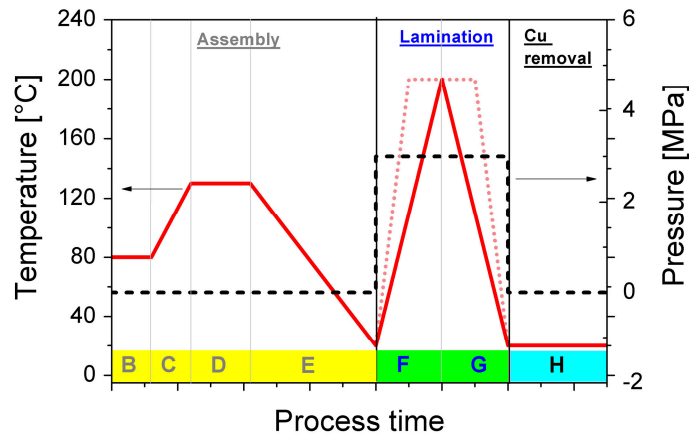


Figure 46: Computational steps of the embedding process simulation with the corresponding applied temperature and pressure [52]. The change of the lamination temperature (from red dotted line to red solid line) profile is described in section 4.3.

The copper pattern is numerically simplified to a continuous layer with a reduced copper thickness of $12.75 \mu\text{m}$, see Figure 47b. The reduced copper thickness is calculated based on the assumption that the continuous copper layer has the same volume as the copper pattern. It should be mentioned that the copper pattern reinforces the prepreg layers in the area surrounding the silicon die, but it does not influence the residual stresses inside the area of the silicon die.

The preregs are numerically modelled as a tri-layered structure consisting of the pure epoxy resin, a homogenized composite of the epoxy resin and the E-glass, see Figure 47c. The homogenized composite has a thickness equal to the overall thickness of a glass cloth. The thickness of the epoxy resin layer and the glass cloth is taken from cross-section measurements. The homogenized glass cloth properties are obtained using the analytical model described in section 4.1.1. A deformation of the prepreg #1037 and #2116 due to contact with the adhesive meniscus is neglected, see Figure 48.

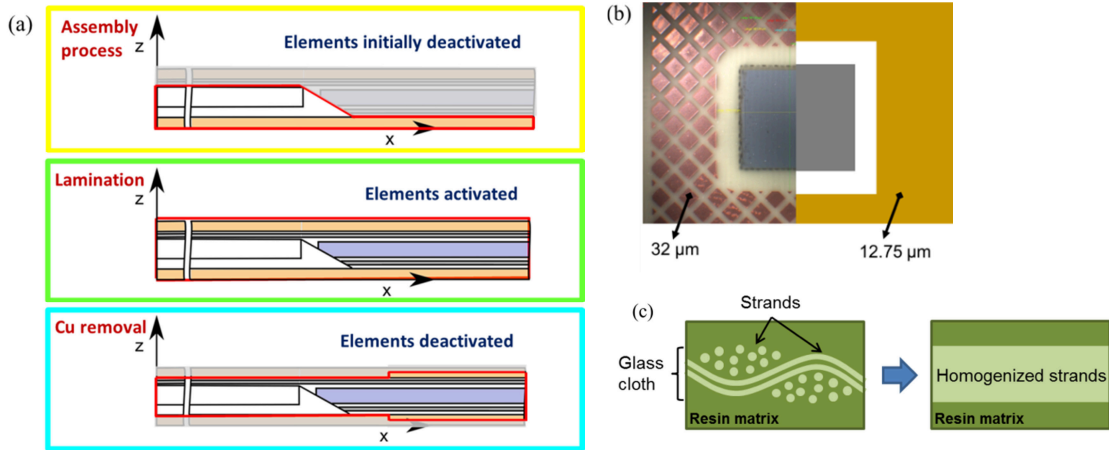


Figure 47: (a) Numerical model of the embedded die package in particular manufacturing steps, i.e. the assembly process, the lamination and the copper (Cu) removal, (b) Real copper pattern and its simplification in the FEA model, (c) Real prepreg structure and its simplification in the FEA model [52].

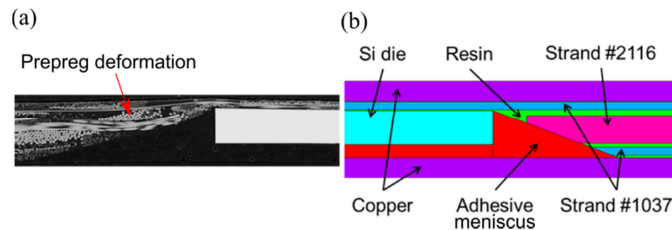


Figure 48: (a) Cross-section of the embedded die package showing prepreg deformation in contact with the adhesive meniscus, (b) Numerical simplification of prepregs in contact with the adhesive meniscus.

Since only a single die package is investigated, the free edges of the package are coupled to simulate the presence of adjacent ones. The adhesive, the epoxy resin and the prepregs are perfectly bonded to the assembled structure as different materials sharing nodes at the interface. The PCB placed between preheated platens of the lamination press (step **F-G**) is numerically simulated by applying a pressure on the top copper foil along with nodes coupling in the z-direction. The copper foil bottom nodes are fixed in the z-direction to mimic the solid support of the bottom platen, see Figure 49. These conditions are removed in the following step **H** of the copper removal.

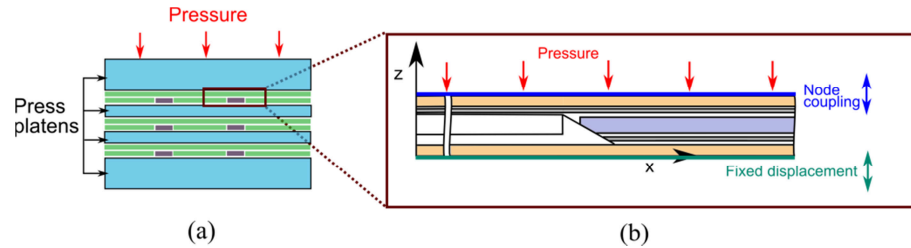


Figure 49: (a) Schematic of the lamination press [46], (b) Boundary conditions of the package fixed between preheated platens in the lamination (step **F** - **G**) [52].

4.3. Material properties

The embedded die package consists of up to 6 materials, *i.e.* copper, adhesive, silicon, resin and composites of resin and E-glass represented by the prepregs of type #1037 and #2116. In order to analyze the thermo-mechanical response of the package during the process, it is necessary to determine temperature dependent key properties of the involved materials. To be able to simulate the process flow, elasto-plastic material data of the copper and the adhesive are used in the analysis in order to preserve plastic deformations arising in the package during the assembly process. Their elasto-plastic material data are shown in chapter 3, section 3.3. The silicon is modelled as linear elastic with the material properties equal to those published in chapter 3.

An additional measurement of the adhesive's coefficient of thermal expansion is presented, since it is already fully cured after the assembly process. Special attention is given to the derivation of the volumetric shrinkage of the polymer resin during its phase transformation, because the cure shrinkage is a significant part of the entire volume change. In the applied temperature/time range no viscoelastic/viscoplastic or creep effects are expected in the resin, therefore only a linear elastic model is used in the analysis. The elastic constants and coefficients of thermal expansion of the epoxy resin R1551W and the prepregs type #1037 and #2116 are determined and introduced into the numerical model.

The mechanical strength of the silicon dies and the adhesive are measured and compared with the residual stresses in the package during the lamination process.

Cured adhesive properties

The utilized adhesive belongs to thermosets which show on irreversible curing behavior; therefore the adhesive is fully cured after the assembly step. The adhesive elastic modulus is measured on fully cured rectangular-shaped adhesive specimens by using a Micro-Dynamic Mechanical Analyzer (model μ -DMA RSAG2), as described in chapter 3.3. The development of the adhesive Young's modulus E as a function of temperature is shown in Figure 50a. The adhesive Poisson's ratio is the same as in Table 2.

The development of the CTE of a fully cured adhesive as a function of temperature was measured using thermo-mechanical analysis (TMA) by AT&S [51]. The adhesive specimens with initial length of 0.29 mm were axially loaded by a small constant force of 0.1 N. The glass transition temperature T_g is observed around 100°C. The development of the CTE is plotted in Figure 50b.

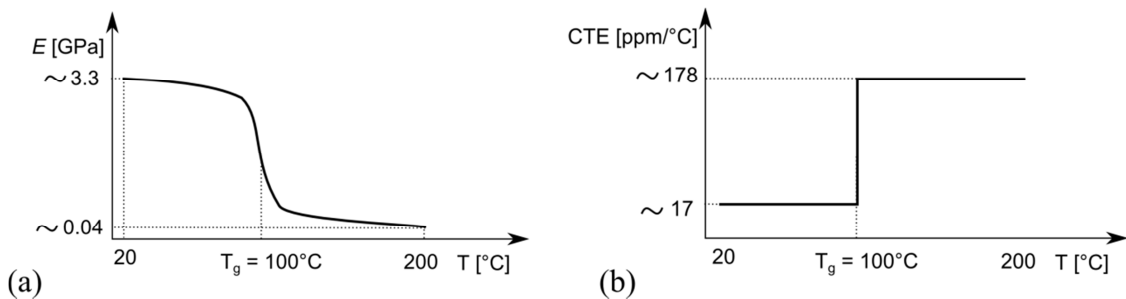


Figure 50: Idealized graphs of fully cured adhesive thermo-elastic properties: (a) Young's modulus E as a function of temperature, (b) Coefficient of thermal expansion CTE as a function of temperature. A clear softening of the material is observed at the glass transition temperature T_g of approx. 100°C.

Epoxy resin properties

The resin's volumetric shrinkage is characterized by measuring the mechanically relevant shrinkage, using a modified rheology measurement approach [48]. The measured volumetric shrinkage ΔV (blue solid line) and the curing temperature profile (red solid line) are represented in Figure 51a. The package heating-up and an isothermal curing at 200°C have only negligible influence on the mechanically relevant shrinkage, since (i) below 200°C the resin is in a liquid or a semi-liquid state causing practically no

relevant loading of the package, (ii) there the resin's volumetric shrinkage is below 0.5%. As a result the reference temperature $T_{ref,lam}$ is set to 200°C and the temperature profile is simplified to only heating-up and cooling-down in the analysis as shown in Figure 46 and Figure 51a, b. The total volumetric shrinkage of the epoxy resin ΔV_{final} relative to $T_{ref,lam}$ is approx. -5% at RT. The major part of the residual stress is generated during the cool-down from the final hold temperature [73].

The resin's CTE is determined using a stepwise static approach [50], which is a modification of the work by Schmöller [50] and Böger [45], as presented in chapter 3.

The epoxy resin is modelled as linear-elastic. The Young's modulus E of the resin R1551W is estimated based on a comparison of the homogenized modulus of a prepreg glass type #1080 with the resin R1551W measured by a dynamic-mechanical analysis (DMA) and homogenized values determined by the analytical homogenization approach, as described in section 4.1.1. The DMA measurement is provided in a fully cured state, *i.e.* 'C-stage'. The glass transition temperature T_g is observed at approx. 150°C. The development of the Young's modulus as a function of temperature is shown in Figure 52. The Poisson's ratio ν is taken from literature [22, 23] as 0.35 below T_g and 0.45 above T_g .

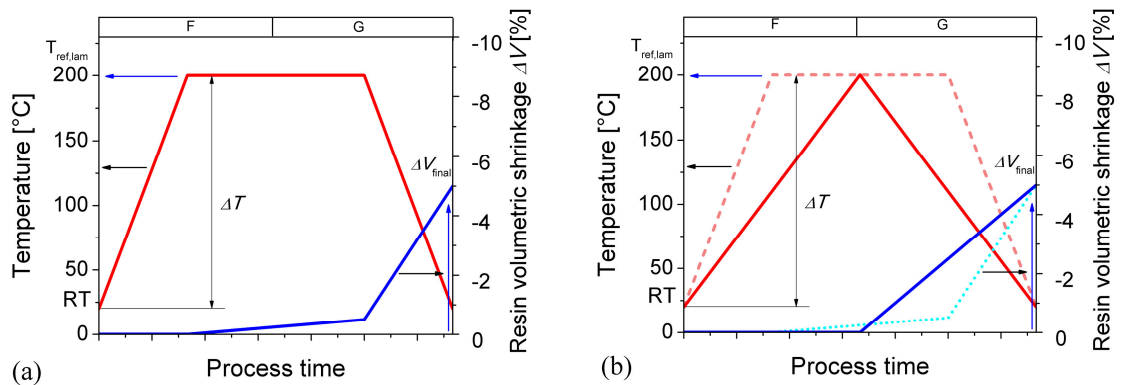


Figure 51: (a) Real resin curing profile (red solid line) with a volumetric shrinkage ΔV (blue solid line) development, (b) Simplification of the resin curing profile (from pink dashed to red solid line) and a volumetric shrinkage ΔV (from cyan dotted to blue solid line) used in the FEA.

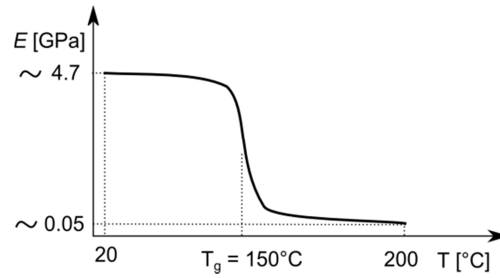


Figure 52: Idealized graph of Resin's Young's modulus E as a function of temperature. The softening of the material is around the glass transition temperature T_g of approx. 150°C .

E-glass properties

The fibers of the prepreg cloth are made of E-glass, which is an aluminoborosilicate glass with less than 1% w/w alkali oxides (percent concentration weight/weight). Linear elastic material properties of the E-glass are taken from literature [74, 78]. At RT the E-glass Young's modulus E is 72 GPa, the Poisson's ratio ν is 0.22 and the coefficient of thermal expansion CTE is 5.4 ppm/°C. In the current investigation E-glass properties are assumed as temperature independent.

Prepreg orthotropic properties

The prepreg's thermo-elastic properties are determined based on the lamination theory of woven structures, as described in section 4.1.1. Based on the knowledge of the linear elastic properties of the resin matrix, the E-glass fibers and the prepreg strand geometry, the orthotropic properties of prepreg type #1037 and #2116 are derived and shown in Table 13 and Table 14. It should be mentioned that the homogenization is done only in a region of a prepreg glass cloth as described and illustrated in Figure 47. Prepreg orthotropic properties are temperature dependent. The referred prepreg reactive CTE combines a chemical effect due to polymerization in the curing phase and a thermal effect in the cool down phase, as it has been estimated using a stepwise static approach [37, 45].

Table 13: Homogenized orthotropic properties of prepreg #1037 at RT containing the influence of the resin curing shrinkage.

Young's modulus	[GPa]	Shear modulus	[GPa]	Poisson's ratio	[-]	Reactive CTE	[ppm/°C]
E_x	21.1	G_{xy}	4.2	ν_{xy}	0.1928	α_x	25.6
E_y	18.4	G_{xz}	4.1	ν_{xz}	0.3759	α_y	40.7
E_z	14.8	G_{yz}	4.1	ν_{yz}	0.3759	α_z	50.2

Table 14: Homogenized orthotropic properties of prepreg #2116 at RT containing the influence of the resin curing shrinkage.

Young's modulus	[GPa]	Shear modulus	[GPa]	Poisson's ratio	[-]	Reactive CTE	[ppm/°C]
E_x	23.7	G_{xy}	5.7	ν_{xy}	0.2020	α_x	31.5
E_y	23.9	G_{xz}	5.5	ν_{xz}	0.3939	α_y	31.3
E_z	16.6	G_{yz}	5.5	ν_{yz}	0.3939	α_z	47.5

4.4. Results and discussion

In order to validate the accuracy of the model, the numerically calculated warpage is compared with the corresponding experimentally measured data obtained by an X-ray diffraction method (Rocking-Curve-Technique). A detailed description of a Rocking-Curve-measurement setup is given in chapter 3.4. The curvature is determined on the silicon die top, see Figure 53a, b. The assembly and the lamination processes do not allow in-situ measurement of the warpage. Moreover, the top copper foil absorbs the X-ray beam. The experimental investigation shows that a Rocking-Curve X-ray beam has the ability to transmit through the prepreg #1037 covering the silicon die and reflecting from the die [82]. As a result, the curvature can be measured after the assembly (**E**) and the copper removal (**H**) step at RT.

In the numerical model the curvature radius R is determined from node coordinates on the die top, when a final value of the curvature is derived by a least squares circle fit method with the software Matlab[®] [80].

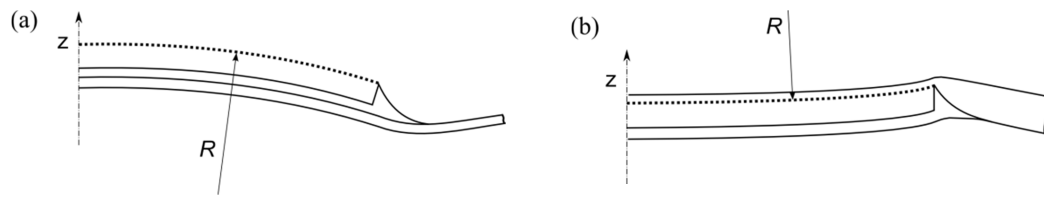


Figure 53: The curvature radius R definition in (a) the assembled structure, (b) the laminated package [52].

The aim of the analysis is twofold: (i) to determine warpage of the package during the embedding process, (ii) to evaluate the stress maxima in the package during the embedding process with the purpose of the assessment of a possible package failure. The survival of the silicon die is a crucial issue of the embedding process, because the package is afterwards processed by manufacturing the copper vias and a solder mask printing [2], where the functional PCB is finally produced. The curvature results obtained by FEA and XRD are summarized in Table 15.

Table 15: The curvature radius R development after the assembly step **E**, the lamination step **G** and the copper removal step **H**, in comparison with a Rocking-Curve-measurement [52].

Step / Technique	Curvature radius R [mm]		
	Assembling Step E	Lamination Step G	Cu removal Step H
FEA 2D axisym.	181.5	26789.0	486.4
XRD	165 ± 7	-	500 ± 7
Error [%]	9	-	3
Warpage	Convex	Convex	Concave

The initial convex warpage of $R = 181.5$ mm after the assembly process (step **E**) is significantly reduced to a practically flat package of $R = 26789.0$ mm in the lamination (step **G**) due to the package compression. In step **H** the package is released from the press and the copper foils are removed.

This causes a partial release of residual stresses and results in an additional package deformation in an opposite concave manner with $R = 486.4$ mm, see Figure 54c. During the lamination, residual stresses in the epoxy resin are higher than those in the adhesive, because only the epoxy resin exhibits a significant volumetric shrinkage due to its

curing. The fully cured adhesive does not melt and cure again in the lamination process because it is a thermoset.

From the results in Table 15 it can be inferred that the maximum curvature is reached after the assembly process in step **E**. The numerical results are in very good agreement with the experimental ones. After the assembly process the difference amounts to less than 9% and after the lamination followed by the copper removal to less than 3%.

Figure 54 shows the distribution of the maximum principal stress σ_1 in the overall package at the end of (a) the assembly process, (b) the lamination process and (c) the copper removal. All deformations are exaggerated by a scaling factor of 10. The location of stress peaks changes upon altering the loading conditions, the package configuration (*e.g.* presence of prepregs, copper foil etc.) and the warpage direction.

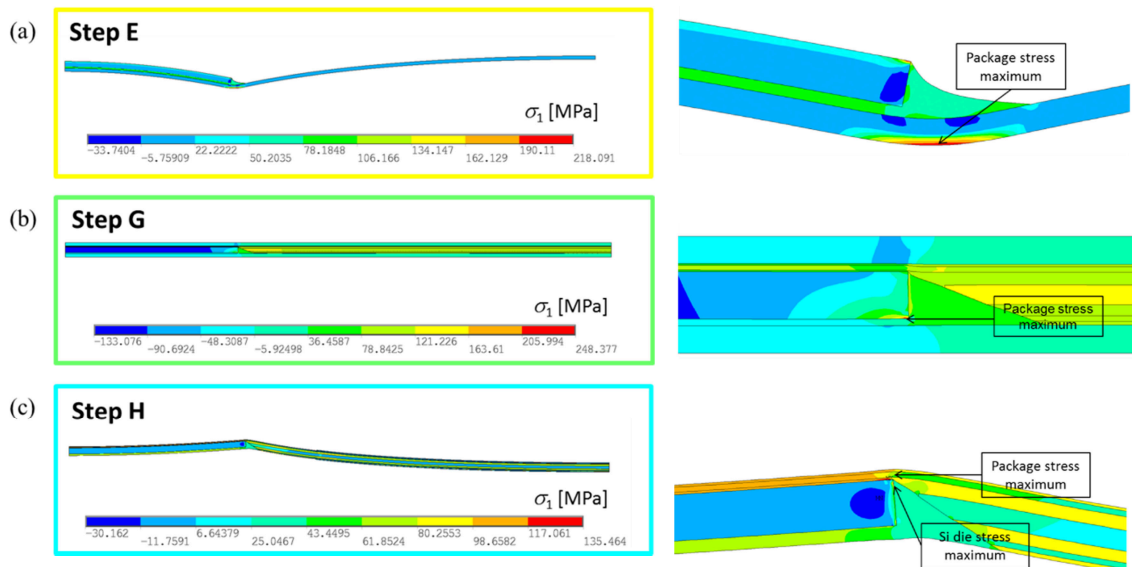


Figure 54: Maximum principal stress σ_1 [MPa] in the overall package at the end of (a) the assembly step **E**, (b) the lamination step **G** and (c) the copper removal step **H** [52].

After the assembly process (**E**), the highest residual stress arises in the copper foil under the adhesive meniscus, with σ_1 being approx. 218 MPa, see Figure 54a. Due to the lamination, the stress peak moves to the silicon die bottom edge, see Figure 54b. The maximum principal stress σ_1 there reaches approx. 248 MPa. It should be mentioned that in the vicinity of sharp edges a numerical singularity occurs [66]. However, the stress peak is significantly below the measured silicon strength of 2575 MPa [37]. Therefore, no failure of the silicon die is predicted.

Due to the concave warpage of the package after the copper removal (**H**) the stress peak of σ_1 of approx. 135 MPa is reached in the epoxy resin above the silicon die top edge, see Figure 54c. This is a consequence of the epoxy resin curing shrinkage with a contribution of bending of the epoxy resin layers and the prepreg #1037 over the die edge. The part of the package outside the silicon die has practically symmetrical structure, see Figure 42. This leads to its dissimilar warpage with the rest of the package and causes the bending. The epoxy resin strength, as reported in [23] is approx. 130 MPa. This means that the calculated value is slightly above the material's strength limit. The residual stress in the epoxy resin might be overestimated, since only a linear-elastic material model is employed. A study by Harper and Weitsman [69] shows that the viscoelastic relaxation of the epoxy matrix reduces the residual stresses by about 20%. The linear-elastic approach is justified by the assumption of a fast curing process, where an elastic effect is dominant as compared with a viscous effect [70].

By means of the embedding process simulation the in-plane stress σ_x [MPa] is evaluated through the package center and compared between steps **E**, **G** and **H**, see Table 16. The stress is assessed in the middle of the adhesive BLT (location Z_1), on the bottom of the silicon die (location Z_2), on the top of the silicon die (location Z_3) and in the middle of the epoxy resin layer above the silicon die (location Z_4), see Figure 55.

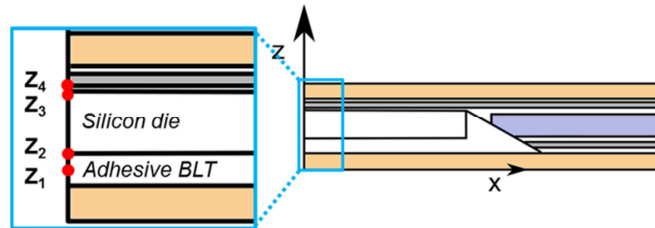


Figure 55: Schematic of locations for the in-plane stress evaluation [52].

After the copper removal in step **H** the residual stress in the adhesive (Z_1) decreases by around 25% compared to the level after the assembly step **E**. In any case, all values of the adhesive residual stress are under the measured adhesive strength of 105 MPa, see chapter 3.3. Therefore no adhesive failure is predicted.

Table 16: The in-plane stress σ_x [MPa] through the package center in steps **E**, **G** and **H** [52].

Location / Process step	In-plane stress σ_x [MPa]			
	Adhesive Z_1	Si die Z_2	Si die Z_3	Resin Z_4
E	85.8	-110.1	53.2	-
G	-7.3	-117.5	-134.1	46.2
H	64.0	-104.1	-179.4	113.1

In the assembly step **E**, the silicon die bottom (Z_2) is compressed due to the adhesive curing shrinkage which leads to the convex warpage of the package. The free die top (Z_3) is under tension. When the die is embedded (step **G**), the die top (Z_3) is under compression due to the epoxy resin curing shrinkage. The compressive stresses on the silicon die top (Z_3) increases after the copper removal, when the package warps in the concave direction. In step **H** the resin's curing shrinkage that is held by contact with the top copper foil is released and the package warps concavely. However the resin curing shrinkage, which is suppressed by contact with the silicon die, is not released and, due to the package bending, the residual stress in the epoxy resin (Z_4) increases. It should be noted that in step **G** the package is still in the lamination press.

The maximum principal stress σ_I arising in the silicon die after the copper removal step **H** is on the die edge at the interface with the adhesive meniscus; see Figure 54c. It reaches approx. 124 MPa. The stress peak is significantly lower than the measured silicon strength of 2575 MPa [37]. No failure is therefore predicted in the silicon die before the package is further treated by the copper via manufacturing and the solder mask printing process.

4.5. Summary and conclusions

The embedding process is analyzed with a special focus on the lamination in terms of package warpage and residual stresses. The analytical lamination theory of woven structures is employed for determination of the prepreg's orthotropic properties. The impact of the process history is taken into account by applying an elasto-plastic material behavior for the copper and the adhesive. The stepwise solution approach used in the analysis is validated experimentally by the Rocking-Curve-measurement of the package warpage. Very good agreement is achieved between the numerical and the experimental results. After the assembly process the curvature difference amounts to less than 9%. After the lamination followed by the copper removal the difference is less than 3%.

Since the stresses arising in the package may reach the material's strength and therefore cause damage, the stress maxima are investigated. It is shown that:

- The maximum calculated stresses in the silicon die are clearly below the measured characteristic strength of the dies. Therefore, no die failure is predicted.
- The stresses calculated in the adhesive decrease by around 25% from the level after the assembly process due to the lamination and the copper removal. They are lower than the measured adhesive strength. Adhesive failure is not expected.
- The stresses calculated in the epoxy resin layer are slightly higher than typical values for the epoxy resin strength. This might be caused by the assumption of a linear-elastic material model employed in the analysis. In this case, failure of the epoxy in form of delamination might occur.
- If the viscoelastic nature of polymer parts (adhesive, epoxy resin) were taken into account, it could lead to a relaxation of residual stresses by about 20%. The assumption of a fast curing process justifies a linear-elastic approach because under such conditions an elastic effect is dominant as compared with a viscous effect.

5. Reliability study of a PCB board with vias

In order to create a functional PCB, the silicon die has to be connected with a circuit. This is reached by manufacturing of copper vias and traces, which link copper pads on the silicon die with an electrical source [1], see Figure 56. During its operation in electronic devices a PCB board is exposed to a cyclic thermal loading. This may in a critical case lead to via cracking and creation of opened circuits.

The motivation of the study is to determine copper via reliability under thermal cycling. For that purpose a reflow cycling is chosen. The PCB board is ten times loaded by a temperature range from RT to 260°C. A temperature profile of the reflow process is shown in Figure 57.

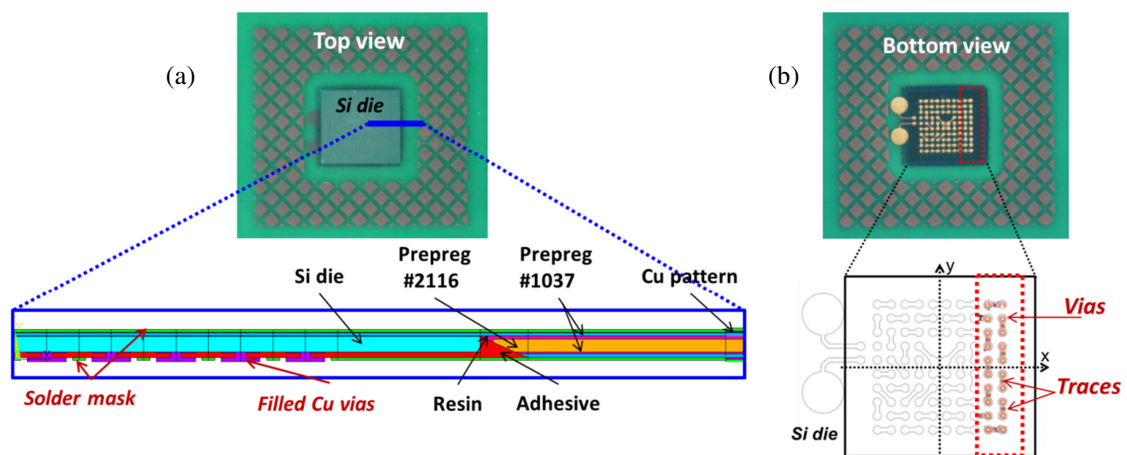


Figure 56: The investigated package with configurations of copper vias and traces: (a) Package top view with a cross section, (b) Package bottom view with a detail of the vias and the traces.

The investigated package has the same configuration (the silicon die, the adhesive, the copper pattern, the prepregs #1037 and #2116 and the resin layers) as the one after the copper removal, see chapter 4. In addition, copper vias are presented in the package going through the adhesive in positions illustrated in Figure 56.

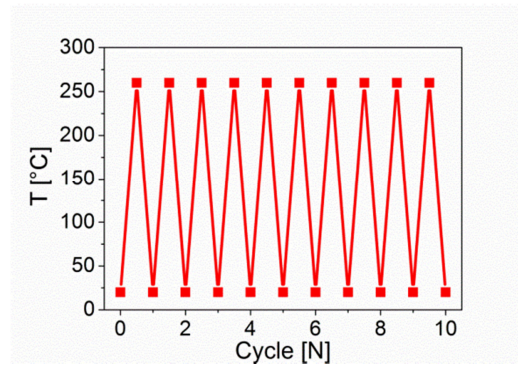


Figure 57: Reflow cycling temperature profile.

The cylindrical-shaped vias are drilled by laser. The drilled holes with a wall angle α_w of 90° are fully filled with copper using an electrodeposition process. The diameter of a via is $80\ \mu\text{m}$ and the distance between two adjacent vias is $500\ \mu\text{m}$. A via top land, *i.e.* a die copper pad, and a via bottom land have the diameter of $300\ \mu\text{m}$. The thicknesses of via bottom land and top land are approx. $32\ \mu\text{m}$ and $8\ \mu\text{m}$, respectively. The sharp radius transition between via lands and via is in the model approximated by a fillet radius of $2\ \mu\text{m}$. The nominal via geometry is described in detail in Figure 58.

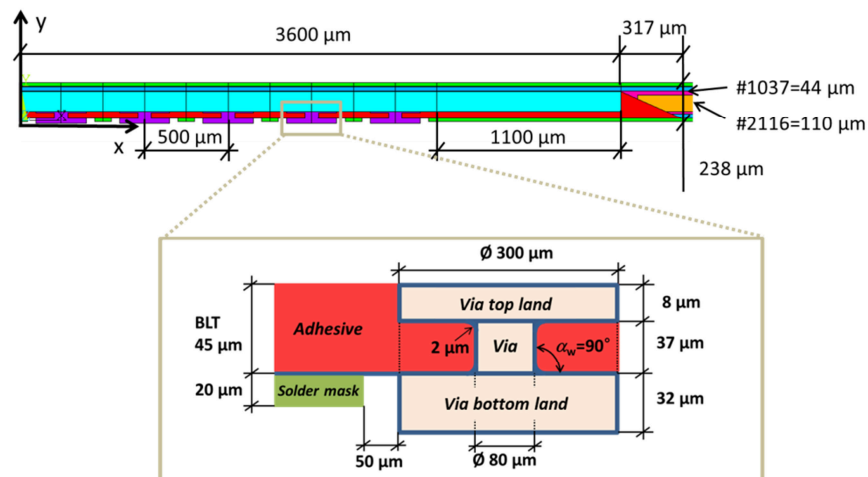


Figure 58: Copper via geometry.

A layer of solder mask is printed on a PCB board to protect areas free of vias and traces from contaminants [1, 3]. Besides, it helps to prevent unwanted short circuits on PCBs. The solder mask consists of a polymer. It is marked by deep green color in

Figure 56. The solder mask layer has a thickness of approx. 20 μm and it is 50 μm apart from via bottom land, see Figure 58.

The solder mask is printed in a liquid state and consequently it requires curing at elevated temperatures. As a result it influences the residual stresses in the package after the die embedding. Since the solder mask curing profile and a volumetric shrinkage are unknown, the package is assumed to be initially stress-free, *i.e.* no residual stresses and the package warpage due to the process flow are included in the analysis. Regarding the complexity of the package structure, the reflow process is modelled only numerically using the finite element software Ansys[®] [47].

The important issue of the package reliability is the survival of the copper vias. In the following investigation the focus is set on a thermo-mechanical loading of the vias in the package during the reflow cycling. The stress and strain distribution is analyzed in the package and the via lifetime is determined.

5.1. Fatigue life assessment of copper vias

Reliability of copper vias is a case of a high strain/low-cycle fatigue, *i.e.* a lifetime of approx. $10^3 - 10^4$ cycles. Fatigue of copper is characterized by elastic and plastic strain components. The overall fatigue life of a via structure is calculated as the number of total cycles to failure N_f using Miner's rule of mixture [83] and the number of cycles to failure due to accumulated elastic and plastic strains, N_{fe} and N_{fp} , respectively, as follows:

$$\frac{1}{N_f} = \frac{1}{N_{fe}} + \frac{1}{N_{fp}}. \quad (70)$$

During a high-strain/low-cycle testing the dominant component is the plastic deformation. Elastic deformation plays a role mainly during low-strain/high-cycle testing; therefore the region of elastic deformation is also considered as the dynamic region. In that case, the first term on the right hand side of Eq. (70) dominates and fatigue performance is mainly a function of the tensile strength. Conversely, in the high-strain/low-cycle regime, the second term of Eq. (70) dominates and fatigue is a function of ductility [84]. Judging lifetime based on stresses is not useful in the case of

low-cycle fatigue. N_{fe} does not play a significant role. The fatigue life of via therefore simplifies to:

$$N_{fp} \ll N_{fe} \Rightarrow N_f \cong N_{fp}. \quad (71)$$

In this study the via reliability is predicted with approaches by Coffin-Manson [84, 85] and Engelmaier [86, 87] which are described below, see Figure 59.

Coffin – Manson approach

One of the basic premises in the strain life approach is the correlation of strain range $\Delta\varepsilon$ and the number of load reversals to failure, $2N_{fe}$ and $2N_{fp}$. This relation is defined with the Coffin-Manson's equation [84, 85]:

$$\Delta\varepsilon = \Delta\varepsilon_e + \Delta\varepsilon_p, \quad (72)$$

$$\Delta\varepsilon_e = 2 \frac{\sigma_f}{E} (2N_{fe})^b, \quad (73)$$

$$\Delta\varepsilon_p = 2\varepsilon_f (2N_{fp})^c, \quad (74)$$

where c is the fatigue ductility exponent, ε_f and σ_f are the ductility and the strength at tensile fracture of copper and E is the Young's modulus.

Engelmaier approach

The general expression by Coffin-Manson, Eq. (72), is enhanced by Engelmaier's work [87] focused on electronic packaging and interconnection technology as follows:

$$\Delta\varepsilon_e = 0.9 \frac{\sigma_f}{E} \left[\frac{e^{\varepsilon_f}}{0.36} \right]^{0.1785 \log(10^5 / N_{fe})}, \quad (75)$$

$$\Delta\varepsilon_p = \varepsilon_f^{0.75} N_{fp}^c. \quad (76)$$

For most metals the value of the fatigue ductility exponent c lies between - 0.5 and - 0.7. In this investigation $c = -0.6$ is chosen as a representative value. Different sources

report that the ductility of electro-deposited copper is smaller than the ductility of the bulk copper [88, 89, 84]. Thus here a maximal ductility ε_f of 20% is assumed.

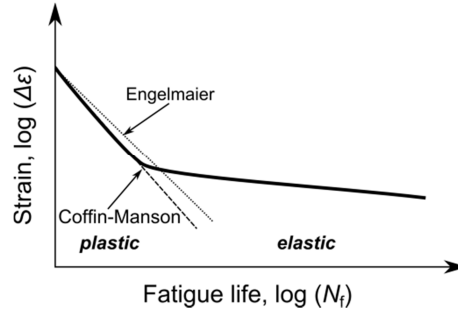


Figure 59: Strain-fatigue life curve [83].

For the purpose of the via lifetime analysis a plastic strain range (increment) $\Delta\varepsilon_p$ is used as damage metric of via failure, as illustrated in Figure 60. Based on Eq. (74) and (76) the number of cycles to failure due to accumulated plastic strains N_{fp} , is calculated. A von Mises strain increment within one cycle is utilized for the evaluation, since there is currently no consensus on how normal and shear strain components contribute to the via failure. The von Mises component combines both parts [90, 91].

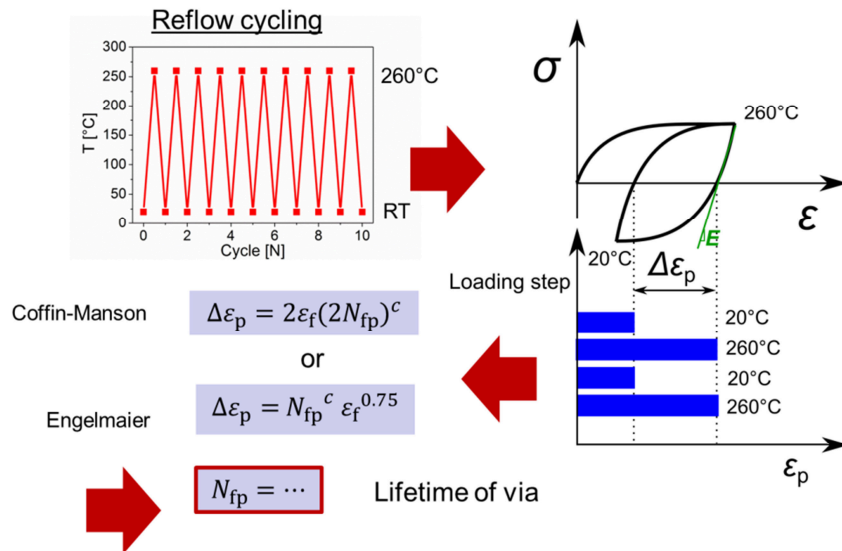


Figure 60: Schematic of fatigue life assessment of copper vias during the reflow cycling.

5.2. Numerical model

Only a single die package extracted from the production panel is investigated. The package containing vias and traces is very complex, see Figure 56. Vias interconnected by traces create an irregular structure. In order to decrease the calculation time the package is simplified to a 2D model and constrained by symmetric and periodic boundary conditions, see Figure 61.

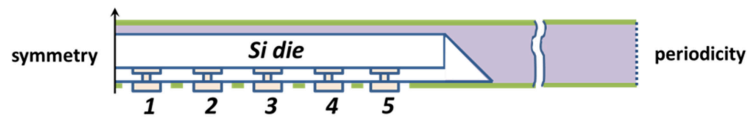


Figure 61: Boundary conditions of the numerical model.

The most common via interconnects by traces are identified and the package is represented by their sections (S1 - S4) which are numerically modelled, see Figure 62. Interconnects are classified by the number of coupled vias (henceforth called via pattern) as follows: (i) free vias (no vias coupled), (ii) 2 vias coupled, (iii) 4 vias coupled. Each particular via in a pattern is numbered from 1 to 5 according to its position from the package center to the edge.

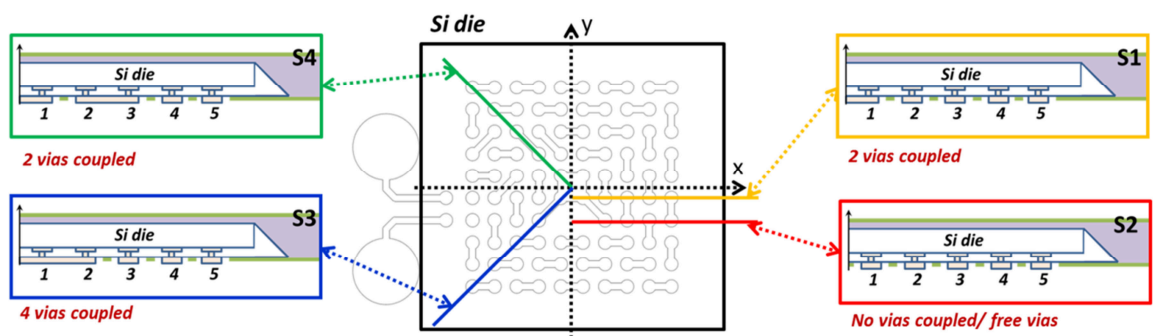


Figure 62: The package representation by sections (S1 - S4) of the most common via interconnects.

The package structure remaining after the lamination and the copper removal process is modelled with approaches described in chapter 4. The 2D model is discretized by

quadratic elements of type “plane183” with a generalized plane strain option. The part of the package containing the copper vias (part I) has a fine mesh of $3\mu\text{m}$ element size, the part of the package placed between the via and the copper pattern (part II) has a coarser mesh of $8\mu\text{m}$ element size, the rest of the package (part III) has a mesh of $10\mu\text{m}$ element size, see Figure 63. The element size has been determined as sufficient after thorough convergence studies. The connectivity of dissimilar meshes is achieved by employing multi-point-constrained (MPC) fully fixed contact. All components of the package are perfectly bonded together by means of nodes sharing the interface.

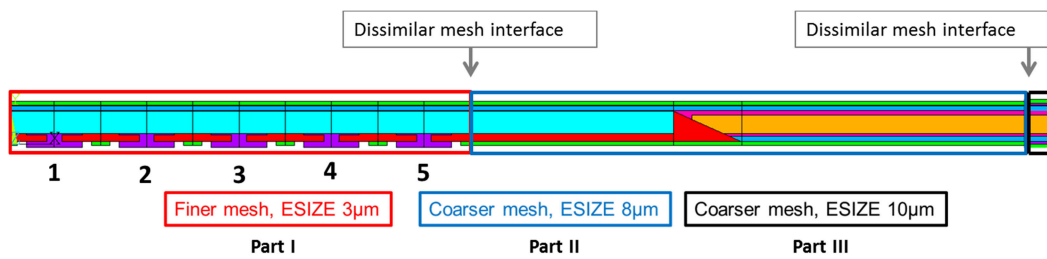


Figure 63: Numerical model of the package.

Residual stresses and the package warpage caused by previous manufacturing steps are not included in the numerical model. The package is therefore modelled as initially stress-free. The reference temperature $T_{\text{ref, re}}$ is set to RT. The reflow cycling is performed by a uniform isothermal loading on the entire structure according to Figure 57.

5.3. Material properties

In the case of the reflow cycling, the package consists of up to 7 materials, *i.e.* the electro-deposited copper, the adhesive, the silicon, the solder mask, the resin and composites of resin and E-glass represented by the prepregs of type #1037 and #2116. In order to analyze the thermo-mechanical response of the package during the reflow, it is necessary to determine temperature dependent key properties of the involved materials.

Fatigue of copper vias is determined by the elasto-plastic material behavior of the electro-deposited copper. The silicon, the adhesive and the E-glass are modelled as

linear elastic with material properties equal to those published in chapter 3 and 4. An additional measurement of the resin's coefficient of thermal expansion (CTE) is provided, since the resin changed its thermal extensibility after its full curing in the lamination process. As a result the elastic constants and CTEs of the prepregs #1037 and #2116 are determined using the lamination theory of woven structures (chapter 4.1.1) and implemented into the numerical model.

Properties of electro-deposited copper

Since the lifetime of a via is of interest, accurate copper material properties are imperative. The electro-deposited copper is less stiff than a bulk copper. This is caused by higher amount of vacancies in the copper, which comes from an electrodeposition process [88]. Stress-strain diagrams based on data measured by IBM electronic (Endicott, NY) [89, 84] are used in the analysis. The stress-strain behavior is modelled with a smoother elastic-plastic transition applying a power law of the form of Eq. (80) as published in [84],

$$\sigma_y = \sigma_{y0}(T) \left(1 + \frac{\epsilon^p}{\epsilon_0^p(T)} \right)^{1/n_h} \quad (77)$$

The function accounts for the temperature dependency of plasticity, where $\sigma_{y0}(T)$ is the initial yield stress and $\epsilon_0^p(T)$ is the reference plastic strain. The hardening exponent is assumed constant with $n_h = 25$. The reference plastic strains are summarized in Table 17.

The copper plasticity data are implemented into the numerical model using a bilinear-kinematic hardening model [47], see Figure 64.

Table 17: Stress-strain data of electro-deposited copper as a function of temperature [89, 84].

T [°C]	E [MPa]	ν [-]	σ_{y0} [MPa]	ϵ_0^p
-65	45086	0.34	156	3.46e-3
20	43823	0.34	149	3.40e-3
120	43994	0.34	146	3.33e-3
200	39285	0.34	121	3.08e-3
300	31028	0.34	87.5	2.82e-3

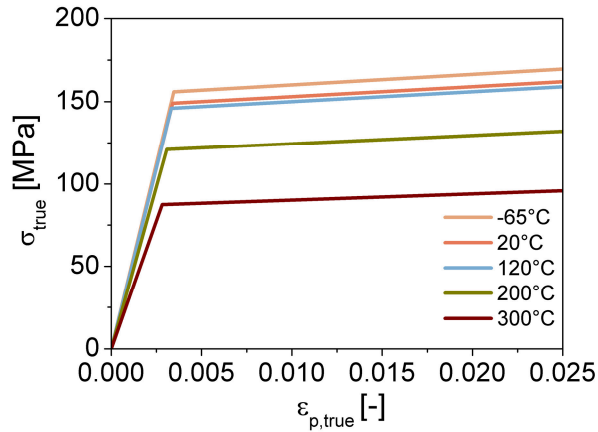


Figure 64: Bilinear-kinematic hardening model of the electro-deposited copper.

Cured epoxy resin properties

The resin's Young's modulus E as a function of temperature is reported in chapter 4, if $E = 4.3$ GPa at RT. The development of CTE of fully cured resin as a function of temperature is measured using thermo-mechanical analysis (TMA). The resin specimens with an initial length of approx. 0.7 mm are axially loaded by a small constant force of 0.1 N. The glass transition temperature T_g is observed around approx. 150°C. The development of the CTE is plotted in Figure 65.

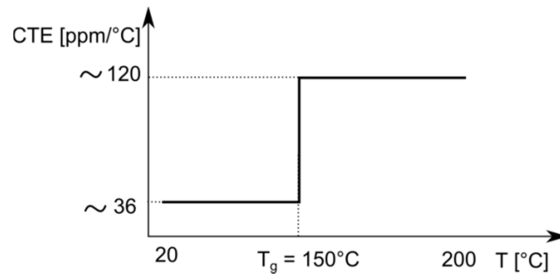


Figure 65: Idealized graph of fully cured resin coefficient of thermal expansion (CTE) as a function of temperature. The glass transition temperature T_g is approx. 150°C.

Prepreg orthotropic properties

Prepreg thermo-elastic properties are determined based on the lamination theory of woven structures, as described in detail in chapter 4.1.1. Based on the knowledge of linear elastic properties of the epoxy resin matrix, the E-glass fibers and the prepreg strand geometry, the orthotropic properties of a prepreg of type #1037 and #2116 are

determined, see Table 18 and Table 19. The prepreg homogenization is done only in a region of a prepreg glass cloth, as mentioned in chapter 4.2. The prepreg's orthotropic properties are temperature dependent.

Table 18: Homogenized orthotropic properties of prepreg #1037 with fully cured resin at 260°C.

Young's modulus	[GPa]	Shear modulus	[GPa]	Poisson's ratio	[-]	Effective CTE	[ppm/°C]
E_x	9.9	G_{xy}	60.2e-3	ν_{xy}	0.0129	α_x	6.9
E_y	6.9	G_{xz}	58.7e-3	ν_{xz}	0.0251	α_y	12.9
E_z	5.4	G_{yz}	58.7e-3	ν_{yz}	0.0251	α_z	43.6

Table 19: Homogenized orthotropic properties of prepreg #2116 with fully cured resin at 260°C.

Young's modulus	[GPa]	Shear modulus	[GPa]	Poisson's ratio	[-]	Effective CTE	[ppm/°C]
E_x	2.9	G_{xy}	79.1e-3	ν_{xy}	0.0442	α_x	10.0
E_y	3.2	G_{xz}	77.1e-3	ν_{xz}	0.0863	α_y	9.3
E_z	2.0	G_{yz}	77.1e-3	ν_{yz}	0.0863	α_z	37.9

Solder mask

The linear elastic material properties of the solder mask at RT are taken from literature [92]. The glass transition temperature T_g is approx. 100°C. The temperature dependency of the Young's modulus and the Poisson's ratio is estimated according to the temperature behavior of the adhesive. The Poisson's ratio ν is assumed as 0.29 below T_g and 0.45 above T_g .

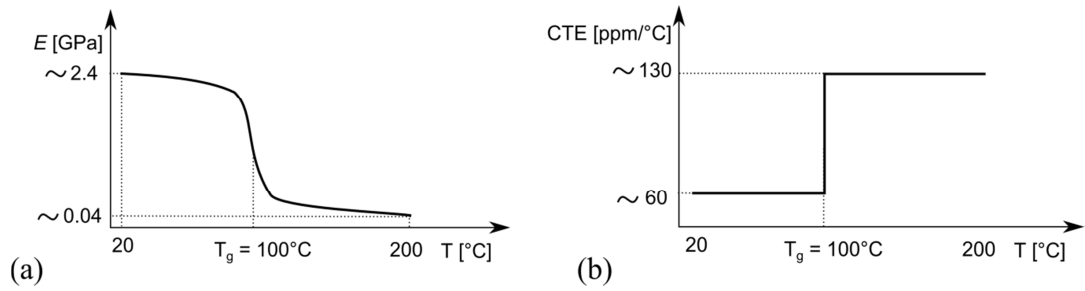


Figure 66: Idealized graphs of thermo-elastic properties of a fully cured solder mask: (a) Young's modulus E as a function of temperature, (b) Coefficient of thermal expansion (CTE) as a function of temperature. The glass transition temperature T_g is approx. 100°C .

5.4. Results and discussion

The failure usually begins at the diameter transition, due to an increase in the tensile stress in this location. Four critical locations are defined on each via at the diameter transitions, marked P1 to P4, see Figure 67. Since two critical locations P1 - P2 and P3 - P4 are defined at the same transition, an influence of a distance from the package center on stress-strain state in those locations is taken into account.

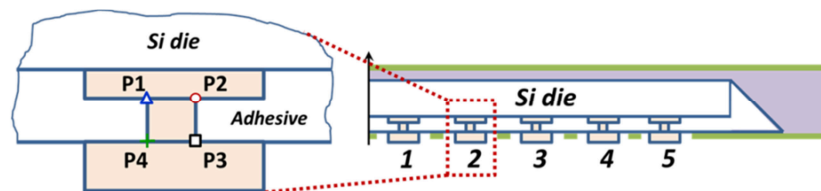


Figure 67: Critical locations P1 - P4 at a diameter transition in each via 1 - 5.

The aim of the reliability investigation is twofold: (I) Stress-strain evaluation. (II) Lifetime assessment.

The goal of the stress-strain investigation is following: (i) To identify, which via position from 1 to 5 is critical, *i.e.* in which via failure occurs first. (ii) To investigate the influence of via interconnection, *i.e.* how traces change the stress-strain state in vias. (iii) To define the most loaded/critical location on the via from P1 to P4.

The stress-strain investigation identifies “the critical via” in terms of position and location. In the lifetime assessment the number of cycles to failure is determined for “the critical via”.

In order to illustrate the overall stress state in the package the maximum principal stress σ_1 is shown in Figure 68. The results are plotted for the 10th cycle (a) at 260 °C, (b) at RT. A detailed evaluation is performed for the via in position 5. The deformations are exaggerated by a scaling factor of 10.

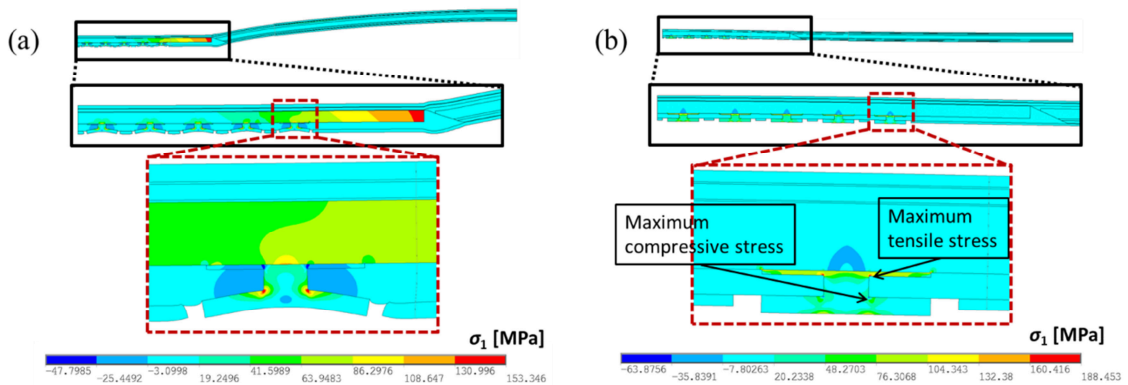


Figure 68: Distribution of the maximal principal stress σ_1 [MPa] in the package in 10th cycle (a) at 260 °C, (b) at RT. The detail is plotted for the via in position 5.

At 260°C the high thermal expansion of the adhesive leads to a convex shape of the via bottom land, see Figure 68a. This causes a concentration of the maximum tensile stresses at location P3 and P4 (bottom) and the maximum compression stresses in locations P1 and P2 (top) at that moment. The package over the silicon die warps in a concave manner with a curvature radius R of 2603 mm. After cooling the package down to RT, the high adhesive shrinkage tends to shear off the via in a horizontal direction, *i.e.* sideways. As a result the location of tension/compression is exchanged, see Figure 68b. The maximum tensile stress occurs in the via top radius transition (here in the location P2) and the maximum compressive stress in the via bottom radius transition (here at location P3), see Figure 68. The package over the silicon dies changes the warpage to a convex shape with a curvature radius R of 1226 mm.

5.4.1. Stress-strain investigation in the copper via patterns

Based on a numerical simulation of 10 reflow cycles of via patterns S1 - S4, the stress and strain level is evaluated at RT in each via position from 1 to 5 and locations from P1 to P4. The evaluation is provided in an area of a radius $R_e = 10 \mu\text{m}$, see Figure 69. The maxima of the principal stress σ_1 (+ / -) and the accumulated equivalent plastic strain $\varepsilon_p^{\text{eq}}$ are assessed as reference values for the stress-strain investigation.

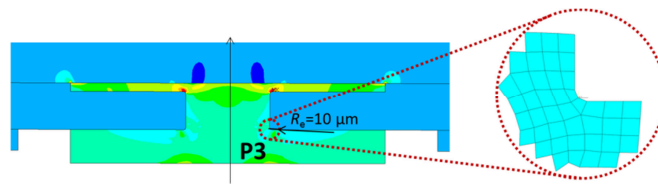


Figure 69: Area for the stress-strain evaluation illustrated in the critical location P3.

The maximum principal stress σ_1 is chosen, since it gives information about the overall stress state in the via in terms of tension/compression. Besides, the accumulated equivalent plastic strain $\varepsilon_p^{\text{eq}}$ gives information about a plastic strain increment per load cycle, which is the driving mechanism of the low-cycle failure. It is assumed that in the location of the highest accumulated plastic strain there is the highest strain increment over a cycle, *i.e.* it is the most loaded location in the via.

Free vias in the pattern S2

Figure 70 shows that there is no significant difference in the stress-strain state over via 1 - 5 in the free via package. This is caused by the thermo-mechanical origin of the package warpage due to the material's CTE mismatch. The residual stress in the adhesive remains practically constant over the via position 1 - 5 (along the silicon die) as it has already been observed in Figure 35 (chapter 3.4.2).

The package bending is not caused by any external force. Since the vias are not interconnected, they deform independently from each other. The plane of symmetry of the free vias pattern lies in the middle of each single via, which is demonstrated by the identical stress-strain level in $P1 = P2 \approx 180 \text{ MPa}$ (top) and $P3 = P4 \approx -60 \text{ MPa}$

(bottom), see Figure 71 . The maximum accumulated equivalent plastic strain ε_p^{eq} of approx. 0.55 [-] is found in the bottom fillet radius, *i.e.* in the locations P3 = P4.

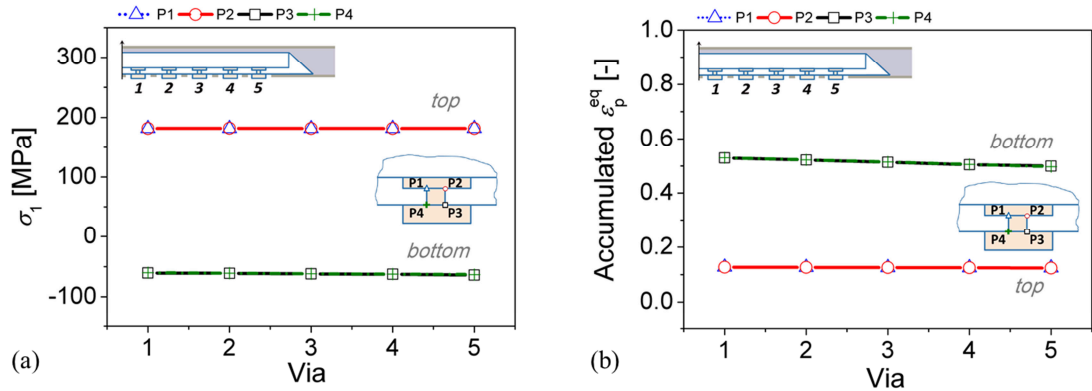


Figure 70: (a) Distribution of the maximum principal stress σ_1 [MPa] over via positions 1 - 5 and locations P1 - P4. (b) Distribution of the accumulated equivalent plastic strain ε_p^{eq} [-] over via positions 1 - 5 and locations P1 - P4.

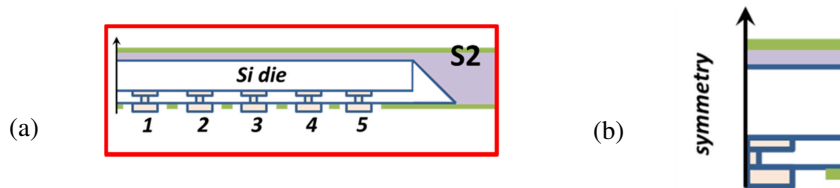


Figure 71: (a) Schematic of the free vias pattern, (b) Symmetry of the free via pattern.

One can conclude that in the free vias pattern: (i) each via exhibits practically the same symmetrical stress-strain state, (ii) the most locations susceptible to via failure are identified in P3 = P4 in the via bottom radius transition.

Two vias coupled in the patterns S1 and S4

As an analogy to the free via pattern no significant difference in the stress-strain results is observed over free vias in positions 2 - 5 (pattern S1) and positions 4 - 5 (pattern S4) respectively. Two coupled vias in position 1 (pattern S1) reach the same stress-strain level as the ones in positions 1 - 3 (pattern S4), see Figure 72 and Figure 73.

The coupled vias exhibit in their outermost positions, *e.g.* via 1 and 3 (pattern S4), a higher level of stresses (about 30 % on the via top and 5 % on the via bottom) and strains (about 300% on the via top and 40% on the via bottom) than the free vias. This is caused by their additional constraint due to trace interconnects to the via bottom lands, which encapsulate the thermally expanding adhesive. The traces in turn increase the stiffness of the via bottom land.

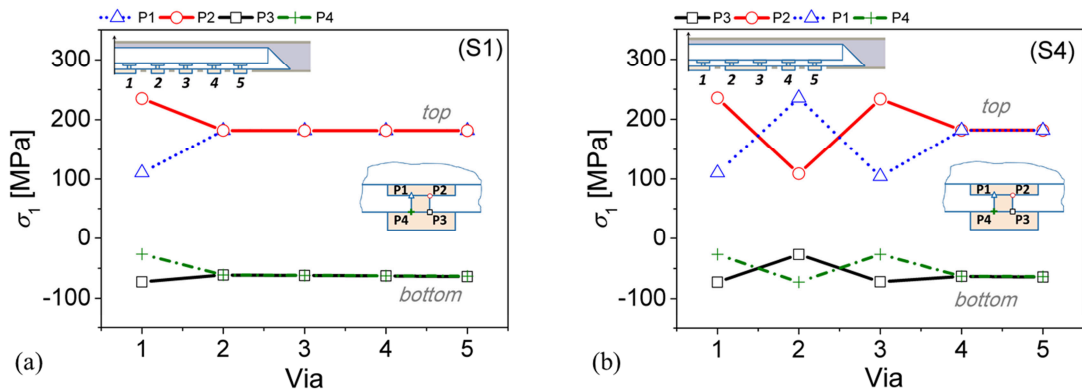


Figure 72: Distribution of the maximum principal stress σ_1 [MPa] over via positions 1 - 5 and locations P1 - P4 in (a) the via pattern S1, (b) the via pattern S4.

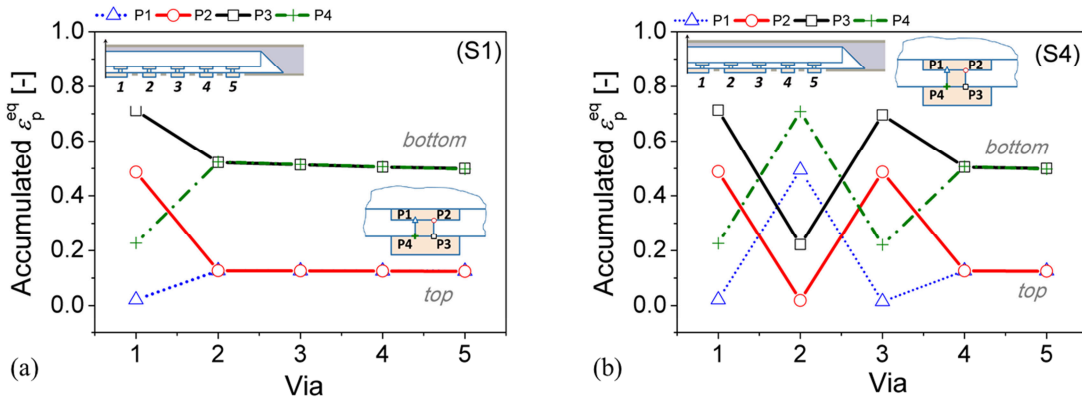


Figure 73: Distribution of the accumulated equivalent plastic strain ϵ_p^{eq} [-] over via positions 1 - 5 and locations P1 - P4 in (a) the via pattern S1, (b) the via pattern S4.

For vias in position 1 (pattern S1) and positions 1 - 3 (pattern S4) it is shown that two coupled vias have a plane of symmetry between the vias. The stress-strain level is therefore equal in locations P1 (right) = P2 (left) and P3, P4 analogously, see Figure 74.

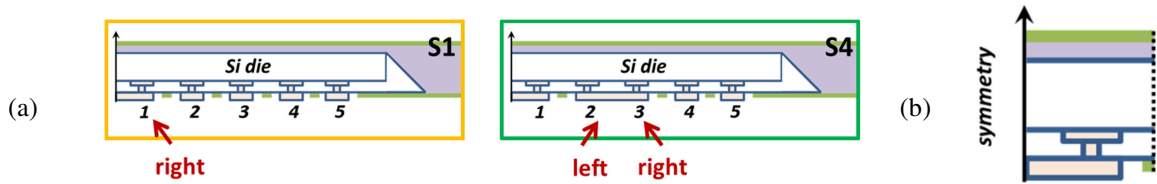


Figure 74: (a) Schematic of two coupled vias patterns S1 and S4, (b) Symmetry of a two coupled vias pattern.

The locations most susceptible to via failure are identified as the outermost locations of P3 and P4 on the bottom fillet radius due to the influence of the trace interconnect. As a result of a high thermal expansion of the adhesive two coupled vias are pushed apart and pulled together during a thermal cycling. Consequently they bend around P3 and P4, where thus the highest degree of plasticization occurs.

Four vias coupled in pattern S3

In the case of 4 coupled vias the pattern S3 is compared with an idealized pattern X of all vias coupled, see Figure 75. It should be noted that the pattern X does not exist in the investigated package. To clarify that free vias in pattern S3 behave the same as those in the pattern S2, an additional comparative study is proposed.

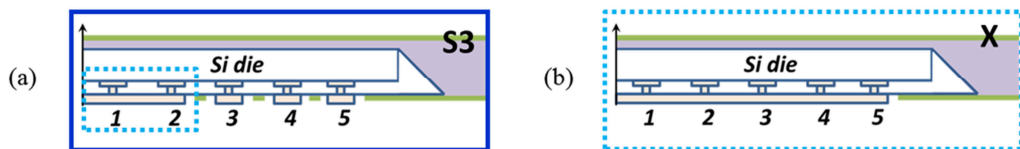


Figure 75: (a) Schematic of the 4 vias coupled pattern S3 in comparison to (b) an idealized pattern X where all vias are coupled.

An analogy to the previous analysis, the maximum stress-strain level at the outermost position of four coupled vias, *i.e.* via 2 (pattern S3), reaches the value obtained in the external position of all coupled vias, *i.e.* via 5 (pattern X), see Figure 76a and Figure 77. Free vias in pattern S3 are not influenced by the coupled vias, since they have the identical stress-strain state as the ones in the pattern S2. In addition it is shown that there is no difference between two, four or more coupled vias in terms of stresses and strains in the coupled via at its outermost position.

The location most susceptible to via failure is identified in the outermost location P3, where the accumulated plastic strain ε_p^{eq} amounts to approx. 0.7 [-], see Figure 77b and Figure 78.

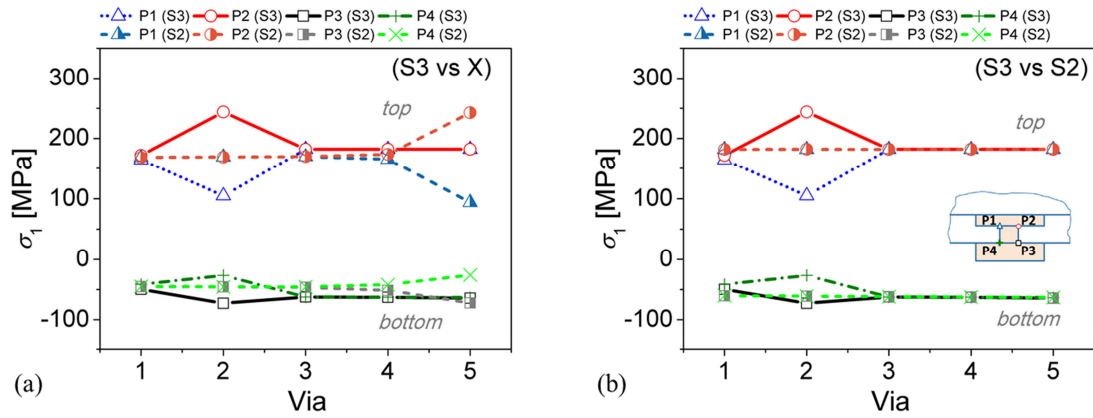


Figure 76: Distribution of the maximum principal stress σ_1 [MPa] over via position 1 - 5 and locations P1 - P4 (a) in the via patterns S3 vs X and (b) in the via patterns S3 vs S2.

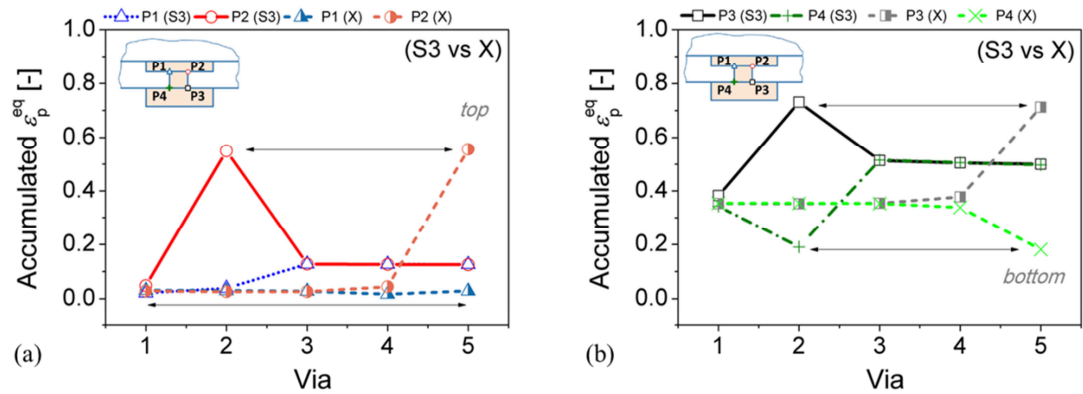


Figure 77: Distribution of the accumulated equivalent plastic strain ε_p^{eq} [-] over via position 1 - 5 in (a) the via patterns S3 vs X in locations P1 - P2 and (b) the via patterns S3 vs X in locations P3 - P4.

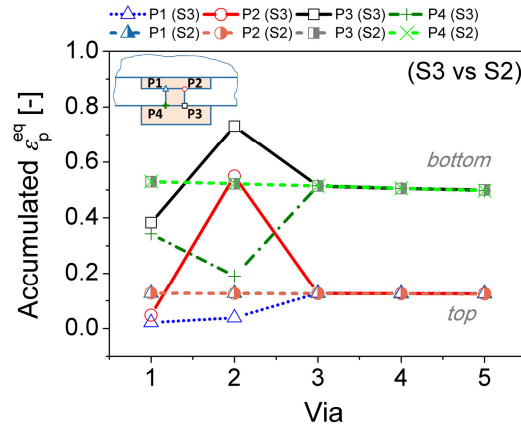


Figure 78: Distribution of the accumulated equivalent plastic strain ε_p^{eq} [-] over via position 1 - 5 and location P1 - P4 in the via patterns S3 vs S2.

It is concluded that there is no significant difference in the stress-strain level over via position in the coupled patterns except at its outermost position, there the critical location for the via failure is identified, *i.e.* location P3. The number of vias interconnected by traces does not play a role.

5.4.1.1. Application of the representative cell model

Due to the observed symmetrical stress-strain distribution in via patterns, there is a possibility to a representative cell model for fatigue life assessment of the copper vias.

In that case the free via pattern is substituted by an infinite laminate with uniformly distributed single vias. This corresponds to a single via reference model (further called 1ViaRef), which is constrained with symmetric and periodic boundary conditions, see Figure 79a. The two coupled via pattern is substituted by an infinite laminate with uniformly distributed coupled vias. In this regard the two vias reference model (further called 2ViasRef) is defined with the boundary conditions mentioned above, see Figure 79b.

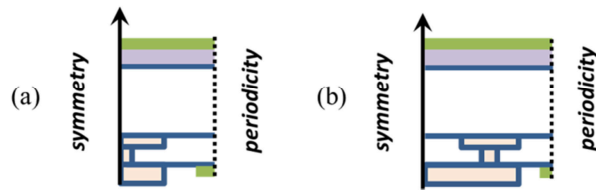


Figure 79: The package superposition by (a) the single reference via model (1ViaRef) and (b) two vias reference model (2ViasRef).

To prove that the representative cell model is applicable for the description of the thermal fatigue behavior of the package, the comparison of the maximum principal stress σ_1 and the accumulated equivalent plastic strain ε_p^{eq} is provided for the via in position 1. The stress-strain results of the patterns S2, S1 are compared with the reference via models 1ViaRef, 2ViasRef over 10 reflow cycles. In the analysis of the 1ViaRef model the stress-strain results are plotted only for locations P2 and P3, since the results are equal at P1 = P2 (top) and P3 = P4 (bottom). In the study of the 2ViasRef model the stress-strain results are plotted for all locations P1 - P4.

Figure 80 shows that the stress-strain results of the 1ViaRef model are in very good agreement with the results of the pattern S2. Only a small deviation of less than 1% is observed between the results.

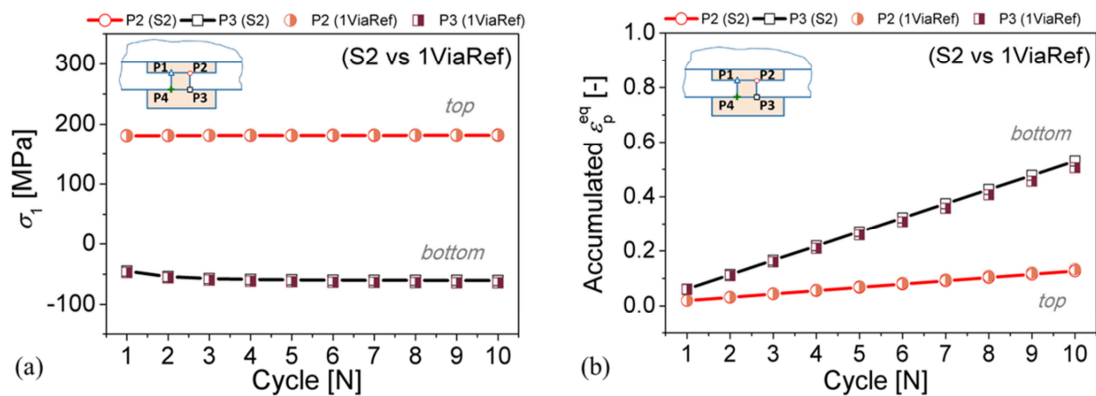


Figure 80: Comparison of the results of the via pattern S2 and the 1ViaRef model: (a) The maximum principal stress σ_1 [MPa] over 10 reflow cycles at location P3 and P4, (b) The accumulated equivalent plastic strain ε_p^{eq} [-] over 10 reflow cycles at location P3 and P4.

Also, a good agreement of the stress results between the 2ViasRef model and the pattern S1 is reached, see Figure 81. The maximum deviation of the strain results accounts of less than 30 % only at location P2. Nevertheless, the strain development in the 2ViasRef model over cycles shows the same trend as the results of the pattern S1. The highest accumulated equivalent plastic strain ε_p^{eq} is found in the location P3, which is in agreement with the previous conclusions of the stress-strain investigation of the pattern models.

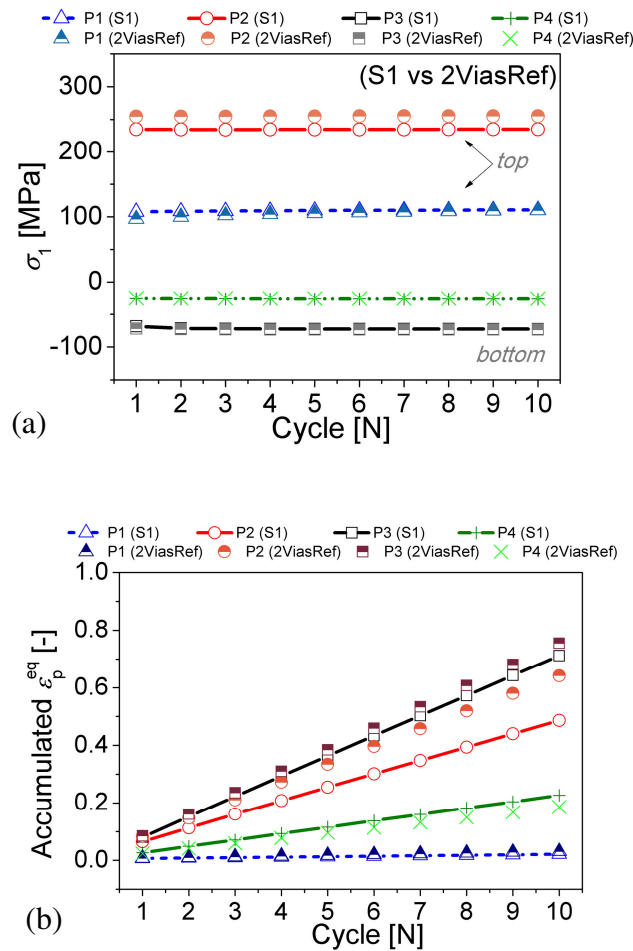


Figure 81: Comparison of the results of the via pattern S1 and the 2ViasRef model: (a) The maximum principal stress σ_1 [MPa] over 10 reflow cycles at locations P1 - P4, (b) The accumulated equivalent plastic strain ε_p^{eq} [-] over 10 reflow cycles at locations P1 - P4.

Based on the graphs plotted above (Figure 80 and Figure 81) it is confirmed that the representative cell model is suitable for the description of the stress-strain state in the package including vias. As a result the reference models are used for a parametric study.

5.4.2. Lifetime assessment of copper vias

For the purpose of via fatigue life assessment, the equivalent plastic strain increment $\Delta\epsilon_p$ within one cycle is evaluated as the strain average over integration points of elements in an area of radius $R_e=1 \mu\text{m}$ at the critical location P3. A von Mises strain increment within one cycle is used in the analysis. A stabilization of the strain increments is observed after the 3rd loading cycle. The stabilized increment is used for the fatigue life assessment.

The location P3 is determined as the most critical point of the structure, since it exhibits the highest accumulated equivalent plastic strain in its outermost location (the 2ViasRef model and the via patterns S1 and S2) as it is concluded above. Using Eq. (74) and (76), *i.e.* the Coffin-Manson and Engelmaier approach, respectively, the number of cycles to failure are calculated and summarized in Table 20.

Table 20: Reliability of copper vias during the reflow cycling evaluated for the critical location P3 in the via.

Plastic strain range $\Delta\epsilon_p$ [-]	Number of cycles to failure [N]	
	Coffin-Manson	Engelmaier
0.0183	~ 85	~ 105

The reflow cycling represents an extreme testing condition, where the temperature difference amounts to 240°C. As a results the via lifetime is determined at around 85 cycles. Due to a small difference in the analytical approaches the Engelmaier formula predicts a 24 % higher via lifetime than Coffin-Manson.

5.5. Summary and conclusions

PCB boards are exposed to a cycling thermal loading during their operation in electronic devices. This may in a critical case cause via cracking and a creation of opened circuits. In this regard a PCB including vias is investigated during the reflow cycling (RT – 260 °C). A 2D numerical model of the package is used taking into account via interconnects by traces. The behavior of the electro-deposited copper is described by an elasto-plastic material model. Analytical Coffin-Manson and Engelmaier approaches are employed for evaluation of the via reliability. The via lifetime is analyzed in terms of the plastic strain increment per load cycle, which is the driving mechanism for low-cycle fatigue.

At the beginning of the analysis the stress-strain state in the vias after the reflow is unknown. Therefore the overall package investigation identifies “the critical via” in terms of position and location. It is shown that:

- There is no significant difference in stress-strain results of via 1 and 5 in the nominal package, since residual stresses in the adhesive remains practically constant across the different via positions.
- Vias coupled by traces are severely loaded configurations. If more than 2 vias are coupled, the outermost via is exposed to the highest loading. Due to a high thermal expansion of the adhesive 2 coupled vias bend around locations P3 and P4, where consequently the highest plasticization occurs.
- For any via pattern having a via wall angle α_w of 90° it is valid that during the reflow cycling the highest plastic straining is located at the outermost location P3, *i.e.* at the fillet radius between the via bottom land and the via. This is the most critical point of the structure, where failure will occur first.
- It is proven that the representative cell model is capable to describe the stress-strain state in via patterns.

The number of cycles to via failure is analyzed at the most critical point of the structure, P3, where the maximum plastic strain arises. Based on Coffin-Manson and Engelmaier approaches the number of cycles to via failure is determined as $N_f = 85$ and $N_f = 105$, respectively, for reflow cycling conditions.

6. Parametric study and design rules for the embedding process

The die embedding is a very complex process containing different manufacturing steps, as described in the previous chapters 2 - 5. The ongoing trend of electronic devices miniaturization and increase of their functionality emphasizes on improvement of the embedding process up to its limitations. The process limitations are defined by *e.g.* the material's strength, the critical package warpage influencing further package workability in subsequent process steps, etc.

In order to improve the embedding process in terms of the die attachment, the assembly process, the package lamination and the via reliability, a set of design rules is proposed. In this regard, possible failure modes are identified and the critical process steps are specified.

In the overall embedding process the following failure modes are assessed as: (a) die fracture, (b) adhesive fracture, (c) copper fracture, (d) critical board warpage and (e) delamination.

Due to its complexity the delamination investigation represents a special topic of multilayer structures failure. Different experimental methods and material tests are required to obtain the interfacial strength. Due to its severity, which calls for an extensive independent study, delamination is not an objective of this thesis and therefore it is not analyzed here.

To determine the potential danger of failure during the embedding process, a risk matrix is proposed combining the defined failure modes and the process steps in Table 21. It is evaluated whether the particular failure mode: (i) is not observed in the process, (ii) is possible or (iii) is critical for the process.

Based on the risk matrix it is shown that the highest possibility of failure is found in the assembly process and the package lamination. Another critical step represents the package reliability testing. These processes and steps are identified as critical and their failure modes, which are further investigated, are marked in blue bold type.

Table 21: Risk matrix of the embedding process with investigated critical steps marked in blue bold type.

Failure modes / Process steps	Die fracture	Adhesive fracture	Copper fracture	Critical warpage
Die attachment	⊗	-	-	-
Assembly process	⊗	⊗	-	∇
Lamination	∇	∇	-	∇
Package reliability	⊗	⊗	∇	⊗

- not observed, ⊗.... possible, ∇.... critical,

The results of the parametric study summarize and cover an overall framework of the thesis. They lead to a definition of design rules for the embedding process.

6.1. Definition of failure criteria

In the proposed study the failure criteria are divided into (i) material tensile/bending strength, (ii) deflection limit and (iii) plastic deformation limit.

(i) Material strength

Die fracture is determined based on the silicon strength, which was measured by ball-on three-balls (B3B) testing, as described in chapter 4.3. The silicon strength is approx. 2575 MPa.

Adhesive fracture is assessed based on the adhesive strength, which was measured by means of a 3-point bending (3PB) experiment, as described in chapter 4.3. The adhesive strength is approx. 105 MPa.

(ii) Deflection limit

The critical package warpage is defined as the maximum allowable bow percentage (further called the critical bow percentage, B_L) according to the standards IPC-D-300G and IPC-TM-650 (number 2.4.22) [93, 94]. It should be mentioned that those standards account for laminates thicker than 0.5 mm, which is beyond the thickness of the assembled structure of 0.235 mm and the embedded die laminate thickness of 0.338 mm.

The critical bow percentage (B_L) is defined by the relation:

$$B_L = h_v / 2L_x, \quad (78)$$

$$h_v = R(1 - \cos(\alpha_w / 2)). \quad (79)$$

Where h_v is the maximum vertical displacement of the silicon die, L_x is the silicon die half-length in x-direction and α_w is the angle between the die edges, see Figure 82.

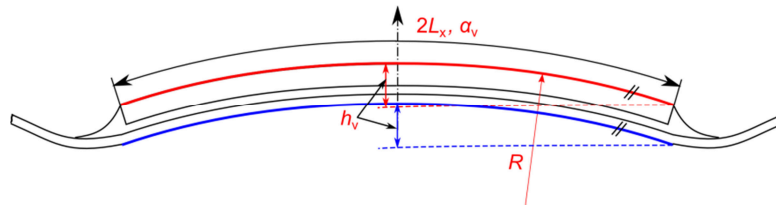


Figure 82: Maximum vertical displacement h_v of the silicon die defined in the assembled structure

(iii) **Plastic deformation limit**

Copper fracture is determined based on the via fatigue life assessment, as described in chapter 5. That means, for any case of a thermal cycling the plastic strain increment $\Delta\varepsilon_p$ is calculated numerically and the number of cycles to failure is evaluated based on the low-cycle fatigue approaches as a function of the copper ductility [84].

6.2. Parametric study

In order to define design rules of the investigated process steps, a parametric study is conducted. Regarding the almost square shape of the package its geometry is simplified by a 2D model and represented by a cross-section in the XZ-plane. The applicability of a 2D approach was demonstrated in chapters 3 - 5. A variety of analytical and numerical methods is used in the studies of each particular process step. The corresponding approaches are mentioned at the beginning of each study.

The stress-strain state in the package is influenced by many parameters during the manufacturing process. These are categorized as: (i) geometrical, (ii) material and (iii) process conditions. The specification and combination of these parameters according to the critical process steps is proposed in Table 22.

Table 22: Settings of the parametric study

Parameter category	Process step	Parameter
Geometrical	Assembly	Die size ($2L_x$) Silicon footprint (SF) Meniscus length (L_m) - -
	Lamination	Thickness (THK) - - - -
	Package reliability	- - - Wall angle (α_w) Aspect ratio (H/D)
Material	Assembly	Young's modulus (E) Volumetric shrinkage (ΔV)
	Lamination	
Process conditions	Package reliability	Reflow cycling test Temperature cycling test

The thickness (THK) is varied for the adhesive (BLT), the silicon die, the copper foil and the via bottom land. The nominal and variable value of the thickness is provided in the particular parametric study.

A **silicon footprint (SF)** defines the package occupancy by the silicon die as follows:

$$SF = A_{Si} / A_{Cu} \times 100 [\%], \quad (80)$$

$$A_{Si} = 2L_x^2, \quad (81)$$

$$A_{Cu} = [2(L_x + L_{Cu})]^2, \quad (82)$$

where A_{Si} is the area of the single silicon die and A_{Cu} is the area of the copper foil below and surrounding the single silicon die, see Figure 83. L_{Cu} is the copper foil half-distance between the investigated die and the adjacent one. The influence of the SF is only numerically investigated.

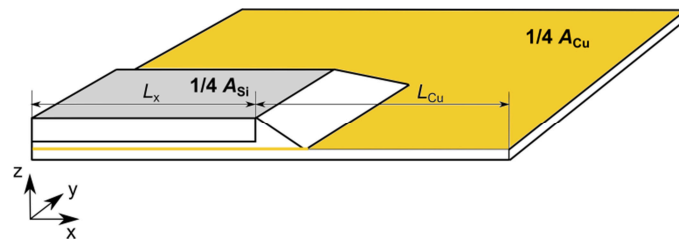


Figure 83: Illustration of a silicon footprint (SF) in one-quarter of the package.

The **via wall angle** (α_w) varies according to the used drilling technology. In the investigated case via holes are drilled through the adhesive BLT to the die copper pads (the via top land) by laser. Due to a possible laser beam oscillation the wall angle α_w is defined between the via and the via bottom land, see Figure 84.

The **secondary wall angle** (β_w) is specified in the model to take into account influence of an adjacent angle on the stress-strain state in the via top.

$$\beta_w = 180^\circ - \alpha_w \quad (83)$$

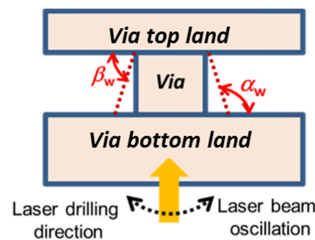


Figure 84: Definition of wall angles in the copper via.

The **via aspect ratio** (H/D) is a dimensionless parameter defining a relation between the circuit board thickness, *i.e.* the via height H , and the smallest drilled hole diameter, *i.e.* the via diameter D , see Figure 85. It is an important measure used in the microelectronic industry for the assessment of the minimum via hole size for the PCB design.

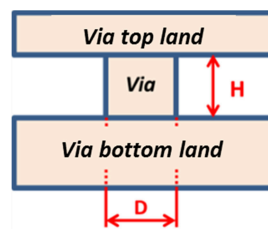


Figure 85: Aspect ratio H/D of the copper via.

6.3. Results and discussion

6.3.1. Design rules for the assembly process

The parametric study of the die assembly is provided using the analytical CLT, the interfacial model and a numerical FEA simulation of the process. All materials are modelled as linear-elastic (LE). The analysis follows the nominal process conditions defined in chapter 3. The in-plane stress σ_x is evaluated in the assembly center, *i.e.* far enough from free edges and corners. The assembly is assumed to be without any defects. Nominal and variable parameters of the study are summarized in Table 23.

Table 23: Nominal and variable parameters of the die assembly.

Category	Parameter	Nominal value	Variation	Figure
Geometrical	Si THK	120 μm	50 - 125 μm	86a, 88, 90a
	Adhesive BLT	45 μm	30 - 50 μm	86c, 88, 95
	Cu THK	70 μm	5 - 80 μm	86b, 88, 90b
	Die $2L_x$	7.2 mm	7-12 mm	91, 94, 95
	SF	9.64 %	5 - 65 %	88, 93
	Meniscus L_m	5% of $2L_x$	5 % of $2L_x$	91, 94, 95
Material	Si E	170 GPa LE	-	87, 89, 92
	Adhesive E	3.4 GPa LE	1.2 - 4 GPa	
	Cu E	92 GPa LE	-	86 - 95
	Adhesive ΔV	-6%	-3 and -6 %	
Failure criteria	Si strength	$\sim 2575 \text{ MPa}$		86, 87
	Adhesive strength	$\sim 105 \text{ MPa}$		88, 89
	Critical B_L	$\sim 1\%$		90 - 93

Die fracture during the assembly process

The stress level is evaluated on the silicon die top. The die reliability is limited by the silicon strength.

It is shown that a decrease of the die thickness leads to a significant reduction of the residual stress in silicon, see Figure 86a. If the thickness is reduced by a factor of 2.5, the stress drops from a level of 58 MPa by a factor of 6. The decrease is nonlinear. The thickness has a higher impact of on the stress level, if the adhesive has a higher volumetric shrinkage ΔV , *i.e.* in the case of $\Delta V = -6 \%$ in comparison with $\Delta V = -3 \%$.

If the thickness of the copper foil is between 80 and 60 μm , the adhesive shrinkage does not play a role and the silicon residual stress slightly increases from 54 MPa by about 13 % to 61 MPa, see Figure 86b. However, an additional reduction of the copper foil thickness entails on (i) an increase of the residual stress up to 101 MPa in the die in the case of a higher adhesive shrinkage of $\Delta V = -6\%$ and (ii) a stress decrease to 58 MPa in a case of a lower adhesive shrinkage of $\Delta V = -3\%$. The stress distribution is in both cases nonlinear.

With an increasing BLT, the stresses in the top of the silicon die slightly decrease by about 20%, see Figure 86c. There is a negligible difference between stresses generated for the two shrinkage values $\Delta V = -3\%$ and -6% .

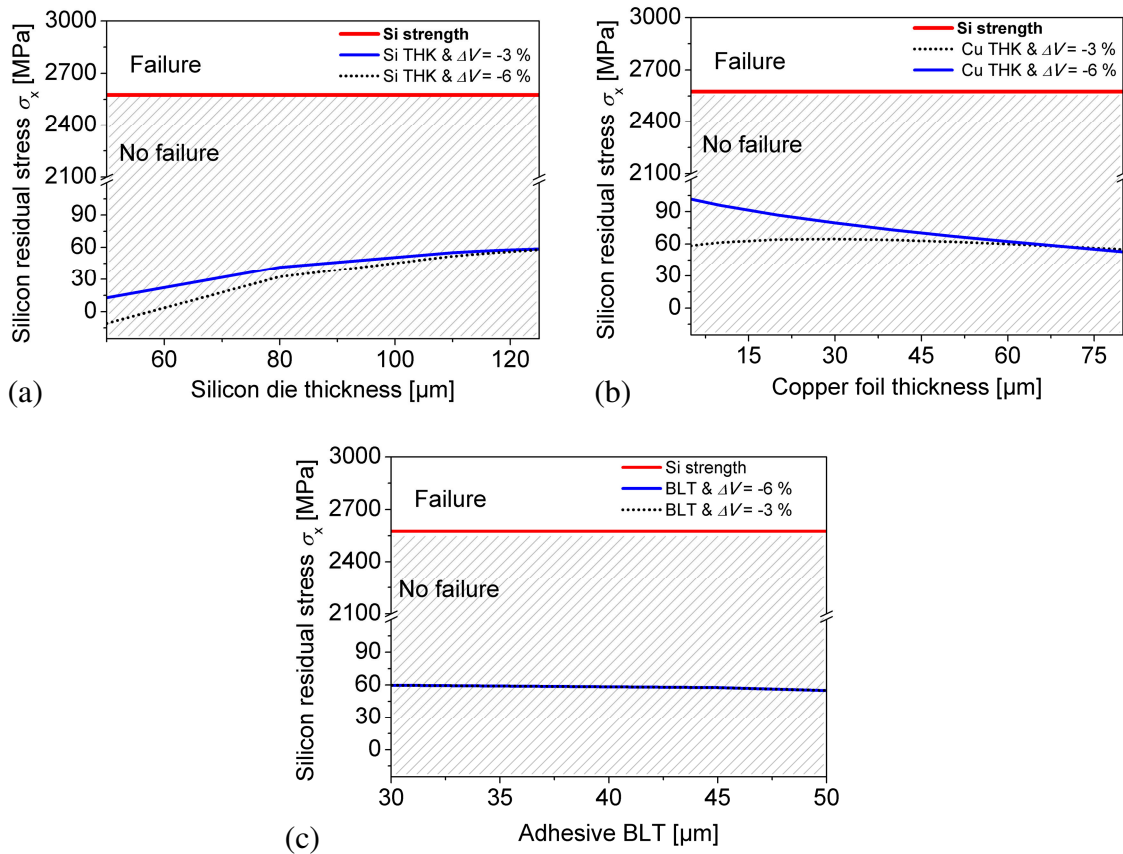


Figure 86: Silicon residual stress as a function of the adhesive shrinkage ΔV and (a) the die thickness, (b) the copper foil thickness, (c) adhesive BLT.

With increasing Young's modulus of the adhesive the stresses on the top of the silicon die slightly decrease from 57 MPa of less than 1 %. The impact of the different values of the adhesive shrinkage is negligible.

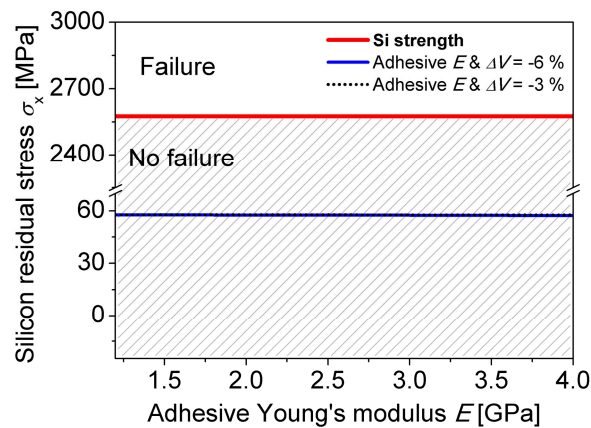


Figure 87: Silicon residual stress as a function of adhesive Young's modulus and shrinkage ΔV .

Based on Figure 86 and Figure 87 it is concluded that no contribution of any material and geometrical parameters produce residual stresses close to the silicon strength. Damage of the silicon die can therefore be precluded.

Adhesive fracture during the assembly process

The stress state is evaluated in the adhesive BLT in the vicinity of the silicon/adhesive interface. The reliability of the adhesive is limited by the adhesive strength.

In Figure 88 it is shown that the residual stress in the adhesive is practically independent from variable adhesive, copper and silicon thickness on a thickness range and it is influenced only by the adhesive shrinkage level. In case of $\Delta V = -6 \%$ σ_x is 95 MPa and for $\Delta V = -3 \%$ σ_x is 46 MPa.

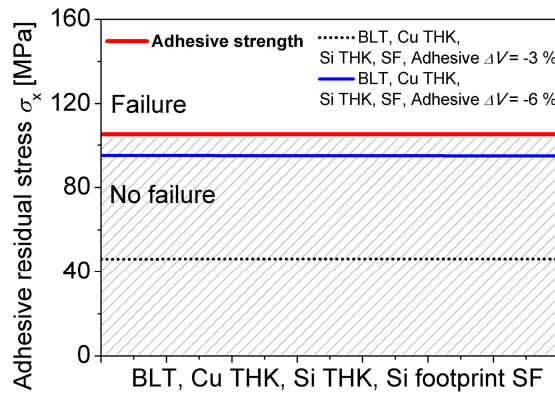


Figure 88: Adhesive residual stress as a function of the adhesive shrinkage ΔV , adhesive BLT, copper and silicon thickness and the silicon footprint (SF).

The adhesive residual stress is nearly linearly dependent on the adhesive Young's modulus. A change of 300 % of the Young's modulus leads to a significant increase of the residual stress by a factor 3, for both cases of volumetric shrinkage, as shown in Figure 89. This indicates a strain induced in the adhesive which is not dependent on its modulus E since for a fixed strain and elastic material behavior, the stress is directly proportional to the elastic modulus.

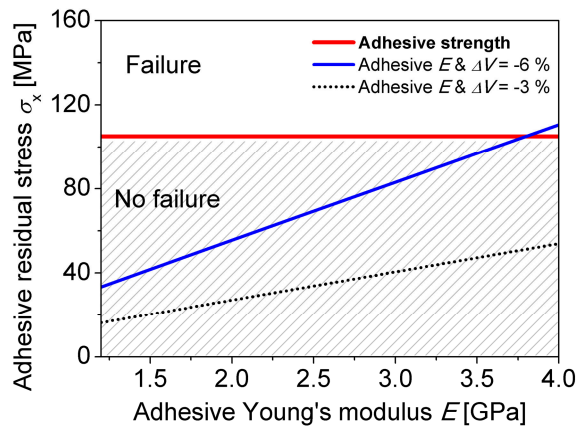


Figure 89: Adhesive residual stress as a function of the adhesive's Young's modulus and shrinkage ΔV .

It is shown that only a combination of high Young's modulus (4 GPa and higher) and a high volumetric shrinkage of the adhesive (-6% and higher) may lead to adhesive

damage. For a Young's modulus between 3.4 - 3.8 GPa, the residual stress in the adhesive reaches the critical value, if the adhesive exhibits volumetric shrinkage of -6 %.

Critical bow percentage of the assembled structure

The processability of the assembly in the subsequent lamination process is limited by a maximum bow percentage of 1% defined according to the standard IPC-D-300G [93]. It is shown that a decrease of the die thickness leads to a slight increase of the bow percentage, see Figure 91a. The bow grows by about 25 % from $B_L = 0.5$ %, if the thickness is reduced by a factor of 2.5. The impact of the silicon thickness is lower for a lower adhesive shrinkage of $\Delta V = -3$ % in comparison to $\Delta V = -6$ %. All bow results are below the critical value.

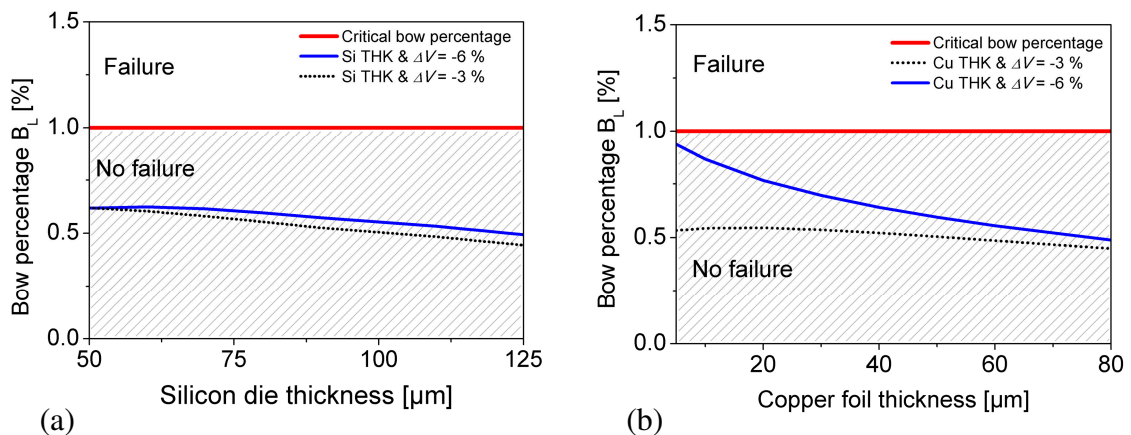


Figure 90: Bow percentage as a function of the adhesive shrinkage ΔV and (a) die thickness, (b) copper foil thickness.

With copper foil thickness decreasing from 80 μm to 5 μm the bow percentage increases, see Figure 90b. A significant bow increase by about 92 % from $B_L = 0.49$ % is observed in case of the higher adhesive shrinkage of ΔV of -6 %, whereas at ΔV of -3 % the bow percentage increases only by about 20%. A reduction of the copper thickness under 5 μm is not recommended, since it may lead to the critical bow.

Only a combination of a big die (higher than 12x12) and a high adhesive volumetric shrinkage (-6% and higher) may entail a critical bow percentage of 1 %, see Figure 91.

If the die size changes by a factor of 12, the bow percentage B_L increases by an average factor of 17 (for both adhesive shrinkages) to approx. 0.8 %.

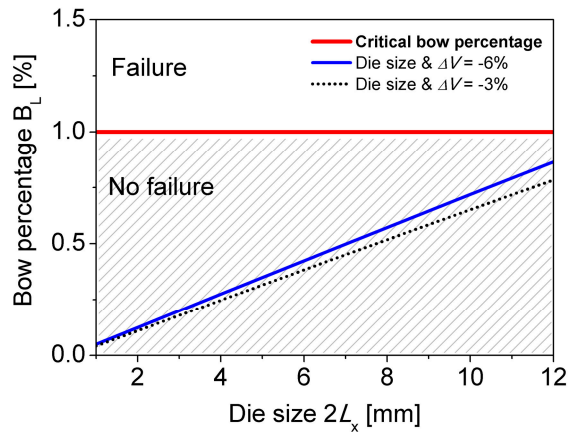


Figure 91: Bow percentage as a function of a die size $2L_x$ and the adhesive shrinkage ΔV .

The bow percentage is linearly dependent on the adhesive's Young's modulus. An increase of the adhesive's Young's modulus by a factor of 3 leads to a slight increase of the die bow by about 14 % (in average for both cases of the volumetric shrinkage) to approx. 0.5 %, as shown in Figure 92, which is below the critical value.

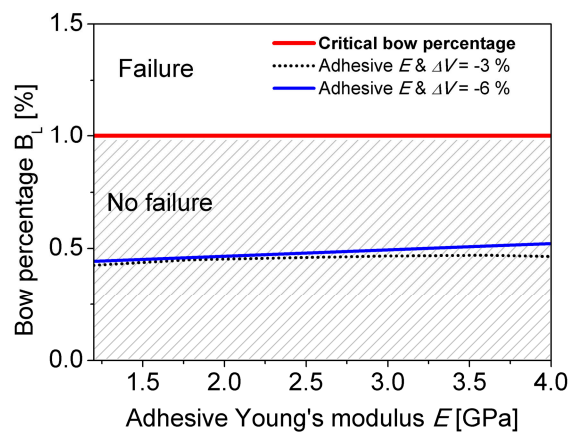


Figure 92: Bow percentage as a function of the adhesive's Young's modulus and shrinkage ΔV .

The silicon footprint has a very small impact on the assembly bow percentage, see Figure 93. In a range from 5 to 66 % of SF the bow increases by only about 8 % in the

case of a size of 7 mm die and about 2 % in the case of 12 mm die size. Modifying the silicon footprint does not lead to the critical bow percentage.

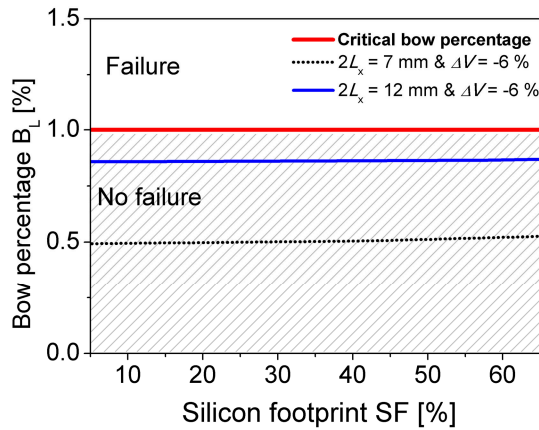


Figure 93: Bow percentage as a function of silicon footprint SF, evaluated for the die size of 7 mm and 12 mm.

The bow percentage is computed based on Eq. (78) and (79) across the area of the silicon die. It relates the die's vertical displacement h_v to the die size $2L_x$ and the die's curvature radius R . Figure 94a illustrates a curvature dependency on the die size. It is observed that for dies longer than 7 mm the curvature reaches a plateau at a curvature radius, which is only a function of the material combination. A conversion of the curvature R to a vertical displacement h_v demonstrates that the vertical lift depends on the die size, Figure 94b. This explains why a bigger die of $2L_x = 12$ mm reaches a higher bow percentage than a smaller die of $2L_x = 7$ mm.

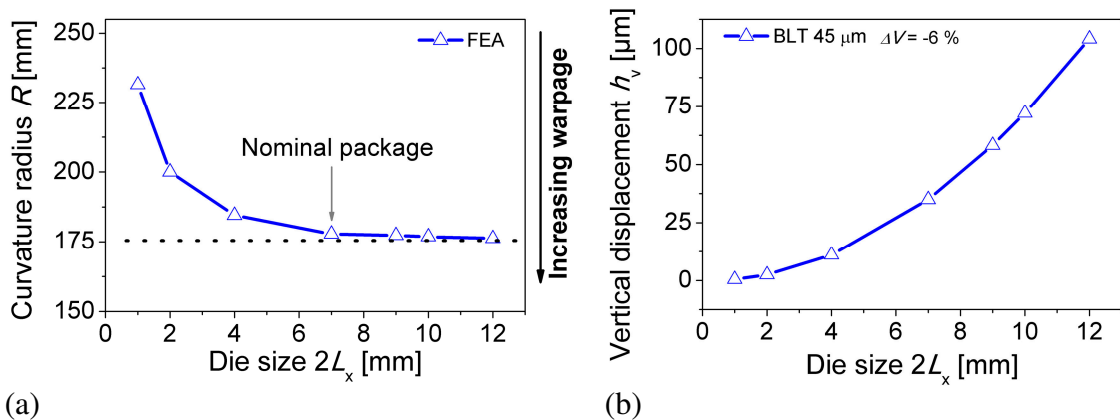


Figure 94: (a) Die curvature radius R as a function of the die size $2L_x$ [36]. (b) Die vertical displacement h_v as a function of the die size $2L_x$.

The adhesive BLT increases along with an increasing die size. The influence of BLT on the bow percentage is illustrated in Figure 95. It is shown that (i) the bow percentage B_L is independent from BLT if the adhesive volumetric shrinkage $\Delta V = -6 \%$ and (ii) the bow percentage B_L slightly decreases by less than 4 % with increasing BLT if $\Delta V = -3 \%$.

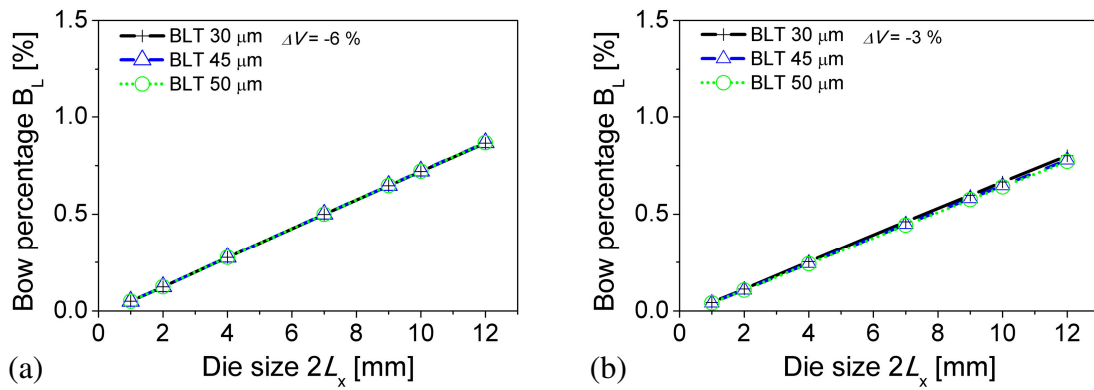


Figure 95: Bow percentage B_L as a function of the die size $2L_x$ and the adhesive BLT: (a) for the adhesive volumetric shrinkage $\Delta V = -6 \%$, (b) for the adhesive volumetric shrinkage $\Delta V = -3 \%$.

6.3.2. Design rules for the lamination process

A parametric study of the laminated package is provided by using a numerical analysis of the embedding process flow, as described in chapter 4. The analysis follows nominal process conditions. The adhesive and the copper are modelled as elasto-plastic (PL). The in-plane stress σ_x is evaluated in the package center, *i.e.* far enough from free edges and corners. The package is assumed to be without any defects. Nominal and variable parameters of the study are summarized in Table 24.

Table 24: Nominal and variable parameters of the lamination process study

Category	Parameter	Nominal value	Variation	Figure
Geometrical	Si THK	120 μm	-	96, 98a, 99a
	Adhesive BLT	45 μm	-	
	Cu THK	70 μm	-	
	Die $2L_x$	7.2 mm	-	
	SF	9.64 %	5 – 66 %	
	Meniscus L_m	5% of $2L_x$	-	
Material	Si E	170 GPa LE	-	97, 98b, 99b
	Adhesive E	3.4 GPa PL	-	
	Cu E	89 GPa PL	-	
	Resin E	4.7 GPa LE	4.3 – 6.7 GPa	
	E-glass E	72 GPa LE	-	
	Resin ΔV	-5 %	-3 and -5%	
Failure criteria	Si strength	$\sim 2575 \text{ MPa}$		96, 97
	Adhesive strength	$\sim 105 \text{ MPa}$		98a, b
	Critical B_L	$\sim 1\%$		99a, b

Die fracture during the lamination process

The stress state is evaluated in the silicon die top. The reliability of the die is limited by the silicon strength, see Figure 96. It is shown that with an increasing silicon footprint (from 5 to 66 %), the residual stress in the silicon die increases by about 17 % (from approx. -180 MPa to approx. -130 MPa). The silicon die top is under compression due to its concave bending, as it was demonstrated in chapter 4. The stress level is clearly below the material's limit, the die is therefore not expected to fail.

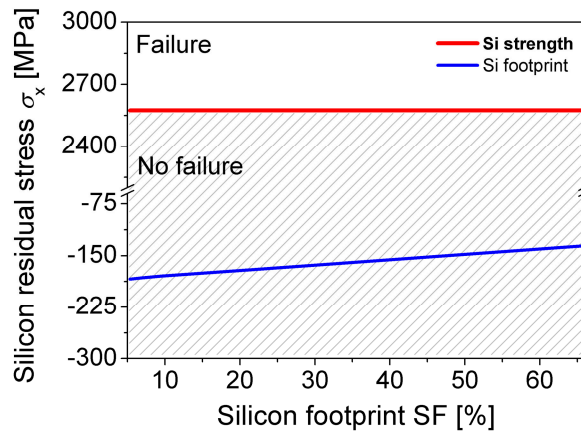


Figure 96: Silicon residual stress as a function of a silicon footprint (SF).

Based on Figure 97 it is proved that an increasing Young's modulus E of the resin in conjunction with an elevated curing volumetric shrinkage ΔV leads to a higher compression of the silicon die top. The stress in the silicon die behaves linearly with the resin's Young's modulus between 4.3 – 6.7 GPa. The stress level differs an average by about 53 % for the volumetric shrinkage ΔV of -3 % versus -5 %, e.g. $\sigma_x = -89$ MPa for $\Delta V = -3$ % and $\sigma_x = -136$ MPa for $\Delta V = -5$ % at $E = 4.3$ GPa.

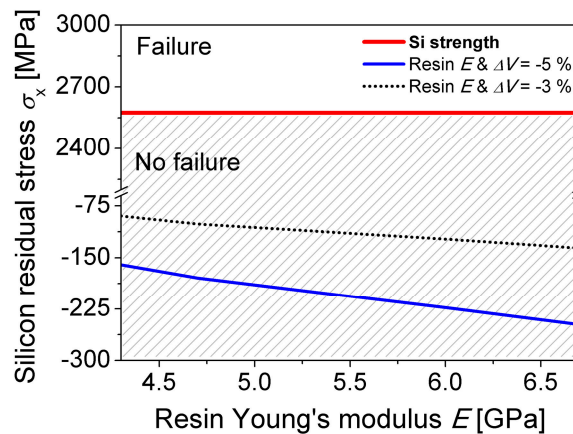


Figure 97: Silicon residual stress as a function of the resin's Young's modulus and the volumetric shrinkage ΔV .

Based on Figure 96 and Figure 97 it is concluded that no combination of material and geometrical parameters leads to die damage.

Adhesive fracture during the lamination process

The stresses are evaluated in the adhesive BLT in the vicinity of the silicon/adhesive interface. The reliability of the adhesive is limited by the adhesive strength, see Figure 98.

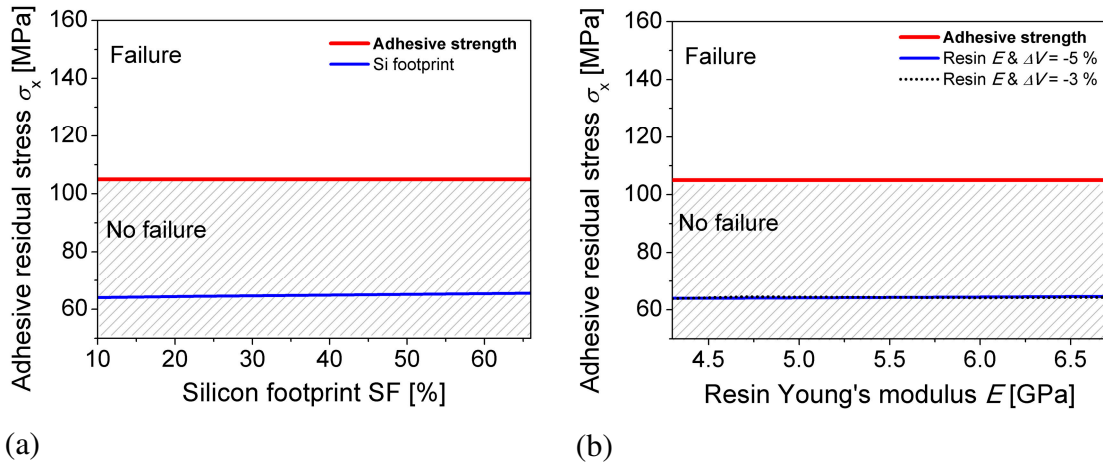


Figure 98: Adhesive residual stress as a function of the resin shrinkage ΔV and (a) silicon footprint; (b) resin Young's modulus E .

Based on Figure 98a, b it is proven that the silicon footprint and the resin's material properties practically do not influence the stress state in the adhesive layer. The stress remains at approx. 64 MPa and slightly increases by less than 1 % with an increasing elastic modulus of the resin and silicon footprint. The residual stress in the adhesive does not reach the material limit, failure can therefore be excluded.

Maximum bow percentage of the board during the lamination process

A higher silicon footprint leads to an increase of the package bow, see Figure 99a. The bow percentage B_L of 0.17 % at a silicon footprint of 5 % grows by about 52 % at 66 % SF.

The resin's material properties have a strong impact on the package warpage, see Figure 99b. The bow percentage increases almost linearly with the resin's Young's modulus ranging from 4.3 to 6.7 GPa. The bow magnitude for $E = 4.3$ GPa versus $E =$

6.7 GPa grows by a factor of 7 due to the resin volumetric shrinkage $\Delta V = -3\%$ and a factor of 2 for $\Delta V = -5\%$.

The package's bow percentage does not reach a critical level of approx. 1% in any case of the parametric study. The recorded warpage does not cause a problem for further manufacturing of the copper vias.

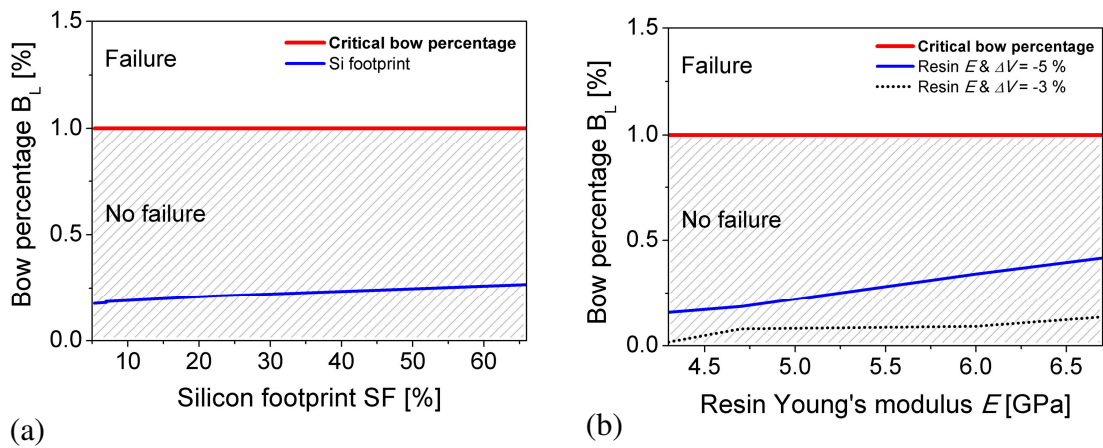


Figure 99: Bow percentage as a function of (a) silicon footprint, (b) resin shrinkage ΔV and the adhesive's Young's modulus E .

6.3.3. Design rules for a PCB board with vias

The reliability of a PCB board with vias is primarily investigated during the reflow cycling using FEA, as it is described in chapter 5. Nominal and variable parameters of the study are summarized in Table 25. The parametric study is extended by an investigation of a temperature cycling test representing testing conditions different from the reflow conditions. The electro-deposited (ED) copper is modelled as elasto-plastic. The number of cycles to via failure is determined based on the approaches by Coffin-Manson and Engelmaier, respectively [85, 84, 87].

Table 25: Nominal and variable parameters of the package reliability study

Category	Parameter	Nominal value	Variation	Figure
Geometrical	Si THK	120 μm	-	102, 103, 110 104, 111 101, 109
	Adhesive BLT	45 μm	-	
	Via diameter D	80 μm	60 - 150 μm	
	Wall angle α_w	90°	90 - 112°	
	Bottom land THK	32 μm	10 - 40 μm	
	Aspect ratio H/D	0.46	0.25 - 0.62	
Material	Si E	170 GPa LE	-	
	Adhesive E	3.4 GPa LE	-	
	ED Cu E	43.8 GPa PL	-	
	Resin E	4.3 GPa LE	-	
	E-glass E	72 GPa LE	-	
	Solder mask E	2.4 GPa LE	-	
Process conditions	Reflow cycling	10x(RT - 260 °C)		101 - 104
	Temperature cycling	10x(-40° - 160 °C)		105 - 111
Failure criteria	N_f	calculated	-	101, 103, 104, 109 - 111

The representative cell model is used for the numerical analysis. The package is represented by the 2ViasRef model. The plastic strain is evaluated in the critical via location P3. Additionally, the strain state at location P2 is taken into account, see Figure 100.

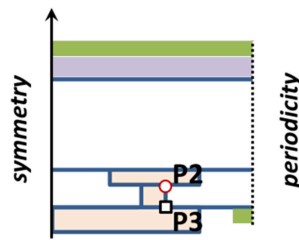


Figure 100: 2ViasRef numerical model for the strain evaluation in locations P2 and P3.

Figure 101 shows that a decrease of the aspect ratio H/D leads to a significant increase of a via's fatigue life. The lifetime of vias with an aspect ratio of 0.25 is approx. 8 times longer than of vias with an aspect ratio of 1.0.

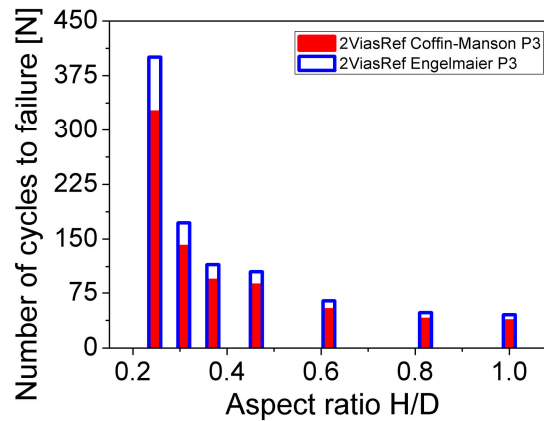


Figure 101: Via reliability as a function of a via aspect ratio H/D during the reflow cycling.

With a change of the via wall angle a shift of the critical via location is observed. When the via wall angle α_w increases, the wall angle β_w decreases according to Eq. (83). An adjacent fillet radius at P2 therefore starts to behave as the major stress-strain concentrator, see Figure 84 and Figure 102. The transition of the critical location from P3 to P2 is observed at $\alpha_w \approx 102^\circ$.

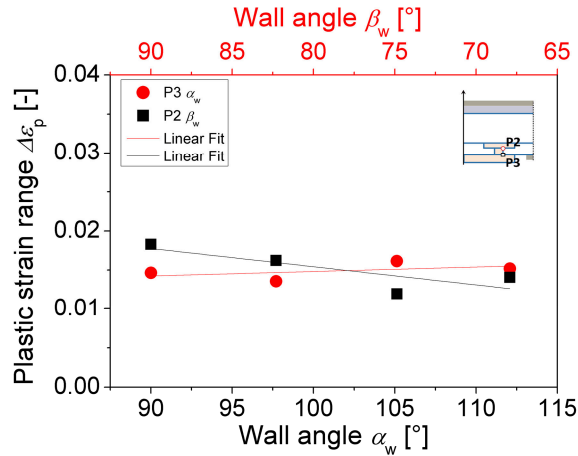


Figure 102: Equivalent plastic strain increment (range) $\Delta\epsilon_p$ as a function of wall angles α_w and β_w during the reflow cycling.

A high plastic straining reflects a high possibility for failure at a particular location, *i.e.* a low number of life cycles. Figure 103 shows that the strain decreases with an increasing wall angle. The same trend is observed for both wall angles α_w and β_w . These results are in agreement with conclusions of a work by Yamanaka [91]. As a consequence, the lifetime increases by about 55 % between an initial state defined by $\alpha_w = 90^\circ$ ($N_f = 85$ by Coffin-Manson) and $\alpha_w = 112^\circ$ ($N_f = 132$ by Coffin-Manson). A decrease of the wall angle β_w on the top of a via at location P2 results in reduction of the lifetime by about 8 % (from $N_f = 123$ to $N_f = 116$). According to the wall angle definition, a change of the wall angle does not alter the aspect ratio, see Figure 84.

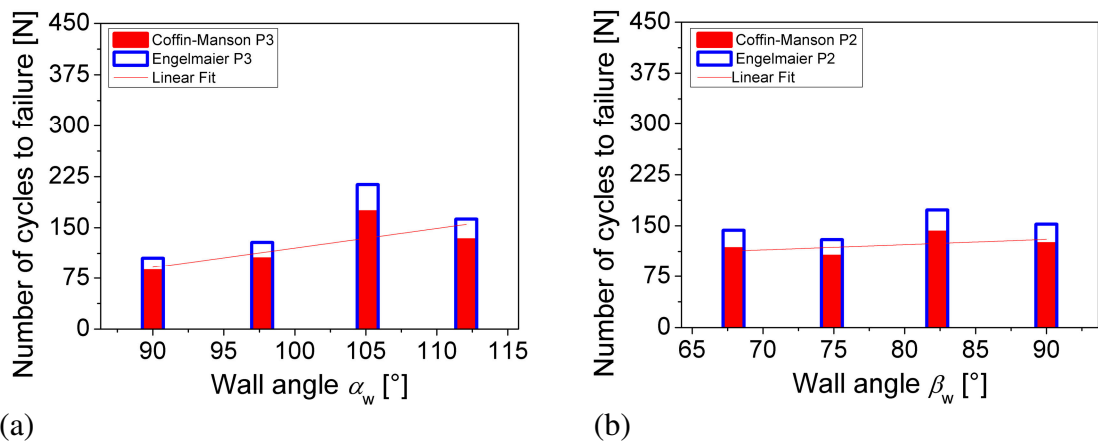


Figure 103: Via reliability as a function of wall angles (a) α_w and (b) β_w during the reflow cycling.

Based on Figure 104 it is shown that a decrease of the copper bottom land thickness has a positive influence on the via lifetime. A reduction of the thickness by a factor of 4 extends the lifetime by about. 76%. This is a result of a less pronounced stress concentration at location P3 due to a lower via bottom land stiffness.

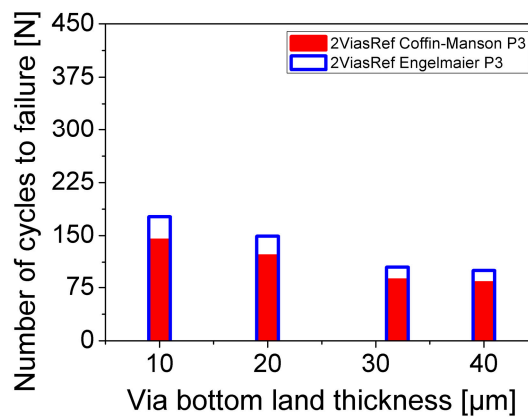


Figure 104: Via reliability as a function of the via bottom land thickness during the reflow cycling.

Loading mode of the via as a function of temperature

An additional study of via reliability is provided by the simulation of a temperature cycling test (TCT). The loading temperature varies in the range from -40 °C to T °C, see Figure 105. T is used as a parameter to be varied.

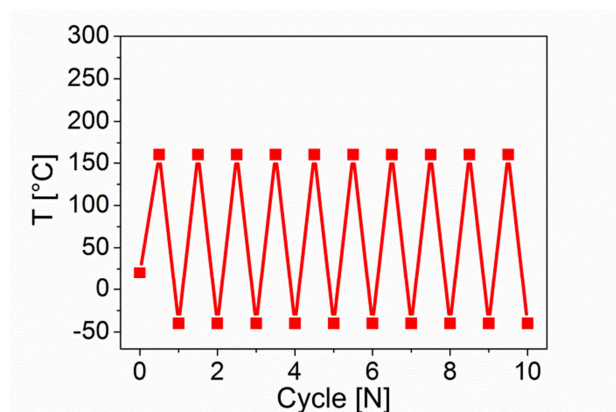


Figure 105: Temperature profile of a temperature cycling test (TCT).

During the TCT analysis a change of the critical via location from P3 to P2 is observed. The upper temperature level T is found to be responsible for this change. In this regard series of numerical analyses are conducted to find the transition temperature, see Figure 106. The transition is noticed around 250 °C.

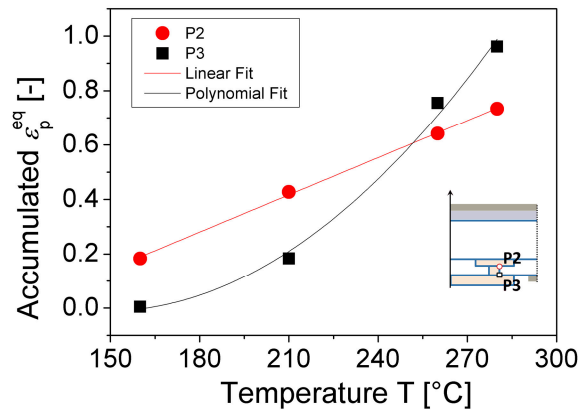


Figure 106: Accumulated plastic strain in locations P2 and P3 after 10 cycles as a function of the upper temperature T . Temperature cycling is provided in the range from RT to T .

Below 250°C the major part of the copper plasticization is accumulated at location P2 (top). P2 is thus the weakest point of the structure. Above 250 °C the largest amount of copper plasticization is accumulated in via location P3 (bottom) what thus becomes a critical location for via failure.

Besides, it is confirmed that a temperature cycling below 250 °C does not reverse the strain state at locations P2 and P3. The lower temperature, *i.e.* -40 °C or RT, causes only an increase of straining at location P2. The strain state at location P3 practically does not change, as demonstrated in Figure 107.

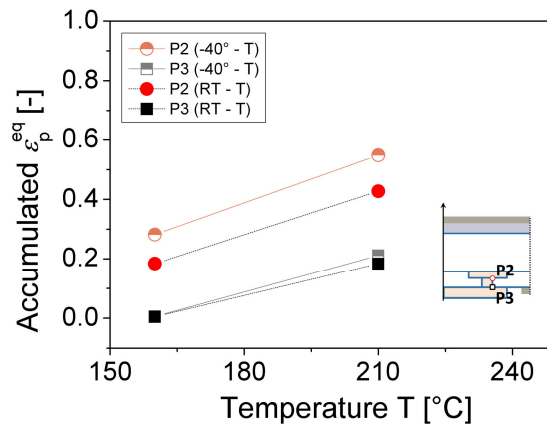


Figure 107: Accumulated plastic strain ε_p^{eq} as a function of a temperature T below 250°C during a temperature cycling from -40°C to T .

The change of the critical location is caused due to a switching of the major loading mode of the via. Below 250°C the via is mainly loaded by shear due to the adhesive's thermal expansion shifting the via in a horizontal direction. Above 250°C the adhesive predominantly bends the via into a convex shape because of a high expansion in the vertical direction.

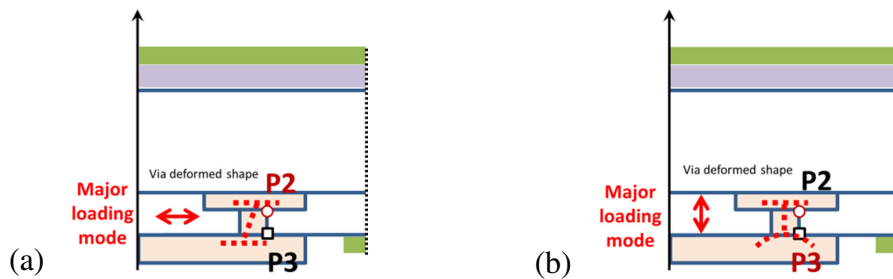


Figure 108: Major loading mode of vias (a) below 250°C , (b) above 250°C .

The temperature cycling is realized with a smaller temperature change ΔT of 200°C than during the reflow cycling (240°C). This consequently leads to a significant increase of via lifetime by a factor of 8. The number of cycles to failure obtained for a nominal via with the aspect ratio of 0.46 is $N_f = 85$ during the reflow cycling and $N_f = 680$ during TCT (Coffin-Manson).

A decrease of the aspect ratio H/D during TCT does not enhance via reliability that clearly as in the case of the reflow cycling, see Figure 109. The increase of lifetime is in the range of only 26% between the aspect ratios of 1.0 and 0.3. Below the aspect ratio of 0.3, *e.g.* 0.25, a significant decrease of via lifetime is observed. This point deviates from the results obtained during the reflow cycling. It shows that a too small aspect ratio is undesirable, if shear is the major loading mechanism of via.

For $T < 250\text{ }^{\circ}\text{C}$ the most critical location of the via remains at P2. The change in the via wall angle does not reverse the strain state at locations P2 and P3. In analogy to the reflow cycling, the number of cycles to failure slightly increases with an increasing wall angle, see Figure 110. It amounts to $N_f = 680$ (Coffin-Manson) for β_w of 90° with a decrease by 25 % at $\beta_w = 68^{\circ}$

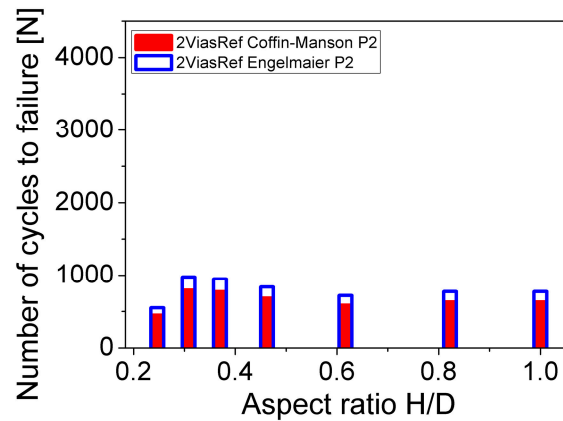


Figure 109: Via reliability as a function of the aspect ratio H/D during temperature cycling in a range from -40°C to 160°C .

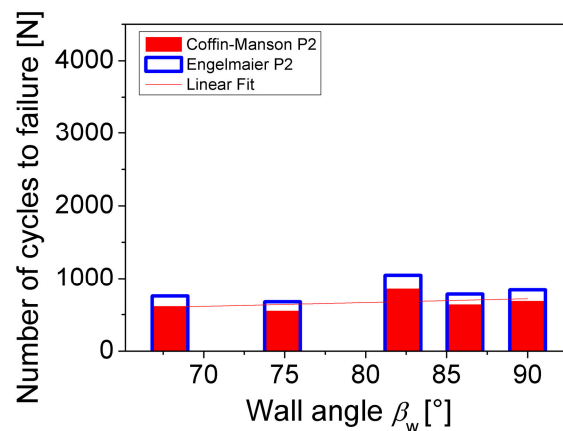


Figure 110: Via reliability as a function of wall angle β_w during temperature cycling in the range of from $-40\text{ }^{\circ}\text{C}$ to $160\text{ }^{\circ}\text{C}$.

Based on Figure 111 it is shown that the via bottom land thickness is the most important geometrical parameter influencing via failure during temperature cycling below 250 °C. A decrease of the copper bottom land thickness leads to a significant increase of via lifetime. A reduction of the thickness by factor 4 extends the lifetime by a factor of 8 up to $N_f = 3500$ (Coffin-Manson).

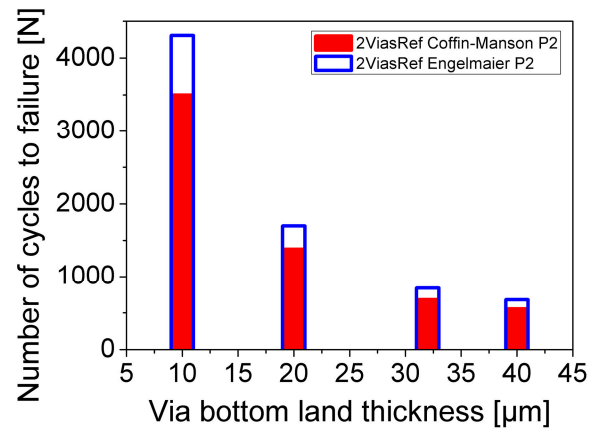


Figure 111: Via reliability as a function of the via bottom land thickness during the temperature cycling in the range from -40 °C to 160 °C.

6.4. Summary and conclusions

In order to improve the embedding process, design rules are defined using a parametric study. For this purpose, the influence of variable material (Young's modulus and volumetric shrinkage) and geometrical parameters (thickness, die size, via aspect ratio, via wall angle, etc.) as well as the process conditions on the package reliability are studied. The highest likelihood for package failure is identified in the assembly process, the lamination and the reliability testing during a temperature cycling.

In the assembly process it is found that:

- The residual stresses arising in the silicon die due to adhesive curing do not cause silicon failure. They are far below the measured silicon strength of approx. 2575 MPa. Any proposed change of silicon, copper and adhesive thickness in combination with varying adhesive volumetric shrinkage is not critical for the die.
- The adhesive's residual stress is critical since it is close to the measured strength of approx. 105 MPa. Adhesive failure is predicted, if the adhesive volumetric shrinkage remains at its nominal value of -6 % and the adhesive's Young's modulus exceeds 3.8 GPa. The residual stress in the adhesive increases linearly with an increasing Young's modulus and the volumetric shrinkage of the adhesive.
- The assembly bow percentage does not reach the critical level of 1 % determined by standards IPC-D-300G and IPC-TM-650 in any case of the parametric study. Therefore lamination of the assembled structure can be carried out without causing any problems.

In the lamination process it is shown that:

- The residual stresses in the silicon die due to resin curing are compressive and they do not lead to silicon failure. Any modification of the silicon footprint and the resin's material properties (Young's modulus, volumetric shrinkage) is not dangerous for the die.
- Due to lamination the adhesive's residual stress decreases by approx. 25% from the critical level after the assembly process. Adhesive failure is therefore not predicted in the investigated area as described above.

- The assembly bow percentage does not reach a critical level of 1 % in any case of the parametric study. Therefore further manufacturing of the copper vias in the laminate is possible without any problems.

In the PCB board with vias it is shown that:

- Two major loading mechanisms of the package are observed as a function of the upper temperature, *i.e.* the horizontal shift and the vertical bending of the via. They significantly influence the impact of the via's geometrical parameters (aspect ratio, wall angle, bottom land thickness) on the package reliability.
- During a temperature cycling below 250 °C the weakest point of the structure lies in the top via's fillet radius, signed as P2. In this case, the via bottom land thickness becomes the most important geometrical parameter influencing via failure. Its reduction by a factor of 4 extends the package lifetime by a factor of 8.
- During a temperature cycling above 250 °C the weakest point of the structure lies in the bottom via's fillet radius, signed as P3. In that case a via aspect ratio H/D has the biggest influence on via failure. Its reduction by a factor of 4 extends the package lifetime by a factor of 8.
- It is shown that the via wall angle α_w causes a change of the critical location from P3 to P2, if it is greater than 102°. The wall angle does not affect the via reliability significantly.

7. Conclusions

This thesis investigates critical process steps during the die embedding process for manufacturing highly integrated printed circuit boards (PCBs). Both analytical and numerical models are employed to describe the warpage and the stress distribution in the package during different critical steps (*i.e.* die attachment, assembly and lamination). The main conclusions derived from the investigation are listed below, corresponding to the different steps.

1) In order to describe the **die attachment process** by an adhesive on a copper foil, a numerical model has been developed. The model allows calculating the adhesive flow underneath the die, forming a bond line thickness layer (BLT) with all physical phenomena included, such as surface tension, contact angle, adhesive non-Newtonian flow behavior and real droplet shape (“star shape”). In addition, an analytical model has been devised to describe the development of the BLT, based on experimental measurements by confocal microscopy on the real assemblies. It is shown that the droplet star shape is dominant, provided that a relatively high attachment force (5 N, 10 N, 15 N) is applied. In such a case the analytical results deviate from the measurements. It can be concluded that the analytical model is therefore limited to a small attachment force range. The numerical simulation in its present form is rather time-consuming and thus not suitable for industrial use.

2) In the **assembly process** the package warpage and residual stresses are identified as the critical parameters, associated with a mismatch of the coefficients of thermal expansion (CTEs) during adhesive and epoxy resin curing at elevated temperatures. The polymers volumetric shrinkage is characterized using a modified rheology measurement approach. The model results are validated experimentally by a Rocking-Curve-measurement of the package warpage, resulting in an error of less than 6%. The following conclusions can be drawn:

- The maximum calculated stresses in the silicon die (*i.e.* approx. 100 MPa) are clearly below its measured characteristic strength (*i.e.* approx. 2575 MPa).
- The stresses calculated in the adhesive are of the order of the measured adhesive strength (*i.e.* approx. 105 MPa). The stresses in the copper foil are well above the

measured values for its yield stress (*i.e.* approx. 160 MPa) due to the use of a linear elastic material model. Taking into account the elasto-plastic material behavior of the adhesive as well as the copper, the stress peaks in the copper foil are reduced. Nevertheless, the influence of plasticity on the curvature radius is not significant, because (i) the plastic deformations in the copper are confined to only small regions of the assembly; (ii) there are only small plastic deformations in the adhesive.

3) The **lamination process** is numerically analyzed taking into account the influence of the package loading history. A process flow modelling is performed. The complexity of the prepreg structure is considered. The analytical lamination theory of woven structures is employed for the determination of homogenized orthotropic properties of the prepregs. Very good agreement is achieved between the numerical and the experimental results after the copper removal step. The following conclusions can be drawn:

- The relatively low maximum residual stress in the silicon die (*i.e.* approx. -179 MPa) will not cause die damage during the lamination.
- The residual stress in the adhesive decreases by about 25 % from the level after the assembly process. Therefore the adhesive will not fail during the lamination.
- The stresses calculated in the resin layer are slightly higher than typical values for the epoxy resin strength of approx. 130 MPa. However, a proper viscoelastic model for the epoxy material will reduce these stresses by about 20%, and thus result in stresses below the strength of the resin.

Finally, a **reliability analysis** of a PCB board with vias has been performed by numerically investigating the stress evolution in critical regions during the reflow cycling. To decrease the complexity of the package containing copper vias and traces, a numerical modelling approach has been presented. The influence of variable material (Young's modulus and volumetric shrinkage) and geometrical parameters (thickness, die size, via aspect ratio, via wall angle, etc.) as well as the process conditions on the package reliability is studied. Based on the numerical stress-strain results, the concepts by Coffin-Manson and Engelmaier have been employed for the evaluation of the lifetime of the copper vias during the low-cycle fatigue.

Conclusions

Based on the process investigations design rules for the die embedding have been derived. The results of this work can consequently lead to a possible improvement of the reliability of future PCB systems.

List of figures

Figure 1: The embedding process chain defined by AT&S: (a) the die attachment, (b) the assembly process, (c) the PCB core lamination, (d) testing of the PCB board containing vias.	2
Figure 2: Schematic picture of the die attachment process.	3
Figure 3: The semiconductor silicon die with copper-patterned side [9].	3
Figure 4: The real adhesive droplet shape obtained by a Nano Focus measurement [9].	4
Figure 5: The analytical model for the adhesive flow during the attachment process, (a) for fully filled area under the silicon die and (b) with the simplified adhesive droplet [9].	5
Figure 6: The adhesive droplet contour (red line) with the cylindrical droplet with a radius r_g (blue line) and the cylindrical die with a radius R_d (black line). The scale of the X- and Y-axis corresponds to the die size [9].	6
Figure 7: Schematic of a numerical 2D axisymmetric model with simplified copper pads on the silicon die.	10
Figure 8: The adhesive droplet definition in the <i>Eulerian mesh</i> : (a) the sharp phase interface after initialization, (b) the smooth phase interface with VOF recalculation [15].	13
Figure 9: The contact angle θ_w definition [15].	14
Figure 10: Velocity profile at no-slip (a), free slip (b) and slip (c) wall conditions [14].	16
Figure 11: Shear-rate dependent viscosity of the new and aged adhesive at room temperature. The line represents a power law fit function of the experimental data [21].	18
Figure 12: (a) The adhesive droplet 3D reconstruction, (b) Adhesive profile data used for a polynomial function fitting [24].	19
Figure 13: (a) Cross section of the die attached to the copper foil by an adhesive droplet (b) Locations of the adhesive bond line thickness measurement #1, #2, #3, #4.	20
Figure 14: The averaged adhesive bond line thickness after the die placement as a function of the attachment force and the holding time.	20
Figure 15: Comparison of experimental data and the adhesive bond line thickness development for the new and aged adhesive using analytical Eq. (13) for (a) the attachment force $F = 1$ N, (b) the attachment force $F = 5$ N.	21
Figure 16: Comparison of experimental data and the adhesive bond line thickness development for the new and aged adhesive using analytical Eq. (13) for (a) the attachment force $F = 10$ N, (b) the attachment force $F = 15$ N.	22
Figure 17: Moving contact line problem in a numerical simulation (a) Vacuum and adhesive distribution in a computational domain, (b) Reaction forces arising at interface I (<i>free slip</i>) and at interface II (<i>no-slip</i>).	23
Figure 18: (a) The vacuum and the adhesive distribution underneath a silicon die, (b) Radial velocity profile of vacuum with <i>free slip</i> and the adhesive with <i>no-slip</i> condition at the wall.	24
Figure 19: Adhesive bond line thickness (BLT) development for fully filled area underneath the silicon die with a radius R_d of 3.375 mm, viscosity η of 0.1 Pa.s and force F of 1e-3 N. Comparison of the analytical model Eq. (9) and the numerical (CFD) solution [9].	25
Figure 20: 2D flow model of the real adhesive droplet (red – adhesive, blue – vacuum) [9].	26

List of figures

Figure 21: Free droplet profile: Numerically caused voids between the adhesive droplet and the silicon die (top wall) due to a missing initial contact between the adhesive and the silicon die [9].....	26
Figure 22: (a) The assembled structure in a cross-section, (b) The 24" x 18" copper panel with uniformly distributed dies [35, 36].	28
Figure 23: The temperature profile (red solid line) of the assembly process with corresponding adhesive volumetric shrinkage ΔV (blue dotted line). The temperature increase of $\Delta T_{ic} = 1^\circ\text{C}$ is used within the curing time of steps B and D in the numerical simulation [36, 37].	29
Figure 24: Schematic of the assembled structure based on the classical laminate theory (CLT). The structure consists of three layers with different material properties (E_i , α_i , ν_i) and heights (h_i), 1: silicon die, 2: adhesive, 3: copper foil [36].	30
Figure 25: Schematic of the in-plane stress distribution and the curvature of the tri-material assembly using the classical laminate theory (CLT).	32
Figure 26: Schematic of the assembled structure based on the interfacial model. 1: silicon die, 2: adhesive, 3: copper foil. The coordinate system centralized in the middle of the adhesive bond line thickness (BLT) is used for derivation of stresses and strains [36].....	32
Figure 27: Shearing forces and bending moments in the tri-material assembly [43].....	34
Figure 28: Schematic of the shearing and peeling stress and curvature of the tri-material assembly using the interfacial model.	34
Figure 29: Numerical model of the assembled structure with boundary conditions. FEA represents a numerical model with the real assembly geometry. <i>Ref.FEA</i> is a numerical model having the same configuration as the interfacial model [36].	35
Figure 30: Load vs displacement curves of 3PB tests of an adhesive bar-shaped specimen. A linear behavior can be observed over a wide range, with a small amount of plastic deformation just before fracture [36, 52].	40
Figure 31: Copper foil plasticity data at various temperatures [36, 52].	42
Figure 32: (a) Definition of the curvature radius, R , from points (black dots) on the die top, (b) The warpage evolution in the steps B-E , in the XZ-plane [35].....	43
Figure 33: In-plane residual stress σ_x in the assembly center after the temperature step E , CLT result (black dotted line) vs. FEM result (red solid line) [35].....	46
Figure 34: Maximum principal stress σ_1 [MPa] in the assembly after the temperature step E , (a) top view, (b) bottom view [35].	46
Figure 35: In-plane residual stress (a) in the x-direction (σ_x) and (b) in the y-direction (σ_y) after the temperature step E through the assembly center (red solid line), along the edge (blue dashed line) and along the corner (green dotted line) [35].	47
Figure 36: (a) Shearing stress distribution along the edge in the interfaces 12 and 23 evaluated by FEA, <i>Ref.FEA</i> and the interfacial model. (b) Shearing stress field in FEA and <i>Ref.FEA</i> model [36].	49
Figure 37: (a) Shearing stress distribution in a diagonal direction to the die corner in the interfaces 12 and 23 evaluated by FEA, <i>Ref.FEA</i> and the interfacial model. (b) Shearing stress field in FEA and <i>Ref.FEA</i> model.	49
Figure 38: (a) Peeling stress distribution along the edge in the interfaces 12 and 23 evaluated by FEA, <i>Ref.FEA</i> and the interfacial model. (b) Peeling stress field in FEA and <i>Ref.FEA</i> model.....	51
Figure 39: (a) Peeling stress distribution in a diagonal direction to the die corner in the interfaces 12 and 23 evaluated by FEA, <i>Ref.FEA</i> and the interfacial model. (b) Peeling stress field in FEA and <i>Ref.FEA</i> model.	51

List of figures

Figure 40: The principal stress σ_1 in the package after cooling to RT, in the assembly's XZ-plane for the LE model [36].	52
Figure 41: (a) Temperature (red solid line) and pressure (black dashed line) profile of the embedding process, (b) Investigated package after the assembly process, the lamination process and the copper (Cu) removal [52].	56
Figure 42: The structure of prepregs in the package [52].	58
Figure 43: Concept of lamination theory of woven structures: (a) Interlacing region of a plain woven structure, (b) One-quarter model of a symmetry woven structure used for the analytical calculation (a unit cell), (c) An idealized unidirectional cross-ply laminate model representing the homogenized prepreg properties [74, 75].	60
Figure 44: Parameters for the definition of strand shape functions (a) along the warp direction and (b) along the fill direction [74, 75].	61
Figure 45: Geometrical representation of numerical models: (a) 2D model with symmetry condition, (b) 2D axisymmetric model, (c) 3D quarter symmetry model.	65
Figure 46: Computational steps of the embedding process simulation with the corresponding applied temperature and pressure [52]. The change of the lamination temperature (from red dotted line to red solid line) profile is described in section 4.3.	67
Figure 47: (a) Numerical model of the embedded die package in particular manufacturing steps, i.e. the assembly process, the lamination and the copper (Cu) removal, (b) Real copper pattern and its simplification in the FEA model, (c) Real prepreg structure and its simplification in the FEA model [52].	68
Figure 48: (a) Cross-section of the embedded die package showing prepreg deformation in contact with the adhesive meniscus, (b) Numerical simplification of prepregs in contact with the adhesive meniscus.	68
Figure 49: (a) Schematic of the lamination press [46], (b) Boundary conditions of the package fixed between preheated platens in the lamination (step F - G) [52].	69
Figure 50: Idealized graphs of fully cured adhesive thermo-elastic properties: (a) Young's modulus E as a function of temperature, (b) Coefficient of thermal expansion CTE as a function of temperature. A clear softening of the material is observed at the glass transition temperature T_g of approx. 100°C .	70
Figure 51: (a) Real resin curing profile (red solid line) with a volumetric shrinkage ΔV (blue solid line) development, (b) Simplification of the resin curing profile (from pink dashed to red solid line) and a volumetric shrinkage ΔV (from cyan dotted to blue solid line) used in the FEA.	71
Figure 52: Idealized graph of Resin's Young's modulus E as a function of temperature. The softening of the material is around the glass transition temperature T_g of approx. 150°C .	72
Figure 53: The curvature radius R definition in (a) the assembled structure, (b) the laminated package [52].	74
Figure 54: Maximum principal stress σ_1 [MPa] in the overall package at the end of (a) the assembly step E , (b) the lamination step G and (c) the copper removal step H [52].	75
Figure 55: Schematic of locations for the in-plane stress evaluation [52].	76
Figure 56: The investigated package with configurations of copper vias and traces: (a) Package top view with a cross section, (b) Package bottom view with a detail of the vias and the traces.	79
Figure 57: Reflow cycling temperature profile.	80
Figure 58: Copper via geometry.	80
Figure 59: Strain-fatigue life curve [83].	83
Figure 60: Schematic of fatigue life assessment of copper vias during the reflow cycling.	83

List of figures

Figure 61: Boundary conditions of the numerical model.....	84
Figure 62: The package representation by sections (S1 - S4) of the most common via interconnects.	84
Figure 63: Numerical model of the package.	85
Figure 64: Bilinear-kinematic hardening model of the electro-deposited copper.	87
Figure 65: Idealized graph of fully cured resin coefficient of thermal expansion (CTE) as a function of temperature. The glass transition temperature T_g is approx. 150°C	87
Figure 66: Idealized graphs of thermo-elastic properties of a fully cured solder mask: (a) Young's modulus E as a function of temperature, (b) Coefficient of thermal expansion (CTE) as a function of temperature. The glass transition temperature T_g is approx. 100°C	89
Figure 67: Critical locations P1 - P4 at a diameter transition in each via 1 - 5.	89
Figure 68: Distribution of the maximal principal stress σ_1 [MPa] in the package in 10^{th} cycle (a) at 260°C , (b) at RT. The detail is plotted for the via in position 5.	90
Figure 69: Area for the stress-strain evaluation illustrated in the critical location P3.	91
Figure 70: (a) Distribution of the maximum principal stress σ_1 [MPa] over via positions 1 - 5 and locations P1 - P4. (b) Distribution of the accumulated equivalent plastic strain $\varepsilon_p^{\text{eq}}$ [-] over via positions 1 - 5 and locations P1 - P4.	92
Figure 71: (a) Schematic of the free vias pattern, (b) Symmetry of the free via pattern.	92
Figure 72: Distribution of the maximum principal stress σ_1 [MPa] over via positions 1 - 5 and locations P1 - P4 in (a) the via pattern S1, (b) the via pattern S4.	93
Figure 73: Distribution of the accumulated equivalent plastic strain $\varepsilon_p^{\text{eq}}$ [-] over via positions 1 - 5 and locations P1 - P4 in (a) the via pattern S1, (b) the via pattern S4.	93
Figure 74: (a) Schematic of two coupled vias patterns S1 and S4, (b) Symmetry of a two coupled vias pattern.	94
Figure 75: (a) Schematic of the 4 vias coupled pattern S3 in comparison to (b) an idealized pattern X where all vias are coupled.	94
Figure 76: Distribution of the maximum principal stress σ_1 [MPa] over via position 1 - 5 and locations P1 - P4 (a) in the via patterns S3 vs X and (b) in the via patterns S3 vs S2.	95
Figure 77: Distribution of the accumulated equivalent plastic strain $\varepsilon_p^{\text{eq}}$ [-] over via position 1 - 5 in (a) the via patterns S3 vs X in locations P1 - P2 and (b) the via patterns S3 vs X in locations P3 - P4.	95
Figure 78: Distribution of the accumulated equivalent plastic strain $\varepsilon_p^{\text{eq}}$ [-] over via position 1 - 5 and location P1 - P4 in the via patterns S3 vs S2.	96
Figure 79: The package superposition by (a) the single reference via model (1ViaRef) and (b) two vias reference model (2ViasRef).	97
Figure 80: Comparison of the results of the via pattern S2 and the 1ViaRef model: (a) The maximum principal stress σ_1 [MPa] over 10 reflow cycles at location P3 and P4, (b) The accumulated equivalent plastic strain $\varepsilon_p^{\text{eq}}$ [-] over 10 reflow cycles at location P3 and P4.	97
Figure 81: Comparison of the results of the via pattern S1 and the 2ViasRef model: (a) The maximum principal stress σ_1 [MPa] over 10 reflow cycles at locations P1 - P4, (b) The accumulated equivalent plastic strain $\varepsilon_p^{\text{eq}}$ [-] over 10 reflow cycles at locations P1 - P4.	98
Figure 82: Maximum vertical displacement h_v of the silicon die defined in the assembled structure	103
Figure 83: Illustration of a silicon footprint (SF) in one-quarter of the package.	104
Figure 84: Definition of wall angles in the copper via.	105

List of figures

Figure 85: Aspect ratio H/D of the copper via.....	105
Figure 86: Silicon residual stress as a function of the adhesive shrinkage ΔV and (a) the die thickness, (b) the copper foil thickness, (c) adhesive BLT.	107
Figure 87: Silicon residual stress as a function of adhesive Young's modulus and shrinkage ΔV	108
Figure 88: Adhesive residual stress as a function of the adhesive shrinkage ΔV , adhesive BLT, copper and silicon thickness and the silicon footprint (SF).....	109
Figure 89: Adhesive residual stress as a function of the adhesive's Young's modulus and shrinkage ΔV	109
Figure 90: Bow percentage as a function of the adhesive shrinkage ΔV and (a) die thickness, (b) copper foil thickness.	110
Figure 91: Bow percentage as a function of a die size $2L_x$ and the adhesive shrinkage ΔV	111
Figure 92: Bow percentage as a function of the adhesive's Young's modulus and shrinkage ΔV	111
Figure 93: Bow percentage as a function of silicon footprint SF, evaluated for the die size of 7 mm and 12 mm.	112
Figure 94: (a) Die curvature radius R as a function of the die size $2L_x$ [36]. (b) Die vertical displacement h_v as a function of the die size $2L_x$	112
Figure 95: Bow percentage B_L as a function of the die size $2L_x$ and the adhesive BLT: (a) for the adhesive volumetric shrinkage $\Delta V = -6\%$, (b) for the adhesive volumetric shrinkage $\Delta V = -3\%$	113
Figure 96: Silicon residual stress as a function of a silicon footprint (SF).	115
Figure 97: Silicon residual stress as a function of the resin's Young's modulus and the volumetric shrinkage ΔV	115
Figure 98: Adhesive residual stress as a function of the resin shrinkage ΔV and (a) silicon footprint; (b) resin Young's modulus E	116
Figure 99: Bow percentage as a function of (a) silicon footprint, (b) resin shrinkage ΔV and the adhesive's Young's modulus E	117
Figure 100: 2ViasRef numerical model for the strain evaluation in locations P2 and P3.....	119
Figure 101: Via reliability as a function of a via aspect ratio H/D during the reflow cycling.	119
Figure 102: Equivalent plastic strain increment (range) $\Delta \epsilon_p$ as a function of wall angles α_w and β_w during the reflow cycling.	120
Figure 103: Via reliability as a function of wall angles (a) α_w and (b) β_w during the reflow cycling.....	120
Figure 104: Via reliability as a function of the via bottom land thickness during the reflow cycling.	121
Figure 105: Temperature profile of a temperature cycling test (TCT).....	121
Figure 106: Accumulated plastic strain in locations P2 and P3 after 10 cycles as a function of the upper temperature T. Temperature cycling is provided in the range from RT to T.	122
Figure 107: Accumulated plastic strain ϵ_p^{eq} as a function of a temperature T below 250°C during a temperature cycling from -40°C to T.....	123
Figure 108: Major loading mode of vias (a) below 250°C, (b) above 250°C.	123
Figure 109: Via reliability as a function of the aspect ratio H/D during temperature cycling in a range from -40°C to 160°C.....	124

List of figures

Figure 110: Via reliability as a function of wall angle β_w during temperature cycling in the range of from -40 °C to 160 °C..... 124

Figure 111: Via reliability as a function of the via bottom land thickness during the temperature cycling in the range from -40 °C to 160 °C. 125

List of tables

Table 1: The adhesive material coefficients	18
Table 2: Elastic properties of the adhesive and the adhesive volumetric shrinkage at temperature steps B - E	38
Table 3: Adhesive volumetric shrinkage at temperature steps B - E	39
Table 4: Elastic properties of standard silicon wafers in $\langle 100 \rangle$ -orientation [55, 56].....	40
Table 5: Weibull parameters along with the 90% confidence intervals for silicon dies tested under biaxial bending using the ball-on-three-balls test.	41
Table 6: Elastic properties of the copper foil and copper CTE [60, 61].	42
Table 7: The curvature radius R and the maximum in-plane stress σ_x through the package center in the silicon die, in the adhesive close to the adhesive/silicon interface and in the copper foil for steps B – E obtained by FEA.	44
Table 8: The curvature radius, R , of the package after cooling down to RT.....	45
Table 9: Influence of plasticity on the curvature radius R of the package after cooling down to RT [36].	53
Table 10: Influence of plasticity on the in-plane residual stress σ_x through the package center and the maximum σ_x in the entire model [36]......	53
Table 11: Averaged prepreg strand dimensions based on cross-section measurements.	60
Table 12: Comparison of numerical models used for the embedding process simulation with a corresponding calculation time (FEA performed on a PC cluster with two 64-bit 6-core processors Xeon X5650 (2010)).	65
Table 13: Homogenized orthotropic properties of prepreg #1037 at RT containing the influence of the resin curing shrinkage.....	73
Table 14: Homogenized orthotropic properties of prepreg #2116 at RT containing the influence of the resin curing shrinkage.....	73
Table 15: The curvature radius R development after the assembly step E , the lamination step G and the copper removal step H , in comparison with a Rocking-Curve-measurement [52]......	74
Table 16: The in-plane stress σ_x [MPa] through the package center in steps E , G and H [52]......	77
Table 17: Stress-strain data of electro-deposited copper as a function of temperature [89, 84].	86
Table 18: Homogenized orthotropic properties of prepreg #1037 with fully cured resin at 260°C.....	88
Table 19: Homogenized orthotropic properties of prepreg #2116 with fully cured resin at 260°C.....	88
Table 20: Reliability of copper vias during the reflow cycling evaluated for the critical location P3 in the via.	99
Table 21: Risk matrix of the embedding process with investigated critical steps marked in blue bold type.	102
Table 22: Settings of the parametric study.....	104
Table 23: Nominal and variable parameters of the die assembly.....	106
Table 24: Nominal and variable parameters of the lamination process study.....	114

List of tables

Table 25: Nominal and variable parameters of the package reliability study 118

References

- [1] C. F. Coombs Jr., Printed circuits handbook, New York: McGraw-Hill, Inc, 2008.
- [2] J. Stahr, M. Morianz, M. Brizoux, A. Grivon und W. Maia, „Simulation of Embedded Components in PCB Environment and Verification of Board Reliability,“ in *Proc. of IPC APEX EXPO Conference*, San Diego, 2013.
- [3] W. Jillek and W. K. Yung, “Embedded component in printed circuit boards: a processing technology review,“ *Int J Adv Manuf Technol*, vol. Volume 25, no. Issue 3-4, pp. 350-360, 2005.
- [4] R. Tummala, Fundamentals of Microsystems Packaging, McGraw-Hill, 2001.
- [5] S. P. Timoshenko, „Analysis of bi-metal thermostats,“ *J Opt Soc Am*, Bd. 11, pp. 233-255, 1925.
- [6] M. Deluca, R. Bermejo, M. Pletz, P. Supancic und R. Danzer, „Strength and fracture analysis of silicon-based components for embedding,“ *J Eur Ceram Soc*, Bd. 31, Nr. 4, pp. 549-558, 2011.
- [7] M. Deluca, R. Bermejo, M. Pletz, M. Weßner, P. Supancic und R. Danzer, „Influence of deposited metal structures on the failure mechanisms of silicon-based components,“ *J Eur Ceram Soc*, Bd. 32, Nr. 16, pp. 4371-4380, 2011.
- [8] M. Deluca, R. Bermejo, M. Pletz, M. Morianz, J. Stahr, P. Supancic und R. Danzer, „Local strength measurement technique for miniaturised silicon-based components,“ in *Proc. IEEE EuroSimE*, Linz, 2011.
- [9] K. Macurova, A. Kharicha, M. Pletz, M. Mataln, R. Bermejo, R. Schongrundner, T. Krivec, T. Antretter, W. Maia, M. Morianz und M. Brizoux, „Multi-physics simulation of the component attachment within embedding process,“ in *Proc. IEEE EuroSimE*, Wroclaw, 2013.
- [10] Y. Yu-Tang, "Optimization of screen-printing parameters of SN9000 ink for pinholes using Taguchi method in chip on film packaging," *Robot Comput Integr Manuf*, no. 27, pp. 531-537, 2011.
- [11] P. J. Leider and R. B. Bird, “Squeezong Flow between Parallel Disks. I. Theoretical Analysis,“ *Ind Eng Chem Fundam*, vol. 13, no. 4, pp. 336-341, 1974.
- [12] J. Engmann, C. Servias and A. S. Burbinge, “Squeeze flow theory and applications to rheometry: A review,“ *J Non-Newton Fluid*, vol. 132, pp. 1-27, 2005.
- [13] M. J. Stefan, “Versuche Über Die Scheinbare Adhäsion, Akad. Wiss. Wien.,“ *Math Natur*, vol. Abt. 2, no. 69, pp. 713-735, 1874.
- [14] J. D. Anderson, Computational fluid dynamics: The basics and application, McGraw-Hill, Inc, 1995.
- [15] ANSYS® Academic Research, “Help System, FLUENT User's Guide,“ ANSYS, Inc.

References

- [16] G. J. Dienes und H. K. Klemm, „Theory and Application on the Parallel Plate Plastometer,“ *J Appl Phys*, Bd. 17, pp. 458-471, 1946.
- [17] S. Oka und R. F. Eirich, „The principles of rheometry,“ in *Rheology, Theory and Applications, Ed. Vol. 3, Chapter 2*, New York, Academic Press, 1960, pp. 73-75.
- [18] J. Schultz and M. Nardin, *Handbook of adhesive technology*, New York: Marcel Dekker, 1994.
- [19] A. Germuth, *Project A3.18: Determination of the rheological properties for two adhesives (L35 20120530 Du01)*, Leoben: Chair of Polymer Processing, Montanuniversitaet Leoben, 2012.
- [20] R. P. Chhabra, “Non-Newtonian Fluids: An Introduction,” Departement of Chemical Engineering, Indian Institut of Technology Kanpur.
- [21] K. Macurova, *Project A3.18 Review: Simulation of the packaging process of embedded components in printed circuit boards*, Leoben: Materials Center Leoben Forschung GmbH, April 2013.
- [22] D. W. Van Krevelen, *Properties of Polymers*, Amsterdam: Elsevier, 2009.
- [23] „<http://www.epoxyworktops.com/epoxy-resin/mech-properties.html>,“ [Online].
- [24] G. Maier und M. Wießner, *Project A3.18: Bestimmung von Grundfläche, Höhe und Schnittlinien von Kleberpads*, Leoben: Materials Center Leoben Forschung GmbH, 2012.
- [25] K. Hermansson, U. Lindberg, B. Hök und G. Palmkog, „Wetting properties of silicon surfaces,“ in *Proc. Solid-State Sensors and Actuators, TRANSDUCERS '91*, San Francisco, 1991.
- [26] P. G. de Gennes, “Wetting: statics and dynamics,“ *Rev Mod Phys*, Vols. 57, No.3, no. Part I, pp. 827-863, July 1985.
- [27] W. Schrittwieser und T. Krivec, *Project A3.18 - Simulation of chip embedding: Target application for first DoE*, Leoben: AT&S, 2012.
- [28] M. Lee, „The squeezing process of complex epoxy patterns in the die-attaching of large IC-chip,“ in *International Conference on Electronic Materials and Packaging EMAP*, Kowloon, 2006.
- [29] S. N. Reznik und A. L. Yarin , „Strong squeezing flow between parallel plates leads to rolling motion at the contact line,“ *Int J Multiphase Flow* , Bd. 28, pp. 911-925, 2002.
- [30] S. B. O'Brien and L. W. Schwartz, “Theory and modeling of thin film flow,“ in *Encyclopedia of Surface and Colloid Science*, Marcel Dekker, 2002, pp. 5283-5297.
- [31] R. G. Cox, „The dynamics of the spreading of liquids on a solid surface. Part 1. Viscous flow,“ *J Fluid Mech*, Bd. 168, pp. 169-194, 1986.
- [32] L. M. Hocking, “A moving fluid interface. Part 2. The removal of the force singularity by a slip flow,“ *J Fluid Mech*, vol. 79, no. 02, pp. 209-229, 1977.

References

- [33] S. Zahedi, *Numerical Methods for Fluid Interface Problems*, Stockholm: KTH Computer Science and Communication, 2011.
- [34] U. Küttler, C. Förster und W. A. Wall, „A Solution for the Incompressibility Dilemma in Partitioned Fluid–Structure Interaction with Pure Dirichlet Fluid Domains,“ *Comput Mech*, Bd. 38, pp. 417-429, 2006.
- [35] K. Macurova, R. Schöngrundner, R. Bermejo, M. Pletz, P. Angerer und T. Antretter, „Influence of adhesive properties on stress distribution and deflection of silicon dies during the assembly process,“ *unpublished*.
- [36] K. Macurova, R. Bermejo, M. Pletz, R. Schöngrundner, T. Antretter, T. Krivec, M. Morianz, M. Brizoux und A. Lecavelier, „Comparison of Different Methods for Stress and Deflection Analysis in Embedded Die Packages during the Assembly Process,“ *International Microelectronics and Packaging Society - JMPP*, Bd. 2, p. in press, 2015.
- [37] K. Macurova, P. Angerer, R. Schöngrundner, T. Krivec, M. Morianz, T. Antretter, R. Bermejo, M. Pletz, M. Brizoux und W. Maia, „Simulation of stress distribution in assembled silicon dies and deflection of printed circuit,“ in *Proc. IEEE EuroSimE*, Ghent, 2014, pp. 1-7.
- [38] G. Kirchhoff, „Über das Gleichgewicht und die Bewegung einer elastischen Scheibe,“ *Journal für die reine und angewandte Mathematik*, Bd. 40, pp. 51-88, 1850.
- [39] K. S. Pister und S. B. Dong, „Elastic Bending of Layered Plates,“ *J Eng Mech Div*, Bd. 84, Nr. 4, pp. 1-10, 1959.
- [40] E. Reissner und Y. Stravsky, „Bending and stretching of certain types of heterogeneous aeolotropic elastic plates,“ *J Appl Mech*, Bd. 28, Nr. 3, pp. 402-408, 1961.
- [41] J.-M. Berthelot, „Classical laminate theory,“ in *Composite Materials*, New York, Springer, 1999, pp. 287-311.
- [42] D. Sujan, M. V. Murphy, K. N. Seetharamu und A. Y. Hassan, „Improved engineering model for interfacial shearing stress analysis of a heated three layered structure in Electronic Packaging,“ in *Proc. International Conference on Advances in Mechanical Engineering*, Kuala Lumpur, 2009.
- [43] D. Sujan, M. V. Murthy und K. N. Seetharamu, „Imprpved tri-material interfacial stress model with the effect of different temperature in the layers,“ *J App Mech*, Bd. 81, pp. 561-568, 2011.
- [44] E. J. Barbero, *Finite element analysis of composite materials*, Boca Raton: CRC Press, 2008.
- [45] T. Böger, K. Dilger und G. Schmöller, „FE-Simulation der Klebstoffschwindung schwindung während des Aushärtevorgangs,“ *immersive SIM engineering GmbH*, München, 2001.
- [46] M. Pletz, R. Bermejo, P. Supancic, J. Stahr and M. Morianz, „Numerical investigation of the process of embedding components into printed circuit boards,“ in *Proc. IEEE EuroSimE*, Linz, April 2011.

References

- [47] ANSYS® Academic Research, „Release 14.5“.
- [48] M. Haider, P. Hubert und L. Lassard, „Cure shrinkage characterization and modeling of a polyester resin containing low profile additives,“ *Composites Part A: Applied Science and Manufacturing*, Bd. 38, pp. 994-1009, 2006.
- [49] A. Wallner, *Project A3.18: Measurement of the shrinkage of one adhesive*, Leoben: Chair of Polymer Processing, Montanuniversitaet Leoben, 2013.
- [50] G. Schmöllner, „Eingefrorene Spannungen: Konsequenzen für die Simulation am Beispiel von Klebverbindungen,“ immersive SIM engineering GmbH, München, 2006.
- [51] R. Schöngrundner, *Project A3.18: Temperature dependent material properties at the relevant length scale*, Leoben: Materials Center Leoben Forschung GmbH, 2014.
- [52] K. Macurova, P. Angerer, R. Bermejo, M. Pletz, R. Schöngrundner, T. Antretter, T. Krivec, M. Morianz, M. Brizoux und A. Lecavelier, „Stress and deflection development during die embedding into printed circuit boards,“ *Materials today: Proceedings*, Bd. in submission, pp. 1-10, 2015.
- [53] A. J. Schwartz, M. Kumar, B. L. Adams und D. Field, *Electron Backscatter Diffraction in Materials Science*, Springer, 2009.
- [54] M. Deluca und R. Bermejo, *Project A3.18: Raman spectroscopy measurements on glued Si chips and embedded LTCC substrates*, Leoben: Materials Center Leoben Forschung GmbH, 2013.
- [55] M. A. Hopcroft, W. D. Nix and T. W. Kenny, „What is the Young’s Modulus of Silicon?,“ *J Micromech S*, vol. 19, no. 2, pp. 229-238, 2010.
- [56] A. Masolin, P. O. Bouchard, R. Martini und M. Bernacki, „Thermo-mechanical and fracture properties in single-crystal silicon,“ *J Mater Science*, Bd. 48, pp. 979-988, 2013.
- [57] R. Bermejo, I. Kraveva, M. Deluca und P. Supancic, *Project A3.18: Strength measurement of commercial miniaturized components (ISFK)*, Leoben: Institute of Structural and Functional Ceramics, Montanuniversitaet Leoben, 2012.
- [58] *Norm. TTT: EN 843-5, Advanced Technical Ceramics - Monolithic Ceramics - Mechanical Tests at Room Temperature - Part 5: Statistical Analysis*, 1997.
- [59] R. Danzer, T. Lube, P. Supancic und R. Damani, „Fracture of ceramics,“ *Adv Eng Mater*, Bd. 10, Nr. 4, pp. 275-298, 2008.
- [60] G. Khatibi, M. Klein, E. El-Magd, H. D. Marchent, B. Weiss, R. Wiechmann und P. Zimprich, „Thermoelastic performance of copper foil and Cu/FR-4 and Cu/PI laminates,“ in *Proc. IPC Printed Circuits EXPO*, Anaheim, 2001.
- [61] „<http://www.itl.nist.gov/div898/handbook/pmd/section6/pmd641.htm>,“ [Online].

References

- [62] C. S. Wong, N. Benett, D. Allen, P. McNally und A. Danilewsky, „A novel x-ray diffraction technique for analysis of die stress inside fully encapsulated packaged chips,“ in *Proc. Electronics System-Integration Technology Conference*, Amsterdam, 2012, pp. 1-6.
- [63] P. Angerer, K. Macurova und R. Schöngrundner, *Project A3.18: High-Temperature Curvature measurements of various silicon single crystals (wafers) by means of X-ray diffraction (Rocking Curve Measurements)*, Leoben: Materials Center Leoben Forschung GmbH, 2013.
- [64] N. Lu, Z. Zhang, J. Yoon und Z. Suo, „Singular stress fields at corners in flip-chip packages,“ *Eng Fract Mech*, Bd. 86, pp. 38-47, 2012.
- [65] E. Suhir, „Calculated thermally induced stresses in adhesively bonded and soldered assemblies,“ in *Proc. ISHM International Symposium on Microelectronics*, Atlanta, 1986.
- [66] F. D. Fischer, T. Antretter und E. R. Oberaigner, „Mechanics of sheared bands - Application to faults, twins and variants,“ *J Mech Mater*, Bd. 2, pp. 195-205, 2008.
- [67] C. T. Peng und K. N. Chiang, „Overview of multilayered thin film theories for MEMS and electronic packaging applications,“ in *Proc. Thermal and Thermomechanical Phenomena in Electronic Systems IThERM*, Hsinchu, 2002.
- [68] J. Chen und J. S. Bull, „Approaches to investigate delamination and interfacial toughness in coated systems: an overview,“ *J Phys D: Appl Phys*, Bd. 44, Nr. 3, 2011.
- [69] B. D. Harper und Y. Weitsman, „Residual thermal stresses in an unsymmetrical cross-ply graphite/epoxy laminate,“ in *Proc. of AIAA/ASME/ASCE/AHS 22nd Structures, Structural Dynamics and Materials Conference*, Atlanta, GA, 1981.
- [70] R. B. R. van Silfhout, J. G. J. Beijer und W. D. van Driel, „Modelling Methodology for Linear Elastic Compound Modelling Versus Visco-Elastic Compound Modelling,“ in *Proc. International Conference on Thermal, Mechanical and Multi-Physics Simulation and Experiments in Microelectronics and Microsystems*, Berlin, 2005.
- [71] A. Ostmann, D. Manassis, J. Stahr, M. Beesley, M. Cauwe und J. De Baets, „Industrial and technical aspects of chip embedding technology,“ in *Proc. Electronics System-integration Technology Conference and Exhibition*, London, 2008.
- [72] G. Layhe, „Education and training in Electronic Design Realisation: Multilayer bonding – what’s it all about?,“ EDR Centre , Merlose, 2002.
- [73] M. M. Shokrieh, *Residual stresses in composite materials*, Cambridge: Woodhead Publishing Series in Composites Science and Engineering: Number 48, 2014.
- [74] N. K. Naik und V. K. Ganesh, „An analytical method for plain weave fabric composites,“ *Composites* , Bd. 26, Nr. 4, pp. 281-289, 1995.
- [75] N. K. Naik und V. K. Ganesh, „Prediction of on-axes elastic properties of plain weave fabric

References

- composites," *Compos Sci Technol*, Bd. 45, pp. 135-152, 1992.
- [76] A. Adumitroaie und E. J. Barbero, „Stiffness and Strength Prediction for Plain Weave Textile Reinforced Composites," *Mech Adv Mater Struc*, Bd. 19, Nr. (1-3), pp. 169-183, 2012.
- [77] N. R. Sottos, J. M. Ockers und M. Swindeman, „Thermoelastic Properties of Plain Weave Composites for Multilayer Circuit Board Application," *J Electron Packaging*, Bd. 121, pp. 37-43, 1999.
- [78] E. J. Barbero, J. Trovillion, J. A. Mayugo und K. K. Sikkil, „Finite element modeling of plain weave fabrics from photomicrograph measurements," *Compos Struct*, Bd. 73, pp. 41-52, 2005.
- [79] S. Rzepka, F. Krämer, O. Grassmé und J. Lienig, „A Multilayer PCB Material Modeling Approach Based on Laminate Theory," in *Proceedings of 9th International Conference on Thermal, Mechanical and Multiphysics Simulation and Experiments in Micro-Electronics and Micro-Systems, EuroSimE*, Freiburg, 2008.
- [80] MATLAB 7.11.1, The MathWorks, Inc., Natick, Massachusetts, United States..
- [81] K. Kaw, *Mechanics of Composite Materials*, Boca Raton: CRC Press, 2006.
- [82] P. Angerer, R. Schöngrundner, M. Wiessner, K. Macurova und J. Keckes, „Curvature determination of embedded silicon chips by in-situ rocking curve X-ray diffraction measurements at elevated temperatures," *Microelectron Eng*, Bd. under submission, 2015.
- [83] R. O. Ritchie und Y. Murakami, *Comprehensive Structural Integrity: Cyclic loading and fatigue*, Elsevier, 2003.
- [84] K. Weinberg und W. H. Müller, „A strategy of damage assessment of thermally stressed copper vias in microelectronic printed circuit boards," *Microelectron Reliab*, Bd. 48, Nr. 1, p. 68–82, 2008.
- [85] G. Voyiadjis, *Handbook of Damage Mechanics, Nano to Macro Scale for Materials and Structures*, Springer, 2015.
- [86] K. Smith, C. Johnson und S. Sitaraman, „A Modeling Method For The Study Of Thermomechanical Behavior Of High Density Interconnect (HDI) Vias," *Int J Microcircuits Electron Packag*, Bd. 21, Nr. 2, p. 1998, 177-185.
- [87] W. Engelmaier, „Effects of Power Cycling on Leadless Chip," in *Proc. Annual International Electronics Packaging Conference*, San Diego, 1982.
- [88] D. A. Barker D.B., „Thermal analysis in plated-through-hole reliability," in *In: Lau JH, editor. Thermal stress and strain in microelectronic packaging*, New York, 1993.
- [89] J. C. DiTomasso, „<http://www.ecs.umass.edu/mie/labs/mda/fea/ditomaso/Main.htm>," Stress analysis of vias within general electric's multichip modules. University of Massachusetts at Amherst, MA, report provided on the web, October 2014. [Online].

References

- [90] T. H. Wang und Y. S. Lai, „Stress analysis for fracturing potential of blind via in a build-up substrate,“ *Circuit World*, Bd. 32, Nr. 2, pp. 39-44, 2006.
- [91] K. Yamanaka, T. Fujisaki, M. Ichinose und T. Ooyoshi, „Effect of geometry and dielectric material on thermo-mechanical strain on micro-vias in build-up substrates,“ *Mater Sci: Mater Electron*, Bd. 21, p. 943–949, 2010.
- [92] D. Lu und C. P. Wong, *Materials for Advanced Packaging*, Springer, 2009.
- [93] *IPC-D-300:Printed Board Dimensions and Tolerances*.
- [94] *IPC-TM-650 TEST METHODS MANUAL: Number 2.4.22 - Bow and Twist (Percentage)*, 1999.